DOCTOR OF PHILOSOPHY

Mechanistic understanding of enhanced mechanical strength of Type 304 stainless steel brazed joints
microscopic and macroscopic considerations

Li, Yao

Award date:
2020

Awarding institution:
Coventry University

Mechanistic understanding of enhanced mechanical strength of Type 304 stainless steel brazed joints: microscopic and macroscopic considerations

By

Yao Li

PhD

March 2020

Mechanistic understanding of enhanced mechanical strength of Type 304 stainless steel brazed joints: microscopic and macroscopic considerations

Yao Li

A thesis submitted in partial fulfilment of the University's requirements for the Degree of Doctor of Philosophy

March 2020

Content removed on data protection grounds

Certificate of Ethical Approval

Applicant:

Yao Li

Project Title:

Critical processing factors that affect the strength of joints when joining similar and dissimilar substrate materials used for pressure vessels and piping systems operating in excess of 500bar

This is to certify that the above-named applicant has completed the Coventry University Ethical Approval process and their project has been confirmed and approved as Low Risk

Date of approval:
12 August 2019

Abstract

High-temperature brazing is a joining technique being widely applied in the fabrication of engine components for the aerospace and automotive industries. Experimental evidences showed that brazed joints had enhanced mechanical strength when compared to the bulk filler metal. The strength enhancement was almost exclusively attributed to the stress triaxiality induced by the mechanical constraint of the base metal. In other words, strain heterogeneity would present in a brazed joint and is always associated with the enhanced mechanical strength. However, previous investigations provided neither a quantitative evaluation of stress triaxiality nor the influence of joint microstructures. Thus, the strengthening mechanism of brazed joints deserve further investigation and experimental verification.

The aim of this research is to identify the strengthening mechanism of brazed joints and quantify the effect of joint microstructure and mechanical constraint. The primary objectives are: 1) to determine the fracture strength and fatigue life of the Type 304 stainless steel brazed joints processed by pure copper; 2) to characterise the microstructure of the brazed joint and evaluate its contribution to the overall joint strength; 3) to quantify the stress triaxiality level and to estimate the influence of mechanical constraint; 4) to provide an experimental evidence for the presence of mechanical constraint. Key findings are summarised as follows.

Firstly, the mechanical strength of brazed joints as a function of the joint interface roughness was determined through uniaxial tensile and fatigue testing. This was to investigate whether the joint mechanical strength could vary with different interface roughness conditions. Key findings have indicated that the brazed joints showed enhanced mechanical strength when compared to the filler metal. In addition, the interface roughness levels had little influence on the mechanical strength. This is because all the brazed joints failed entirely within the joint centre (i.e. inside the filler metal) rather than at the interfacial region, as revealed by SEM based fractography study.

Secondly, microstructural characterisation has revealed a two-phase microstructure within the joint region: the star-shaped Fe-Cu-rich precipitates and the copper matrix. Theoretical evaluation of the collected microstructural data has suggested that Cu-Mn solid-solution dominated the overall strengthening, whereas contributions from precipitation hardening as well as grain-size strengthening were negligible.

Finally, the mechanical constraint was revealed by comparing the fracture strengths of two identical joints but with their interfaces orientated at either 90° or 45° with respect to the

loading direction. The 45° joint configuration had a lower fracture strength as compared to the 90° counterpart, as a result of the reduced mechanical constraint level. The Bridgman necking criteria was then applied to derive the longitudinal flow stress at sample fracture for the 90° brazed joint. The discrepancy between the theoretically calculated and experimentally determined strengths was judged as the influence of mechanical constraint. Thus, the enhanced mechanical strength of brazed joints is a concurrent consequence of (i) microscopic Cu-Mn solid-solution strengthening and (ii) macroscopic mechanical constraint.

In addition, geometrically necessary dislocation (GND) distribution was mapped by using electron backscatter diffraction (EBSD). The pile-up of GNDs was observed at the base-filler metal interface for the 90° joint. This observation suggests that GNDs were introduced to accommodate deformation incompatibility imposed by the mechanical constraint. This finding is thus considered as an experimental (microscopic) evidence for strain inhomogeneity due to the presence of mechanical constraint.

Acknowledgements

I am sincerely grateful to my supervisors Prof. Bo Chen, Prof. Xiang Zhang and Dr. David Parfitt, for their numerous discussions, continuous encouragements and fruitful arguments over the course of this study. In particular, I would like to thank Prof. Bo Chen to provide the considerable opportunities for collaborative research works.

In addition, I appreciate the great support and technical suggestion from Dr. Xiaodong Hou. I would also like to thank Prof. Steve Jones for taking this PhD interview and allowing me to start this research work at Coventry University.

Prof. Peter Flewitt from the University of Bristol has provided extensive research support and I would like to express my thanks to him. Furthermore, I would like to thank Prof. João Quinta da Fonseca and Prof. Michael Preuss for the fruitful discussion on experimental design at the Material Science Centre, University of Manchester.

I extend my thanks to the technical staff working at the workshops and laboratories: Steve Damms, Rizwan Tai, Steve Allitt, Barry Meek. All of them have provided a great help for manufacturing specimens and assisting me to use the equipment. Thanks are due to Vinay Patel and Karl Tassenberg for their technical guidance on EBSD scan at the Advanced Microscopy Centre, University of Leicester. I would also acknowledge Dr. Gareth Hughes and Dr. Ian Griffiths for their extensive support on FIB-lift out and TEM session at the Department of Materials, University of Oxford.

The numerous researchers at the Faculty of Engineering, Environment & Computing have provided great motivation for this PhD journey. In particular, I wish to thank Dr. Hua Guo for his suggestion over the preparation of this thesis. I would also express my thanks to Dr. Satam Saha, Dr. Yiding Liu and Deepak Sharma for their encouragement.

Last but not least, I would like to thank my parents, Mr Jiang Li and Mrs Li Ding, my uncle Mr Yi Mao and aunt Mrs Bin Ding for their support. I would also express my thanks to my girlfriend Miss Fanqi Sun for her endless encouragements.

This project was funded by Coventry University, UK.

Publications

[1] Y. Li, X. Zhang, D. Parfitt, S. Jones, B. Chen, *Characterisation of microstructure, defect and high-cycle-fatigue behaviour in a stainless steel joint processed by brazing*, Mater. Charact.

[2] Y. Li, D. Parfitt, P. E. J. Flewitt, X. Hou, J. Quinta de Fonseca, B. Chen, *Microstructural considerations of enhanced tensile strength and mechanical constraint in a copper/stainless steel brazed joint*, Mater. Sci. Eng. A.

Table of contents

List of tables

List of figures

Nomenclature

Note: units for all of these nomenclatures have been given in the relevant places in the text.

a	Internal radius of tensile specimen at the minimum cross section
A	Initial defect size (area) within the brazed joints
b	Burgers vector
c	Molar ratio of solute elements in the copper matrix
C	Material constant used in Paris law equation
C_2	Material constant used for calculation of initial fatigue crack growth rate
d	Average grain size
D	Diffusion coeficient
f	Volume fraction of the precipitates
G	Shear modulus
$\{hkl\}$	A particular set of crystallographic planes
(hkl)	A specific crystallographic plane
k	Material constant used in Hall-Petch equation
ΔK	Stress intensity factor range
L *and* L'	Thickness of tensile specimen before and after loading
m	Material constant used in Paris law equation
M	Taylor factor
r	Average radius of the precipitates
R	Radius of external curvature of the necking profile
R_a	Surface roughness
R_{ratio}	Stress ratio for fatigue testing
t	Diffusion time
$[uvw]$	A specific crystallographic direction
W *and* W'	Width of tensile specimen before and after loading
x	Diffusion distance
α	Nye dislocation tensor

$\delta_{\text{matrix-precipitate}}$	Lattice constant misfit between the copper matrix and precipitates
$\delta_{\text{matrix-solute}}$	Lattice constant misfit between the copper matrix and solute element
δ_{ss}	Interaction parameter in substitutional solid solution-hardening equation
ε	Tensile strain
θ_{ij}	Misorientation
κ	Lattice curvature
λ	Interparticle spacing between the precipitates
ρ_{G}	Density of geometrically necessary dislocations
ρ_{S}	Density of statistically stored dislocations
$\Delta\sigma$	Applied stress range for fatigue testing
σ_0	Yield strength of single crystals
σ_1, σ_2, σ_3	Principal stresses
σ_a	Stress amplitude for fatigue testing
$\sigma_{\text{Coherency}}$	Strengthening induced by coherency strain hardening
σ_{e}	von Mises equivalent stress
σ_{f}	Fracture stress
$\sigma_{\text{Hall-Petch}}$	Strengthening induced by grain size strengthening
σ_{m}	Hydrostatic
σ_{Orowan}	Strengthening induced by dislocation-looping mechanism
σ_{r}, σ_{θ}	Transverse stress components in a necking region
σ_{T}	True stress at sample fracture
σ_{TB}	Longitudinal flow stress at sample fracture
σ_{y}	Yield stress
ν	Poisson's ratio
Φ	Euler angles

Chapter 1. Introduction

1.1 Brazing of metallic materials

Brazing is a joining technique that differs from fusion welding as it does not melt the base metals. It is widely applied in the fabrication of engine components for the aerospace and automotive industries because of the minimised thermal distortion. Copper is widely used as the filler metal for brazing of stainless steels due to its favourable wetting behaviour [5]. In addition, the magnitude of thermal residual stress is usually limited because of the slow heating and cooling processes that a work piece would encounter.

Experimental evidences [6,7] showed that copper brazed steel joints had enhanced mechanical strength when compared to the bulk filler metal. For example, Kavishe and Baker [7] brazed Ni-Cr-Mo low-alloy steel with copper and it was found that the tensile strength of the joint was three times of that of the filler metal. It is believed that the strength enhancement of brazed joints was almost exclusively attributed to the mechanical constraint of the base metal [8–10]. Upon tensile loading, the plastic flow of brazed joint was laterally restricted by the base metal due to material property mismatch, resulting in a triaxial stress state within the joint region [9]. In other words, shear stresses developed within a brazed joint cannot propagate through the high strength base metal, leading to stress triaxiality. Such a triaxiality was claimed to be the reason for the increased tensile strength of the joint [8]. In addition, West et al. [10] found that the transverse stresses at the base-filler metal interface increased as the joint thickness decreased, causing extra restriction on joint deformation. This implies that the mechanical constraint can vary with different joint designs, i.e. by altering the triaxial stress state. The term “mechanical constraint” is frequently adopted to explain the enhanced mechanical strengths for brazed joints [9], but without a mechanistic-based justification. Additionally, previous investigations provided neither a quantitative evaluation of stress triaxiality nor the influence of brazed joint microstructures. Thus, the strengthening mechanism as well as the plastic flow of brazed joints deserve further investigation and experimental verification.

Because of the high-temperature brazing process, a range of complex microstructures are produced in brazed joints. Since the melting point of pure copper is 1085° C, the stainless steel brazed joints are usually processed above 1100°C. At these high temperatures, up to 3.5 wt.% iron can be dissolved in copper, whereas the corresponding solubility at room temperature is

negligible. Consequently, iron precipitation as well as non-equilibrium impurity segregation can arise during the subsequent cooling process, forming secondary phases within the joint region. Detailed investigations of the influence of iron on precipitation morphology and crystal structures have been undertaken by Chen et al. [11,12], where additional iron was introduced to strengthen copper alloys via precipitation hardening effect [13]. Therefore, it is critical to characterise the microstructure of a brazed joint to capture the distribution of diffused elements, and to evaluate its potential influence on mechanical strength.

In the meantime, various studies have reported the influence of joint interface roughness on the mechanical strength of brazed joints [14–18]. The interface roughness here refers to surface roughness of the base metals prior to brazing. For example, the influence of interface roughness on tensile and high cycle fatigue (HCF) strength of mild steel brazed joints was studied by Suezawa [17]. A wide range of interface roughness levels were introduced by adopting different P-grade SiC papers from P120 to P600. The maximum tensile strength of 425 MPa and the HCF fatigue limit of 172 MPa were revealed for the brazed joint that had been prepared with P120. This work indicates that a coarser joint interface condition led to a higher mechanical strength, which was qualitatively attributed to the enlarged bonding area. To this end, one might raise a question as to whether an enlarged bonding area (due to asperities) will promote the mechanical constraint effect and thus cause additional strengthening. Therefore, it is noteworthy to verify the influence of interface roughness on the mechanical strength of stainless steel brazed joint under.

For engineering design of brazed joints, an in-depth investigation of the mechanical properties in conjunction with the mechanism of enhanced mechanical strength is required to ensure the structural integrity and sustainable operations. We will firstly design and test stainless steel brazed joints to evaluate their fracture strength and fatigue life as a function of the interface roughness. This is followed by multi-scale microstructural characterisations of the brazed joint using a range of electron optical tools. Theoretical calculation of the joint strength based on the microstructural data as well as the Bridgman necking criteria [19] was performed to correlate with the experimentally determined value. Furthermore, braze assemblies were designed to create two joint configurations with their interfaces orientated at 45° and 90° with respect to the loading direction. The design of 45° joint in principle would help to reduce the influence of mechanical constraint when compared to the 90° joint. This would then enable a direct comparison of the plastic flow capability and the overall strength of brazed joints under different mechanical constraint levels.

Besides the macroscopic strengthening effect, microscopic aspect of the mechanical constraint is also of interest. Studies demonstrated that electron backscatter diffraction (EBSD) can be used as a reliable technique for characterising dislocation densities close to interfaces at micrometre scale. For example, Kadkhodapour et al. [20] performed an experimental study of geometrically necessary dislocations (GNDs) within dual phase steels where GNDs close to the ferrite-martensite phase boundaries was one order of magnitude higher than those at grain interiors, causing local strain hardening. In addition, Jiang et al. [21] studied the evolution of GNDs in copper during tensile loading by using EBSD combined with cross-correlation. In this context, interrupted tensile tests were conducted on the 45° and 90° brazed joints in the current work. This was followed by post-mortem EBSD analysis, as a new approach for plastic flow characterisation, to investigate dislocation characteristics as well as GND distribution within the brazed joints. These findings would reveal potential deformation incompatibility in the vicinity of the base-filler metal interface and thus serve as an experimental evidence for the presence of mechanical constraint.

1.2 Aim and objectives

The present work aims at identifying the strengthening mechanism of stainless steel brazed joints and quantify the effect of joint microstructure and mechanical constraint. The primary objectives are:

1) To determine the tensile and fatigue strengths of the Type 304 stainless steel brazed joints processed with pure copper

2) To perform a full characterisation of the joint microstructure and to evaluate its potential influence on the overall joint strength

3) To quantify the stress triaxiality levels and to estimate the effect of mechanical constraint on joint strength

4) To understand the microscopic aspect of mechanical constraint

1.3 Structure of thesis

Chapter 2 gives a brief introduction to ductile fracture of metals as well as stress triaxiality encountered in uniaxial tensile testing. This is followed by a brief review of EBSD-based dislocation evaluation technique. Furthermore, dislocation structures together with their

crystallographic characteristics are detailed, as these are closely related to the deformation behaviour of stainless steel brazed joints processed by pure copper. Specific materials and experimental techniques applied in the current work are described in Chapter 3.

Mechanical strength of the stainless steel brazed joints was examined by using uniaxial tensile and high cycle fatigue testing. Details have been reported in Chapter 4. In addition, a correlation between the joint defect and the corresponding fatigue life was performed, which is reported in Chapter 4.

Chapter 5 presents a multi-scale microstructure characterisation of the stainless steel brazed joints. This includes the grain size and texture analysis of the as-brazed joint, together with a statistical consideration of Fe-Cu precipitation size and distribution. In addition, microstructural contribution to the overall tensile strength is theoretically evaluated.

The contribution of mechanical constraint towards the overall joint strength was evaluated by adopting the Bridgman necking criteria. Details are reported in Chapter 6. Furthermore, microscopic aspect of the mechanical constraint is reported, which was revealed by comparing plastic flow of brazed joints orientated at 90° and 45° with respect to the loading direction.

Finally, a summary of research findings is given in Chapter 7, together with some future works.

Chapter 2. Literature review

2.1 Introduction

This chapter gives a brief review of ductile fracture process of metals and the role of stress triaxiality in Section 2.2. In Section 2.3, dislocation structures and the corresponding examination methods are given. Lastly, characteristics of geometrically necessary boundaries and incidental dislocation boundaries are discussed. The aim of this chapter is to briefly introduce the plastic deformation as well as the microscopic dislocation motion for ductile metals, which are key and essential to the discussion in Section 6.

2.2 Ductile fracture and stress triaxiality

The failure of ductile metals that includes tensile and shearing fracture depends on the stress state. This is based on the internal process of nucleation, growth and coalescence of microvoids [22]. For ductile materials, microvoids nucleate at inclusions or second-phase particles, either by decohesion of the particle-matrix interface or by fracture of the particle [23]. Upon continued deformation, these microvoids grow and coalescence by internally necking down or shearing of the ligaments depending on the local stress state [24]. This would create a continued fracture path, which propagates until sufficient loss of cross sectional area and leads to final failure. The ligament here refers to the material in between two neighbouring microvoids, as shown in Figure 2-1.

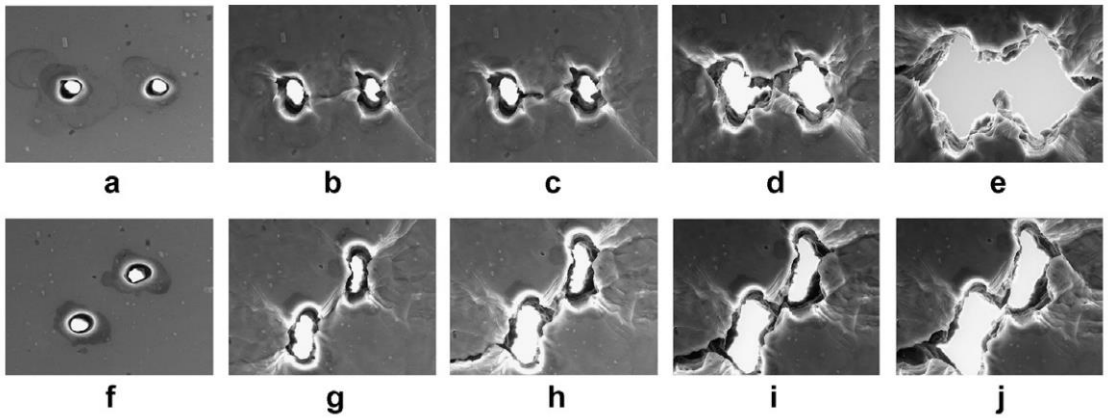

Figure 2-1: 1 (a)-(e) necking down of the ligament and (f)-(j) shearing of the ligament in between two neighbouring microvoids

Dimples on fracture surfaces are formed by coalesced microvoids [25]. Experimental observation clearly indicates that the lateral expansion of microvoids is primarily controlled by the stress state. For specimens failed under shearing mode, the fracture surface was relatively flat without clear dimples. For specimens failed under combined "tensile and shearing" mode, the nucleated microvoids would be elongated by the shear stress, which resulted in distorted shaped dimples. Both the macroscopic failure mode as well as microscopic fracture mechanism depend on the local stress triaxiality, which is defined as ratio of the mean stress (hydrostatic) to the von Mises equivalent stress. The mean stress σ_m is calculated as:

$$\sigma_m = \frac{\sigma_1 + \sigma_2 + \sigma_3}{3} \tag{2-1}$$

where σ_1, σ_2, and σ_3 are the principal stresses. The von Mises equivalent stress σ_e is calculated as:

$$\sigma_e = \sqrt{\frac{(\sigma_1 - \sigma_2)^2 + (\sigma_1 - \sigma_3)^2 + (\sigma_2 - \sigma_3)^2}{2}} \tag{2-2}$$

Studies indicated that ductile fracture mode would change from tensile dominated failure to shearing dominated failure with decreased stress triaxiality (σ_m/σ_e) [26]. For an axisymmetric specimen under uniaxial tensile loading, the stress state becomes nonuniform upon the onset of necking. The necking area is a localised region where most of the strains accumulate while the rest of the specimen undergoes negligible change in dimension. As a result, further lateral contraction is restricted by the un-necked region, thus the stress state changes from uniaxial to triaxial. The corresponding stress triaxiality is maximised at the specimen centre and causes microvoid nucleation. Bridgman [19] formulated a geometric approximation to obtain the longitudinal flow stress that accounts for the presence of the transverse stress components, under the assumption of uniform strain distribution in the minimum cross-section.

Experimental observation of circumferentially notched specimens revealed elevated flow stress and decreased strain, a situation in which deformation around the notch root is mechanically constrained [27–29]. For a notched specimen, a mass of less-stressed material exists above and below the notch. The material in the thinnest cross section of the notch wants to contract laterally because of the Poisson effect, but it is constrained by the material above

and below. This constraint causes both radial and transverse stresses in addition to the tensile stress, leading to a triaxial stress state. This in turn leads to an elevation in the stress-strain curve because higher applied stress in the tensile direction is needed to cause fracture of the specimen [23,30]. That is to say, the elevated flow stress of notched specimen is a consequence of the mechanical constraint effect. Numerical modelling on the basis of finite element analysis (FEA) [31] revealed increased stress triaxiality level for circumferentially notched specimens, being 0.6 at specimen centre and gradually decreased to 0.33 towards the edge. Thus, the mechanical constraint effect in notched specimens is also substantiated by the high stress triaxiality levels.

Wenchao et al. [29] conducted tensile testing of Q460 steel to investigate its mechanical strength under different stress states where various stress triaxiality levels were introduced by creating specimens with different notch radius. The stress triaxiality level was found to increase with decreased notch radius, leading to decreased fracture strains. To this end, it is concluded that the mechanical constraint effect in notched specimens is affected by the notch geometries, and it can be characterised by calculating the stress triaxiality values.

Based on the information above, the principle of mechanical constraint effect in brazed or soldered joints is identical to that in the notched specimens. Although a notch is not always introduced in brazed joints, plastic flow of the joint material is mechanically constrained by the base metal (i.e. above and below the brazed copper) due to elastic-plastic incompatibility, leading to a triaxial stress state. Therefore, the Bridgman necking criteria is adopted in the current study to derive the longitudinal flow stress at sample fracture of the brazed joints. Furthermore, stress triaxiality levels of angled specimens at 30° to 45° (with respect to the tensile axis) were well below 0.3, leading to shearing-dominated fracture [29]. It is therefore inferred that the 45° brazed joint has a low stress triaxiality, hence a reduced mechanical constraint effect when compared to the 90° configuration. The design of 45° brazed joint aims at promoting a shear-type of failure as the critically resolved shear stress is maximised when inclined at 45° in respect to the tension axis.

2.3 Evaluation of dislocation and dislocation structures

2.3.1 Lattice curvature and electron backscatter diffraction

Dislocation characterisation is key to the understanding of plasticity. Dislocations are generally revealed by observing the localised lattice distortion via diffraction [32]. Historically, dislocations were characterised as discrete phenomena via transmission electron microscopy (TEM). While TEM technique can detect distortion fields at length scales small enough to resolve individual dislocations, the correlation between these localised measurements to their effect on the corresponding macroscopic properties is difficult. This is caused by the large number of dislocations involved. This challenge eventually led to the development of continuum dislocation microscopy, through which dislocations can be modelled as continuous fields rather than discreet ones. Continuum dislocation microscopy depends on the observation of local lattice distortion gradients.

With the development of automated electron backscatter diffraction microscopy, lattice orientation can be readily revealed at micrometre scales. Some studies [33–43] suggested that dislocation density can be derived via the Nye tensor components [44] from EBSD orientation data. EBSD technique allows measuring the crystal orientation at each measurement point on the sample surface. Hence, the misorientations θ_{ij} can be calculated between any two measurement points i and j as shown in Figure 2-2 below. The presence of dislocations in a deformed lattice may introduce a measurable lattice curvature. The result of this lattice curvature is an overall Burgers vector, which explains the deformation from point to point at the continuum scale.

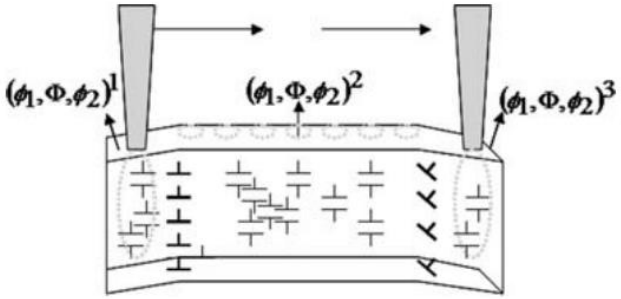

Figure 2-2: Schematic illustration of change in orientation (as represented by Euler angles: Φ_1, Φ, Φ_2) as the electron beam scans across the surface of a crystalline material. Note the

orientation changes only when the beam crosses an array of dislocations that has a net non-zero Burgers vector

Assuming the contribution of the elastic field to the local misorientation is negligible [45], the local misorientation data can therefore be directly converted into a dislocation density. In order to determine the dislocation density at each measurement point, the local misorientation θ_{ij} is averaged over the neighbouring points located at a fixed distance from the pixel of interest. This local average misorientation θ is the well-known KAM value (Kernel Average Misorientation angle proposed by all EBSD data processing software package), provided that KAM is calculated using only the peripheral pixels and not all the pixels included in the kernel.

Using continuum dislocation mechanics developed by Nye and Kroner [46,47], the lattice information can be related to the dislocation content of the material. These techniques were developed into the first continuum dislocation microscopy technology [35,38,47–49]. Calculated dislocation densities may be used to evaluate existing plasticity models [32] or applied directly to meso-scale calculations that incorporate GND evolution and effects [50,51]. Note that continuum dislocation mechanics only observes geometrically necessary dislocations. GNDs are dislocations that are associated with long range distortion gradients in a material, relating to heterogeneous deformation. To establish a correlation between the accommodated plastic deformation and the stored dislocations, theoretical concepts of statistically stored dislocations (SSDs) and geometrically necessary dislocations (GNDs) were introduced.

2.3.2 GNDs and SSDs

Nye [46] firstly noted that dislocation networks are required to maintain the geometrical continuity of a material possessing strain gradient in its deformed state. Ashby [52] later on described these as GNDs at a continuum scale. SSD and GND were historically distinguished by their arrangement and distributions. Homogeneous deformation is accompanied by the storage of SSD [53], which are in the form of tangles, dipoles, multipoles. As a consequence, their arrangements do not give rise to a significant lattice curvature and hence their Burgers vector is practically zero. In contrast, GNDs are introduced to accommodate strain gradient encountered during inhomogeneous plastic deformation, which often gives rise to lattice curvature.

Since each dislocation induces a slight lattice curvature at the local scale, each dislocation in principle could be defined as GND. Therefore, the distinction of SSD and GND strongly

depends on the observation scale and on the accuracy of the measure used to determine the misorientations of the crystal lattice. To this end, it was concluded in [32] that there was no fundamental difference between SSDs and GNDs apart from their distributions. For example, all dislocations within a Burgers circuit whose distortion effects are not cancelled by other dislocations are considered as GNDs. Dislocations within the same Burgers circuit that collectively cancel each other's distortion are SSDs. If the Burgers circuit is small enough to contain one single dislocation that is similar to TEM dislocation imaging, the dislocation can be considered as a GND at that length scale. On the other hand, more dislocations may cancel others of opposite signs and form dislocation dipoles without net geometrical effect are SSDs, if a larger Burgers circuit is introduced. For GND evaluation technique on the basis of EBSD, the size of the implicit Burgers circuit is related to the chosen step size. Therefore, GND density can be evaluated through EBSD and the calculated density will depend on the step size used to measure the lattice distortion [37]

2.3.3 GNBs and IDBs

Correlation between plastic deformation and the resulting microstructure has been experimentally explored by TEM. These studies indicate that individual dislocation or small groups of dislocations can be observed at low strains only [1]. For materials with medium to high stacking fault energy, dislocations can change their slip planes and form well-organised dislocation structures. Such non-random dislocation structures have been intensively characterised by TEM in many materials, for example, Cu [54], Al [54–57], Ni [58], 304 L austenitic stainless steel [56] and Fe [59]. At increased strains, the characteristic features are dislocations forming extended boundaries with relatively large misorientations across them. As misorientation increases with dislocation density, there are two types of dislocation walls that are usually associated with higher and lower misorientations. Kuhlmann-Wilsdorf and Hansen [60] termed these dense dislocation walls as geometrically necessary boundaries (GNBs) and incidental dislocation boundaries (IDBs). The formation of GNBs is resulted from slip system differences on each side of the boundary, whereas the formation of IDBs is random because it results from statistical mutual trapping of glide dislocations. An illustration of GNBs and IDBs are given in Figure 2-3. As can be seen, dislocation boundaries developed in pure Ni that had deformed to a rolling reduction of 20%. The schematic solid lines represent GNBs and the speckled lines show the IDBs.

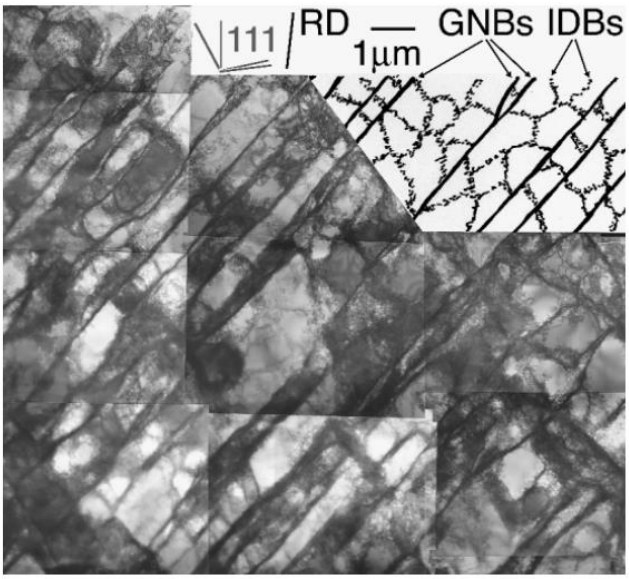

Figure 2-3: Transmission electron micrograph showing the arrangement of dislocation boundaries developing in pure nickel deformed to a rolling reduction of 20%. The attached schematic shows the arrangement of GNBs with solid lines and IDBs with speckled lines. The rolling direction is marked as RD as well as the trace of the (111) slip planes [1]

Misorientations across the dislocation boundaries increase with the increased strain level, and the rate of increase distinguishes IDBs and GNBs [57,58,61]. Figure 2-4 shows that significant misorientations are formed for both IDBs and GNBs at relatively low strain levels. In addition, misorientation angles of GNBs can exceed 15° ($\theta > 15°$) at high strain levels, which is equivalent to ordinary grain boundaries, Figure 2-4. Dislocation density within dislocation boundaries is of the order of θ/b. Note θ/b represents the minimum dislocation density within a chosen Burger circuit because some dislocations may cancel others with opposite sign (e.g., $+b$ and $-b$), which does not contribute to misorientation θ. Therefore, at a microscopic continuum scale, GNDs are dense dislocation walls composed of GNDs, whereas IDBs are groups of SSDs being developed by mutual trapping of dislocations in the form of tangles and dipoles [1].

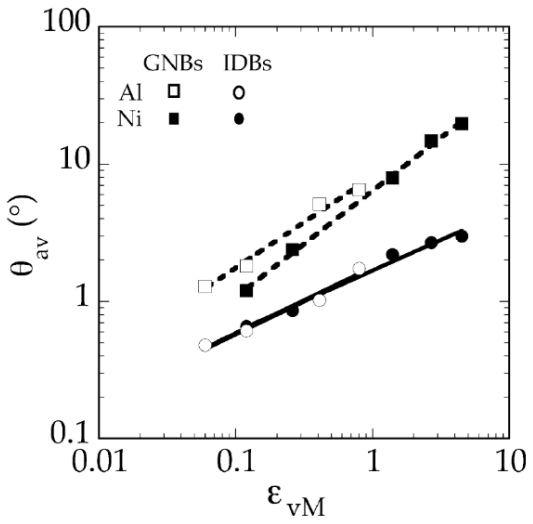

Figure 2-4: Relationship between the average misorientation and the applied von Mises strain for high purity cold rolled Al and Ni [1]

The magnitude of misorientation angles and boundary spacings vary substantially with the metal type, for example being smaller in copper than in aluminium, because of the differences in the active slip systems and stacking fault energies [62–64]. The evolution of misorientation angles increase with increased strains, whereas the boundary spacing decrease. The average misorientation angles for GNBs is found to increase exponentially with the strain [57]. The crystallographic GNB plane varies systematically with the grain orientation and the crystal structure of the metal. The grain orientation dependence of the crystallographic GNB alignment is believed to originate from an underlying dependence of the active slip systems, implying that the GNB alignment is a new indirect way to investigate slip systems. GNB boundaries often consist of planar segments, which are parallel but slightly shifted with respect to each other as demonstrated in the TEM image below, Figure 2-5. The individual segments are planar as supported by the straightness of their traces, however, the steps in between may give the GNBs a curved character over longer distances [2,65,66].

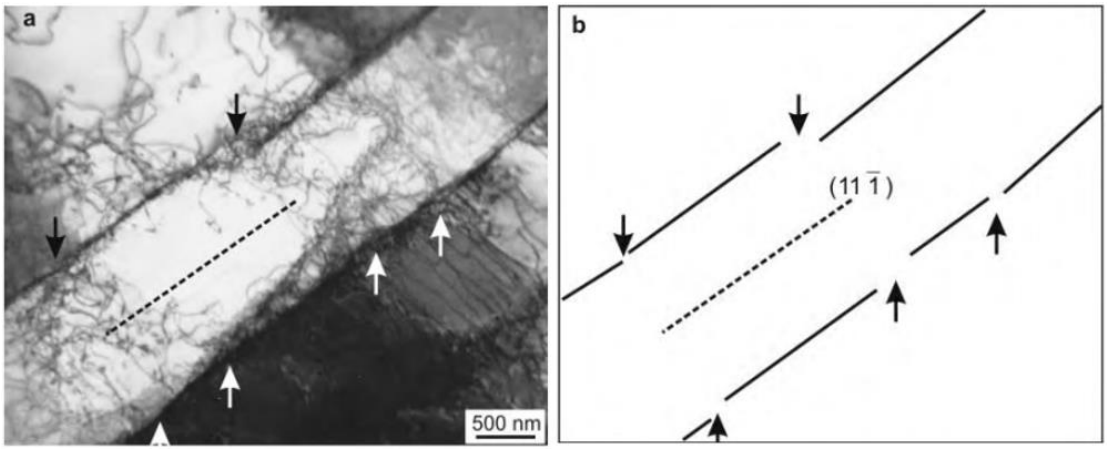

Figure 2-5: GNB plane determination for grain with GNBs aligned with the $(1\,\bar{1}1)$ slip plane. (a) an edge-on image of two GNBs taken in the beam direction of $[1\bar{2}\,\bar{1}]$. Small steps are indicated by arrows. (b) A sketch showing an approximately parallel relationship between the straight segments forming the GNB [2]

2.4 Summary

Ductile fracture is reviewed in this chapter together with the stress triaxiality. The triaxial stress state in brazed joints induced by the mechanical constraint of the base metal is analogy to that in a necking region. Therefore, the Bridgman necking criteria will be adopted in the current study to derive the longitudinal flow stress. In addition, dislocation/dislocation structures of ductile metals are discussed as these are essential in characterising plastic flow of the brazed joints. Details of the dislocation structures are given in Chapter 6.

Chapter 3. Materials and experimental techniques

3.1 Introduction

Chapter 3 provides a short description of the material used in the present study combined with the key experimental methods including microstructure evaluation techniques and mechanical testing facilities. Type 304 austenitic stainless steel was selected as base metals for manufacturing the brazed joints. This was the material typically used in manufacturing of engine components.

In Section 3.2, the preparation and manufacturing of the brazed joints are detailed. The manufacturing method of the brazed joints was the same for all the specimens fabricated in this PhD work. In Chapter 3.3, the microstructure characterising tools are described. These techniques were used to investigate brazed joint microstructure in the as-brazed condition presented in Chapter 5 and the partially strained condition presented in Chapter 6. In Section 3.4, mechanical testing facilities and corresponding methods used in this research are given.

3.2 Fabrication of brazed joints

3.2.1 Materials

The type 304 stainless steel was supplied by Rapid Metals, UK, in the form of long bars of square cross-sections. Pure copper (99.99% purity) was used in the current work as the filler metal for brazing. Copper foil of 125 μm thick (supplied by Alfa Aesar, Thermo, UK) was used to ensure the uniform thickness of the brazed joint because it serves as filler metals as well as spacers. The chemical composition of the stainless steel is shown in Table 3-1.

Table 3-1: Chemical composition of the Type 304 stainless steel

Base metal	Chemical composition (wt.%)							
Type 304	Ni	Cr	Mn	Si	C	P	S	Fe
stainless steel	9.25	19.00	2.00	1.00	0.08	0.05	0.03	Balance

3.2.2 Joint assembly design

The supplied stainless steel bars were firstly cut into rectangular blocks by using electric discharge machining (EDM) technique. This was followed by degreasing and cleaning (with acetone) in an ultrasonic bath for 10 mins. Figure 3-1(a) shows the sample fabrication process where the copper foil was inserted in between two blocks of stainless steel base metals, at 90° orientation with respect to the loading direction. The assembly was then tack welded to hold the pieces together during brazing; the black dots in Figure 3-1(a) indicate the locations of the tack welds.

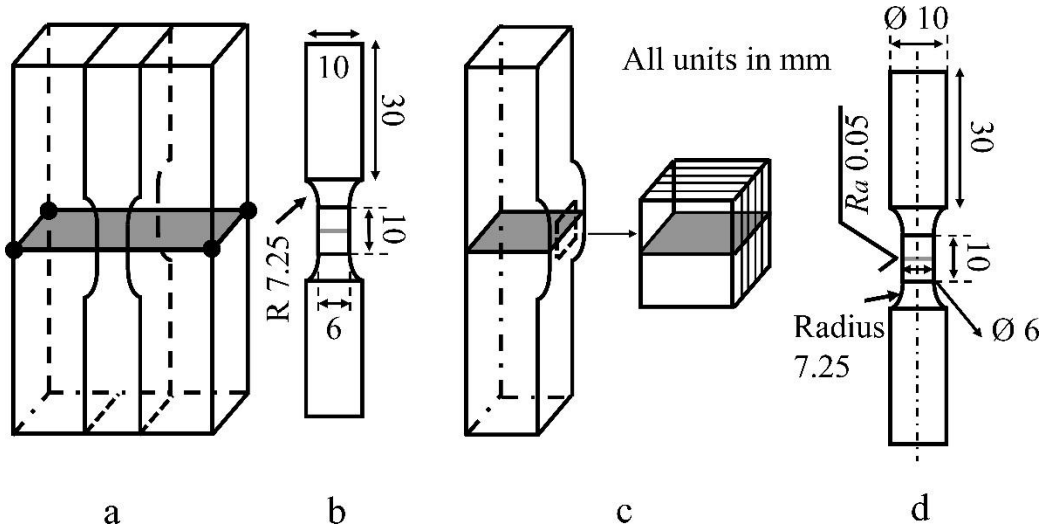

Figure 3-1: Brazed joint configurations with respect to the longitudinal loading direction: (a) joint at 90°; (b) flat tensile test specimen and dimensions (thickness = 3 mm); (c) sampling location for microstructure characterisation; (d) cylindrical specimen for high cycle fatigue tests

3.2.3 Brazing process

Brazing was performed in a conveyor belt furnace in a hydrogen atmosphere. Figure 3-2 presents the thermal history of the brazing process. Three primary stages were included: heating, brazing and cooling. The initial temperature increase in Figure 3-2 was caused by the flame curtain that occurred when the tack welded sample assembly moved close to the entrance of the heating zone. The flame curtain was used to ensure a reduced atmosphere. During heating, the temperature rapidly increased from ~200 to 1080 °C within 6 mins. The sample assembly was then kept at the brazing temperature of ~1120 °C for 10 mins. The sample assembly was

then cooled to room temperature within 30 mins after the brazing stage, Figure 3-2. This brazing process applied to all the joint fabrication throughout this PhD work.

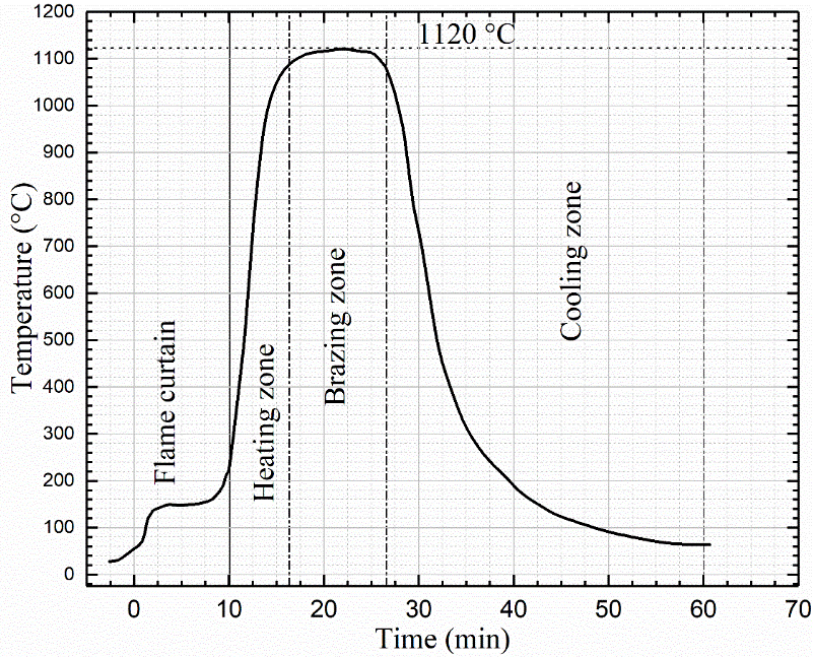

Figure 3-2: Thermal history adopted in the current study for the manufacturing of brazed joints

After brazing, the central portion of the as-brazed joint assembly was extracted by electrical-discharge-machining (EDM) to acquire dog-bone profiles, as indicated by dashed lines in Figure 3-1(a). The extracted dog-bone assembly was sliced into flat tensile test specimens with 3 mm in thickness. For the gauge section of the specimen, the width is 6 mm and the length is 10 mm; the griping area has 10 mm width and 30 mm in length. After specimen extraction, the remaining joint assembly was used for microstructural characterisation and the sampling location is indicated by dashed rectangular box in Figure 3-1(c). The extracted rectangular block was sliced into multiple pieces, Figure 3-1(c), and at least five different regions were examined to obtain statistically significant information about the joint microstructure. To avoid crack initiation from the corners of the specimens, cylindrical specimens were also fabricated for the high cycle fatigue testing in the current work. This was achieved by firstly extracting cylinders from the joint assembly, as shown in Figure 3-1(a), followed by subsequent machining to obtain the desired design. The dimensions of the cylindrical specimens are detailed in Figure 3-1(d).

3.3 Microstructure characterisation techniques

3.3.1 Metallographic preparation and scanning electron microscopy (SEM)

Joint microstructure characterisation was performed on the basis of the 90° joint configuration, Figure 3-1(c). A standard metallographic sample preparation was used, this included sequentially grinding to P1200, polishing to a finish of 1 µm, and finally OPS polishing using a vibro-polisher for 12 hours with 0.02 µm colloidal silica.

The scanning electron microscope (SEM) is one of the most versatile instruments for investigating microstructure of materials. Under electron bombardment, a variety of different signals are generated from the material including secondary electrons, backscattered electrons, characteristic X-rays. SEM expands the resolution range to a few nanometres, thus bridging the gap between optical microscopy and transmission electron microscopy (TEM). In addition, a large depth of field can be achieved for these instruments because the electron beam is focused from the aperture onto the specimen surface over a distance of typically ~15 mm. A relatively high resolution offers possibilities for revealing detailed microstructures of polished and etched cross-sections of the specimens. A combination of high resolution and large depth of view makes SEM well suited to examine fractography. Energy dispersive X-ray microanalysis using equipment routinely attached to the SEM provides qualitative and quantitative analysis of the chemical composition with a typical lateral resolution of a micrometre and a typical depth resolution of a few tenths of a micrometre [67].

In the present work, the microstructure of the brazed joints was revealed using a Zeiss Gemini SEM at 15 kV under the backscattered electron (BSE) and second electron (SE) imaging mode. Cross-sectional view of brazed joints was revealed using BSE-imaging mode, whereas fractography was conducted using SE-imaging mode. In addition, High-magnification SEM images were collected and processed using ImageJ programme to obtain the size, distribution and volume fracture of potential secondary phase particles based on 500 measurements. Furthermore, fractography was performed on the failed specimens to verify the fracture mechanism for both tensile and fatigue testing. This allowed to distinguish the fatigue crack initiation, propagation and final fracture zone. Additionally, a quantitative measure of the joint defect area within the fatigue crack initiation region was obtained by analysing the collected SEM images. For defect-bearing specimens, fatigue striation spacings in the early-stage of fatigue crack propagation were measured to provide an indicative evaluation of the

initial fatigue crack growth rate. For each specimen condition, twenty measurements were performed to determine the average value of the fatigue striation spacings. Furthermore, longitudinal cross-sections of the fractured specimens were examined using SEM to assist in understanding the fatigue failure mode of the brazed joint.

For the quantitative metallography in the current study, all the measurement was performed based on image analysis in ImageJ. For example, SEM images of secondary particles were firstly collected and imported into ImageJ. This was followed by certain adjustment including brightness and contrast, etc., so that regions of interest can be easily identified. Finally, statistics of the regions of interest, i.e., average sizes and area fraction, can be extracted by using the built-in function within ImageJ. This process was repeated when multiple SEM images were generated to acquire statically sound values. However, it is suggested to always compare data from image-processing package with those obtained manually (i.e., linear intersect method) to verify the results.

3.3.2 Electron backscatter diffraction (EBSD)

Electron backscatter diffraction (EBSD) is a SEM based technique that enables individual grain orientations, local texture, phase identification and distributions to be determined routinely on the surface of bulk samples. The first observation of a diffraction pattern in backscatter mode was reported in 1928 by Nishikawa and Kikuchi [68]. The characteristic feature of a backscatter Kikuchi pattern is the regular arrangement of parallel bright bands rather than a regular array of diffraction spots as is generated from a single crystallite. The intersections of Kikuchi bands form prominent and distinct zone axes. Fully automated methods have been developed for acquisition and indexing of Kikuchi pattern within the SEM [69] and the TEM [70,71]. EBSD patterns are generated on a phosphor screen by backscatter diffraction of a stationary beam of high-energy electrons from a volume of crystal material approximately 20 nm deep in the specimens. The electron beam is directed across the specimen based on a pre-defined grid, pausing at each point only long enough to acquire the backscatter diffraction.

The diffraction patterns are sorted according to their intensities and width, and indexing of the diffraction pattern is performed by comparing the measured interplanar angle (which correspond to the angles between the Kikuchi bands) and interplanar spacings (which are represented by the band widths) with theoretical values from the data base. Plastic deformation in polycrystals usually results in local lattice curvature, for which EBSD is well designed to

measure. Typical values for misorientation resolution using standard EBSD platforms are on the order of 0.5° [72]. Using direct pattern analysis methods, angular resolutions down to 0.01 – 0.02° can be achieved [73]. Compared to this sensitivity, plastic deformation in metals can easily cause several degrees of lattice rotation, and EBSD is therefore a useful technique for the measurement of micrometre scale lattice rotation.

EBSD pattern can be analysed either directly or through some transforms, usually Hough transform in automated analysis. One of the more important correlation between the plasticity mechanics and EBSD is the use of continuum descriptions of dislocations in describing crystal plasticity. This work was started by Nye in the 1950s and further established by Ashby and others in the 1970s [46,52]. A good review paper of these is found in the work of Arsenlis and Parks [74]. The direct correlation between GND determination and EBSD was pioneered in the last several years in the work of Adams [38,69,75] and has been adopted by several authors [40,48].

The characterisation of the microstructure of materials provides important information for the understanding of their properties. In this context, EBSD is a useful tool for sub-micron-scale crystallographic analysis materials in the SEM [76]. EBSD delivers spatially resolved crystallographic information via measurement of backscattered Kikuchi diffraction patterns that are formed by incoherent point sources of backscattered electrons within a single crystalline volume [77,78]. Compared to other diffraction techniques, Kikuchi patterns have the distinct advantage that they provide a rather extended, wide-angle view on potential point group symmetries of the phase that is probed locally by the incident electron beam.

In the current study, texture and grain size measurements of the brazed joints were conducted using EBSD on a JEOL JSM-7200F SEM at 15kV with 1 µm step size. In addition, the interrupted tensile specimens were subjected to longitudinal cross-section and metallographic preparation, followed by SEM observation and EBSD scans to reveal the plastic flow characteristics. A field-of-view of 250 × 150 µm^2 at a step size of 0.25 µm was used for EBSD scan to ensure an appropriate spatial resolution. Measuring the crystallographic orientations with small neighbouring material volumes typically enables the calculation of lattice curvature, from which the GND density can be derived using the Nye dislocation density tensor [46]. In the current study, GND densities were calculated from the lattice curvature κ approximated with a finite difference scheme applied on the misorientation $\theta = (\theta_1\ \theta_2\ \theta_3)^T$ as follows [40]:

$$\kappa_{ij} \cong \frac{\Delta\theta_i}{\Delta x_j} \tag{3-1}$$

where Δx_j is the step size (0.25 μm in this work) of the orientation map in the direction x_j. By neglecting the elastic strains, the Nye dislocation tensor α was then obtained by [79]:

$$\alpha \cong tr(\kappa).\mathrm{I} - \kappa^{\mathrm{T}} \tag{3-2}$$

its entrywise norm

$$\|\alpha\| = \sqrt{\alpha ij \cdot \alpha ij} \tag{3-3}$$

is displayed in Figure 6-8 to represent the GND density values. The calculation was performed by using ATEX software package [80] and the results were expressed in m^{-2} by dividing by the magnitude of the burgers vector *b*. EBSD-based estimation of GND density can also be performed by calculating the scalar value suggested in [81]. This method was not applied in the current study.

3.3.3 Focused ion beam (FIB)

Focused ion beam (FIB) workstations have been produced commercially for approximately 20 years. Up to about a decade ago, these instruments were rarely found outside the microelectronics industry. However, more recently these workstations have been commonly used in a broader range of materials science field. This is because FIB instruments have achieved a spatial resolution rivalling that of the conventional SEM. Furthermore, the improved resolution, novel FIB channelling contrast effect and the capability of FIB to produce high precision milling cross-sections provide a powerful contribution [82–84]. FIB instruments are similar to conventional SEM in the construction of the column and operating principles. A beam of gallium ions replaces the electron beam, bringing with it several advantages over SEM techniques. The high mass of the ions in the beam causes sputtering of the specimen surface, which result in the removal of atoms, ions and electrons. In the case of the preparation of milled cross-sections, rough milling at a high beam current and subsequent polishing with a low beam current is used to produce micrometre scale cross-sections at specific regions of microstructural interest. Cross-sectioning reveals both topographic and subsurface information.

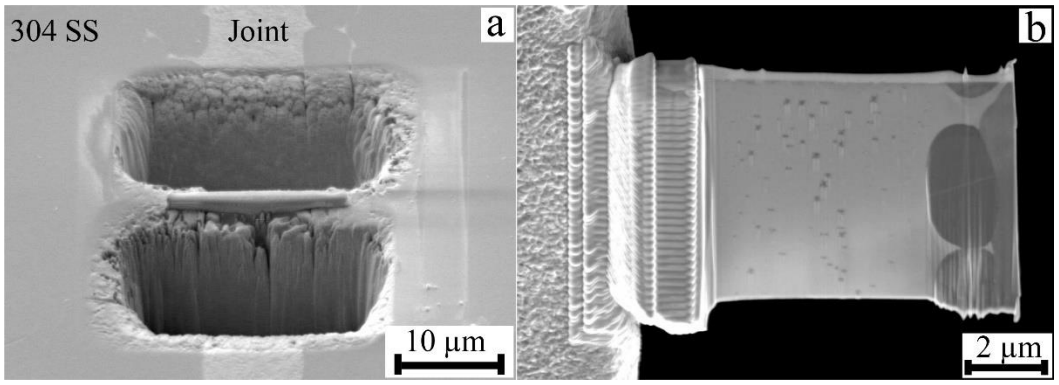

Figure 3-3: (a) FIB TEM lamella position relative to the brazed joint; (b) TEM lamella after final polish

In the current work, FIB technique was used to prepare thin specimens for TEM examination of secondary phases. This is because FIB introduces less damage to the sub-surface of the material than that introduced by the conventional preparation method. In-situ lift-out TEM sample preparation was conducted by using a focused ion beam (FIB) workstation (Zeiss Gemini 2 FIB/SEM crossbeam 540) equipped with a micromanipulator. Ga^+ ions accelerated at 30 kV were used for milling and polishing with FIB currents in descending order from 65 nA, 15 nA, 7 nA to 3 nA, Figure 3-3(a). This was followed by FIB lift-out and attachment to a copper grid by using 200 pA current to minimise the damage. The TEM sample was then cleaned at 700 pA, 300 pA and 100 pA at 30 kV, followed by final polish at 200 pA, 2kV, Figure 3-3(b). More details about FIB milling and polishing can be found elsewhere [85].

3.3.4 Transmission electron microscopy (TEM)

Transmission electron microscopy is used to reveal sub-micrometre, internal fine structure in solids. To reveal the crystal structure of second phase particles within the brazed joint, a JEOL JEM-3000F transmission electron microscope (TEM), operated at 200 kV was used for selected area electron diffraction (SAED). In addition, an atomic-resolution JEOL ARM-200F Cs corrected S/TEM, equipped with a highly efficient (Centurion) energy dispersive X-ray (EDX) system, was used for elemental analysis and atomic-scale characterisation in STEM mode (operated at 200 kV). The probe size was set to 0.1 nm with a convergence semi-angle of 22.5 mrad. The collection angle of the high angle annular dark field (HAADF) detector was in the range of 80 to 150 mrad. SAED patterns were processed using Digital Micrograph 3.5

and Gatan Microscopy Suite 2.1 to acquire lattice constants for both the copper matrix and second phase particles. In addition, orientation relationship between the second phase particles and the copper matrix was determined from the collected STEM-HAADF images by applying fast Fourier transform (FFT).

3.4 Mechanical testing

3.4.1 Berkovich nanoindentation

Nanoindentation refers to depth-sensing indentation (DSI) techniques used to obtain mechanical properties from very small volumes of material. In a traditional indentation test, an indenter is pressed into a sample with a known load and is removed. The hardness is then defined as the load divided by the area of the residual indentation and gives a measure of the resistance of the material to plastic deformation. In DSI, the load on and displacement of the indenter are continuously recorded as it is pressed into and removed from the sample. These data are subsequently analysed to determine mechanical properties. Material properties can therefore be obtained from indentations with depths as small as a few nanometres.

Nanoindentation is commonly used to determine the mechanical properties of thin films and coatings, particles and fibres, embedded phases, patterned structures, and other small volumes [86]. In this context, nanoindentation is an ideal tool for mechanical property evaluation for brazed joints as compared to traditional micro-hardness measurement. In this work, Berkovich nanoindentation was used to determine the strength of the brazed joint including regions in the vicinity of the base-filler metal interface. Positioning of the indentation was controlled with an optical microscope and an array of 10 × 5 indents were tested. Nanoindentation was conducted using force control with a nominal load of 3.5 mN and this resulted in the indent size being in the range of 2 μm to 5 μm [87]. The spacing between each individual indent was set as 15 μm (5 times the indent size) to avoid interference from the plastic zone of neighbouring indents. The hardness was derived as a function of the depth of each indent using the Oliver-Pharr method [88].

3.4.2 Testing parameters for static and fatigue tests

Uniaxial tensile tests were performed on an Instron 8802 servo-hydraulic testing system with a 50 kN load cell. Tests were conducted at room temperature with a constant strain rate of 3.3×10^{-4} s^{-1}. The axial strain was measured by an extensometer with a gauge length of 10 mm and travel distance of ± 1 mm. In this work, two types of specimens were adopted for uniaxial tensile testing, flat specimen for static load test and cylindrical specimen for fatigue test, as shown in Figure 3-1(b) and 3-1(d). The selection of cylindrical specimens was primarily to avoid crack initiation from the corners of the flat specimen during high cycle fatigue testing. The flat specimens were adopted to investigate the mechanical constraint as well as the plastic flow characteristics of the 304 stainless steel brazed joints. The preparation of cylindrical specimens are further details in Section 4. Five specimens were tested per sample condition to achieve statistically significant results.

Chapter 4. Mechanical properties and influence of interface roughness

4.1 Introduction

In this chapter, influence of the interface roughness (surface roughness of the stainless steel) on the mechanical properties of Type 304 stainless steel brazed joints is presented. Firstly, the procedure of creating different interface roughness conditions is detailed in Section 4.2. The characterisation of the pre-defined interface roughness of the stainless steel is then reported in Section 4.3, which is followed by results of fracture and fatigue life of the brazed joints as a function of the interface roughness levels. Furthermore, the fracture surfaces of failed specimens were examined, and details are reported. Brazed joints are susceptible to the formation of planar defects, which act as stress raisers and can reduce the mechanical strength remarkably [89]. Coarser roughness at the joint interface may introduce a larger number of defects (i.e. number of voids) because of the reduced wetting behaviour [18], this can be seen from the work conducted by Suezawa [17]. Thus, the influence of interface roughness is discussed in Section 4.4, alongside with the correlation between defect size and fatigue life of the brazed joints.

4.2 Interface roughness conditions and design of experiments

Prior to brazing, the bonding surfaces of the stainless steel samples were prepared using P-grade SiC papers to obtain different interface roughness conditions: P80, P180, P240, P400, P800, P1200 and OPS. For the OPS surface preparation, the stainless steel was firstly ground down to P1200, followed by mechanical polishing using 9 µm, 3 µm and 1 µm diamond suspensions and finally polished by OPS for approx. 5 mins. This helped to provide an ultra-fine surface finish (i.e. deformation-free surface), as stated elsewhere [90]. Sample batch ID 1 to 7 denotes each interface roughness condition, as presented in Table 4-1. For example, batch 3 indicates brazed joints for which the joint interface was prepared with P240. The interface roughness, R_a, is defined as the average roughness of both the microscopic peaks and valleys for a specific joint interface condition. White light interferometry was used for measurement of the pre-define interface roughness.

Table: 4-1 Summary of specimen batch ID, the corresponding interface roughness and parameters for fatigue testing

Batch ID	1	2	3	4	5	6	7	8
Interface roughness	P80	P180	P240	P400	P800	P1200	OPS	steel
Fatigue test parameters	σ_a = 135 MPa (σ_{max} = 300 MPa and σ_{min} = 30 MPa) σ_a = 180 MPa (σ_{max} = 400 MPa and σ_{min} = 40 MPa) R_{ratio} = 0.1, 20 Hz							

HCF tests were conducted using a constant stress amplitude sinusoidal waveform. The cyclic stress ratio was set to R_{ratio} = 0.1 and the frequency was 20 Hz. HCF lives of the brazed joints were assessed by using two stress amplitudes, σ_a = 135 MPa and σ_a = 180 MPa, Table 4-1. The maximum fatigue stress level was selected as 60% and 80% of the average fracture strength of tensile test specimens. This led to the fatigue life being in the range of 10^4 to 10^6 cycles. Five brazed joints were fatigue tested per interface roughness condition, this ranged from P80 to OPS at both stress amplitudes, batch 1 to 7, Table 4-1. In addition, three Type 304 stainless steel specimens (batch 8) were tested at σ_a = 180 MPa to enable a direct comparison of the fatigue properties between the brazed joint and the base metal. The Type 304 specimens were subjected to the same heating and cooling cycle in Figure 3-2 as applied to the brazed joint specimen. To mitigate the effect of machining [91], surface within the gauge section of each fatigue test specimen was ground by SiC paper up to P2500 prior to HCF fatigue tests, giving a R_a value of 0.05 µm, as indicated in Figure 3-1(d).

4.3 Experiment results

4.3.1 Interface roughness and fracture strength

The interface roughness R_a values of specimens that had been processed with different surface preparation conditions are shown in Figure 4-1(a). As can be seen, the roughness values R_a decreased rapidly from P80 (R_a = 0.963 µm) to P400 (R_a = 0.189 µm), whereas little difference between P400, P800 and P1200 were found. The surface polished down to OPS level had the minimum R_a of ~0.005 µm, Figure 4-1(a). In addition, it is evident that a coarser surface preparation led to a relatively large standard deviation (STDEV), whereas a finer

surface preparation led to a much smaller STDEV, Figure 4-1(a). The insets in Figure 4-1(a) illustrate SEM images of the roughness conditions of the coarsest (P80) and finest (OPS) specimens. Grinding marks were readily visible on the surface prepared by P80, whereas the surface prepared down to OPS showed no traceable marks and grain structures can be readily seen.

The tensile testing results of brazed joints from batch 1 (P80) to 7 (OPS) are given in Figure 4-1(b). The fracture strength of brazed joints with their interfaces been prepared from P80 to OPS are 508.5 ± 26.2, 507.0 ± 7.1 (P180), 508.5 ± 14.8 (P240), 518.5 ± 40.3 (P400), 520.0 ± 14.1 (P800), 515.0 ± 4.2 (P1200) and 503.5 ± 12.0 MPa, respectively. No significant difference in fracture strengths can be seen for the brazed joint prepared with different interface roughness conditions, which indicates that joint interface roughness did not affect the fracture strength of the brazed joints. It was also found that all the brazed specimens failed entirely within the joint region.

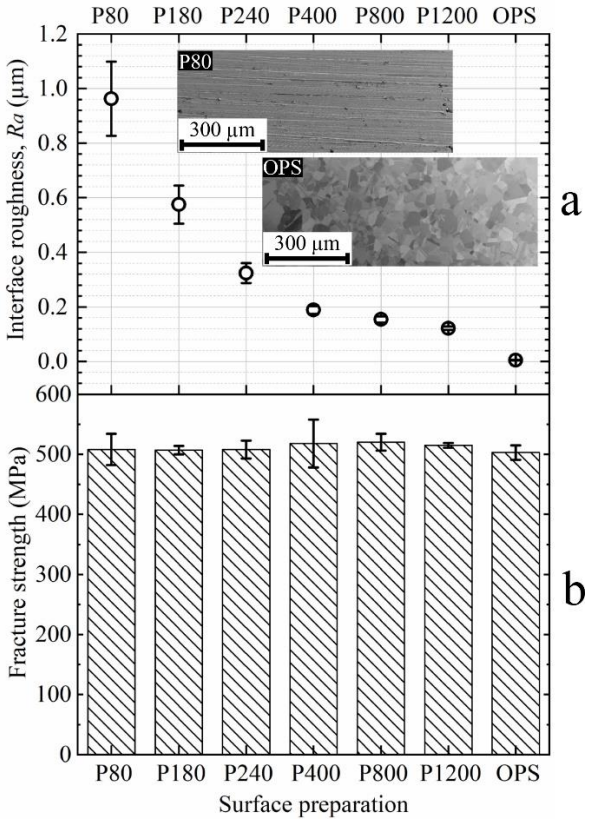

Figure 4-1: (a) Interface roughness condition of the stainless steel base metal prepared by using various methods; (b) the brazed joint fracture strength as a function of the various roughness conditions

4.3.2 High cycle fatigue life

Five specimens per sample condition were tested to assess the average HCF life of brazed joints prepared with different interface roughness conditions. The brazed joints can be categorised into defect-free and defect-bearing groups according to the post-test SEM fractography. The HCF fatigue test results at the higher stress amplitude (σ_a = 180 MPa) are shown in Figure 4-2(a) to reveal the influence of interface roughness as well as the presence of defects. For defect-free joints, it is evident that the joint interface roughness had negligible influence on the fatigue life. The average fatigue life of the defect-free brazed joints was about 8×10^4 cycles, Figure 4-2(a). In contrast, the defect-bearing specimens had lower fatigue life when compared to the defect-free ones, ranging from 1×10^4 to 5×10^4 cycles. In addition, the defect-bearing brazed joints tended to have a large scatter in the measured fatigue life; this particularly applied to interface roughness condition of P240 and OPS.

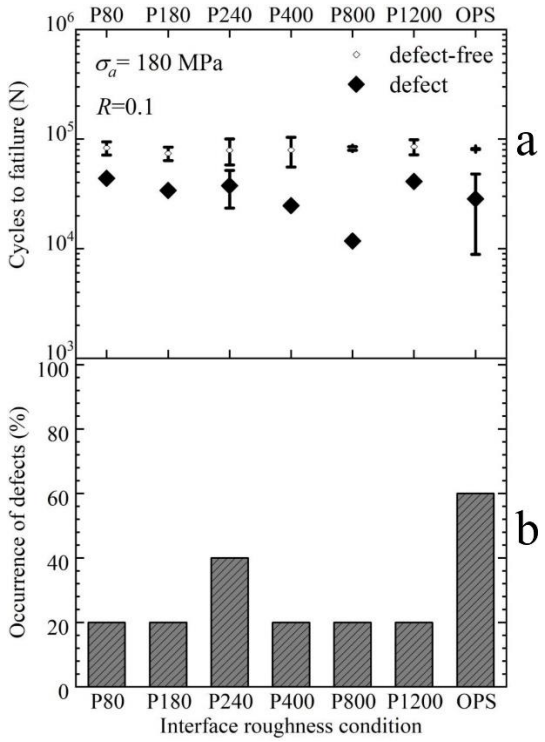

Figure 4-2: (a) HCF life of defect-free and defect-bearing brazed joints with interface roughness conditions ranging from P80 to OPS; (b) the occurrence of defects as a function of different interface roughness conditions

Figure 4-2(b) shows the occurrence of defects in specimens with various interface roughness conditions. The occurrence was calculated according to the proportion of the defect-

bearing specimens within the five specimens per interface roughness condition. As shown in Figure 4-2(b), the occurrence of defects was 20% for P80, P180, P400, P800, and P1200 prepared joints. The brazed joints that had been prepared by P240 exhibited higher defect occurrence of 40%. For brazed joints prepared by OPS, the occurrence of defects was significantly higher than the other interface conditions. This observation could be attributed to limited wetting, which was reported in wetting behaviours of AgCu/Cu systems [92]. In summary, interface roughness of OPS led to an increased likelihood to generate joint defects during brazing, hence being responsible for the relatively large scatter in the fatigue life, Figure 4-2(a).

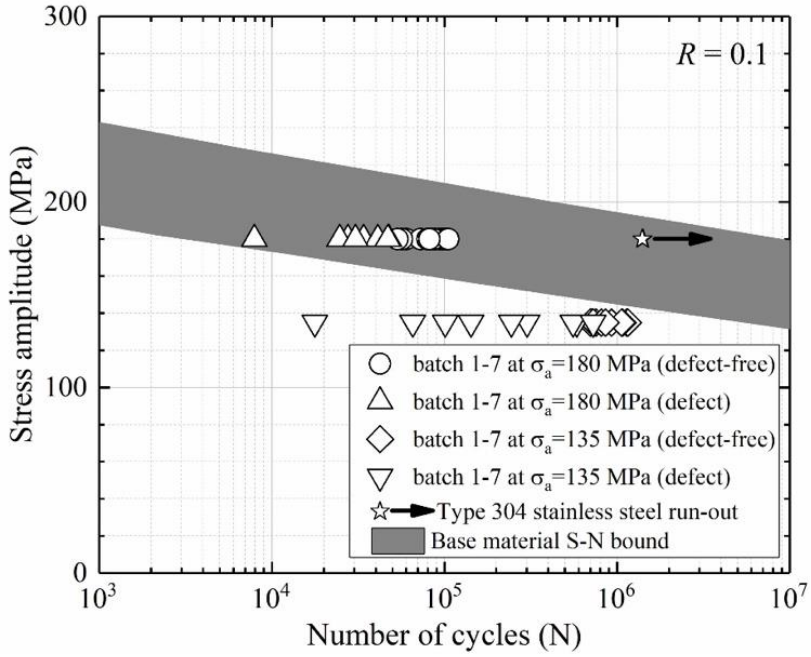

Figure 4-3: HCF life of specimens (batch 1-7) tested at two stress amplitudes, together with the base metal (batch 8) and the corresponding S-N data band from [3]

Figure 4-3 presents the HCF fatigue life of sample batch 1 to 7 at two stress amplitudes (σ_a = 135 MPa & σ_a = 180 MPa), for both the defect-free and defect-bearing specimens. As shown in Figure 4-3, the maximum fatigue life of brazed joints subjected to σ_a = 135 MPa approached 10^6 cycles, whereas the fatigue tests conducted at σ_a = 180 MPa failed within 10^5 cycles. In addition, defect-bearing specimens always had a lower fatigue life when compared to the defect-free counterparts. This applied to both the higher stress amplitude of σ_a = 180 MPa and the lower stress amplitude of σ_a = 135 MPa fatigue tests, Figure 4-3. Furthermore, the defect-free specimens exhibited less data scatter in the HCF fatigue life when compared to

the defect-bearing ones. The grey band in Figure 4-3 is the S-N data bounds of Type 304 stainless steels providing a comparison to the brazed joint specimens. Three base metal fatigue specimens made from the same Type 304 stainless steels were tested at the stress amplitude of σ_a = 180 MPa; all the three base metal specimens did not fail after 3×10^6 fatigue cycles, thus fatigue run-out was indicated in Figure 4-3. This suggests that brazed joints tended to have a lower HCF life when compared to the base metal.

4.3.3 Fractography

After the completion of fatigue tests, it was visually observed that all the brazed specimens failed within the joint region. Since the presence of joint defects was found to dominate the fatigue life of the brazed joints, SEM fractography examination was performed to further understand the joint failure mechanism. Figure 4-4 shows two typical types of fracture surfaces that were observed for all the brazed joint specimens; fatigue cracks initiated either from the specimen surface, see Figure 4-4(a), or from the joint defect, see Figure 4-4(b). SEM images of both fatigue crack initiation regions at higher magnifications are given in Figure 4-4(c) and Figure 4-4(d), respectively. For the defect-free brazed joint specimens, fatigue cracks were exclusively found to initiate from the specimen surface.

Also shown in Figure 4-4(a) and Figure 4-4(b) are the fatigue crack propagation and final fracture zones. There was no difference between the defect-free and defect-bearing specimens in terms of the fatigue crack propagation and final fracture zones, whereas the defect-bearing specimens had a relatively large fatigue crack initiation region when compared to that of the defect-free ones. A large number of dimples were present at the final fracture zones for both the defect-free in Figure 4-4(a) and defect-bearing specimens in Figure 4-4(b). The presence of dimples suggests that these fatigue specimens finally failed by a typical ductile mode that involved void nucleation, growth, and coalescence, because the remaining areas could no longer sustain the maximum stress applied.

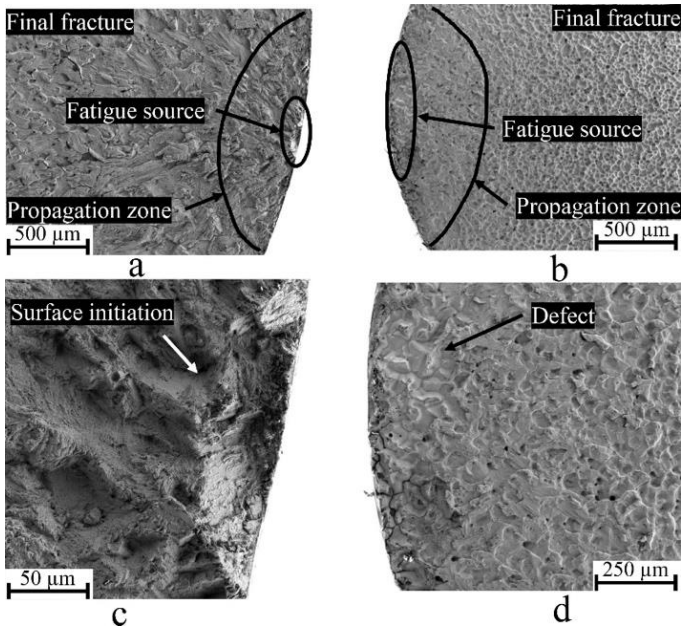

Figure 4-4: Fracture surfaces of (a) defect-free and (b) defect-bearing joints; (c) enlarged view of (a) fatigue crack initiated from the sample surface; (d) enlarged view of (b) fatigue crack initiated from the joint defect. Both samples are from batch 7 (OPS)

Figure 4-5 shows the defect region within the fatigue crack initiation zone of the same sample (batch 7) at a higher magnification, together with the EDX area mapping. The relatively smooth regions in Figure 4-5(a) were considered as the joint defect, likely to be an incomplete fusion type [93]. Intermetallic phases with different sizes can also be seen within these defect regions, Figure 4-5(a). Figure 4-5(b) to Figure 4-5(d) show the corresponding EDX elemental mapping of the selected rectangular box in Figure 4-5(a). It is apparent that the distribution of Cr and Fe, Figure 4-5(b) and Figure 4-5(c), were location dependent and associated with the intermetallic phases. Cu was found to be rich in the whole region but relatively lean in the intermetallic phases, Figure 4-5(d). The average element distribution of the selected EDX region in Figure 4-5(a) is given in Table 4-2; the region of intermetallic phases contained ~94.9% Cu, 2.7% Fe, 0.9% Cr, 1.0% Ni and 0.5% Mn (all in wt.%). Based on the information above, it is evident that elemental diffusion happened during the brazing process, where significant amount of Fe and Cr were found in the joint region. The observed elemental migration would essentially affect the joint mechanical strength. Hence, critical processing parameters including the brazing time and temperature would have a pronounced influence on the joint microstructure, which would eventually alter the joint mechanical strength. The effect of brazing time and temperature is not discussed in this work and will be my future targets.

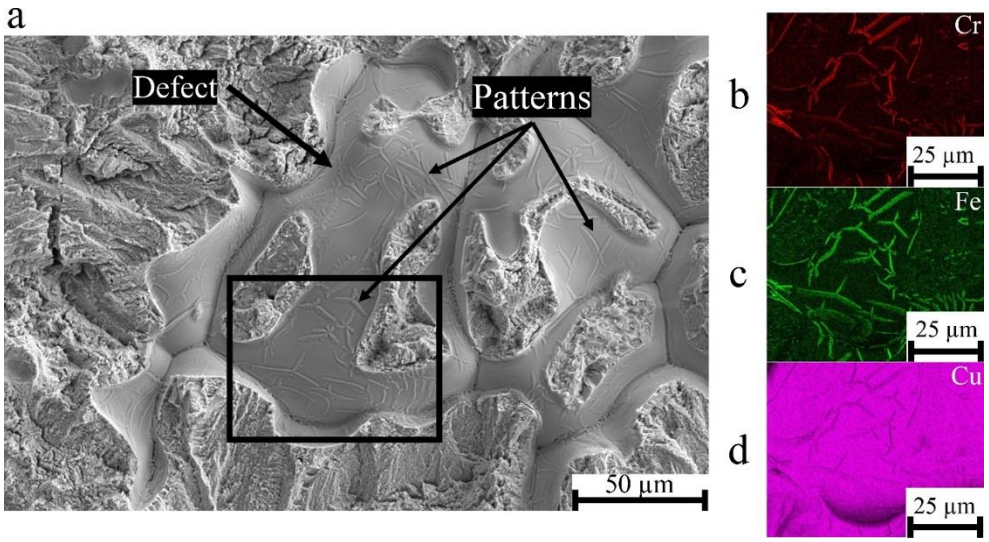

Figure 4-5: (a) Defect region and intermetallic phases within the fatigue crack initiation zone (batch 7); EDX elemental mapping of (b) chromium Cr; (c) iron Fe and (d) copper Cu of the selected rectangular region in (a)

Table 4-2: SEM-EDX data obtained by area mapping at the boxed regions in Figure 4-5(a)

SEM-EDX area mapping	Composition (wt.%)				
	Cu	Fe	Cr	Ni	Mn
SEM-EDX map in Figure 4-5(a)	94.90	2.70	0.90	1.00	0.50

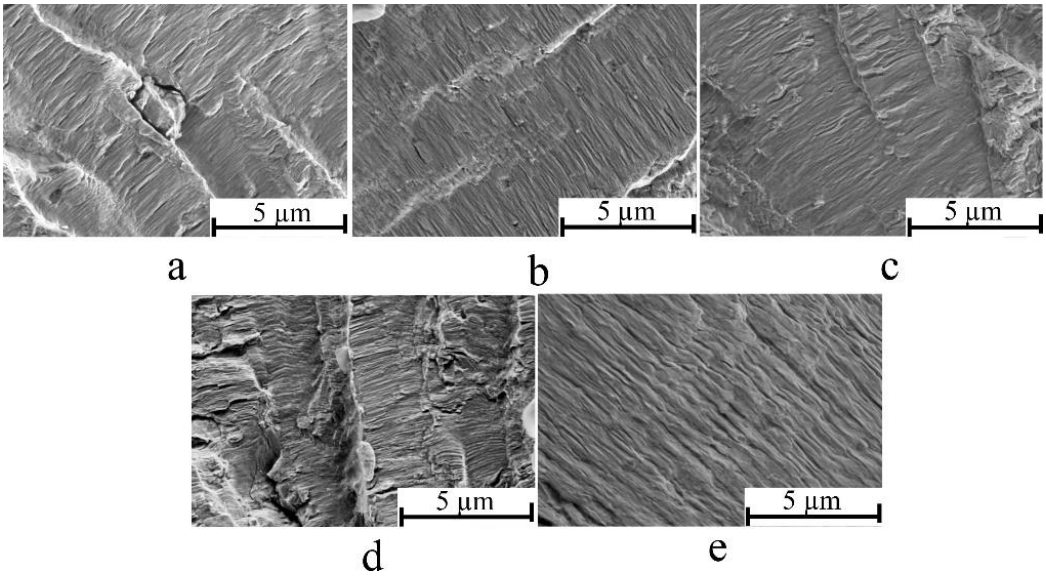

Figure 4-6: Fatigue striation spacings at the early-stage fatigue crack propagation regions of defect-bearing samples with an initial defect area of (a) A = 0.03 mm^2, batch 7A; (b) A = 0.05 mm^2, batch 6A; (c) A = 0.17 mm^2, batch 3A; (d) A = 0.60 mm^2, batch 7B; and (e) A = 1.47 mm^2, batch 6B. Batch ID A & B represents two individual specimens that have the same interface roughness conditions

Figure 4-6 shows the typical fatigue striations for the defect-bearing specimens with various defect areas. Five specimens with distinctive initial fatigue striation spacings were selected and illustrated in an ascending order in Figure 4-6. Figure 4-6(a) shows the minimum fatigue striation spacing, whereas the maximum fatigue striation spacing is shown in Figure 4-6(e); intermediate fatigue striation spacings are presented in Figure 4-6(b) to Figure 4-6(d). The fatigue striations within the early-stage of fatigue crack propagation, i.e. close to the fatigue crack initiation region, were measured to provide an indication of the initial fatigue crack growth rate. The specimens with the smallest defect area of A = 0.03 mm^2 (batch 7A) had a corresponding initial fatigue striation spacing of 0.09 ± 0.02 µm, Figure 4-6(a). Similarly, the initial fatigue striation spacing for the specimen with the largest defect area A = 1.47 mm^2 (batch 6B) was measured to be 0.54 ± 0.05 µm, Figure 4-6(e). The fatigue striation spacing values and the corresponding defect areas are summarised in Table 4-3. It is evident that the initial fatigue striation spacings were positively dependent on the magnitude of the defect areas. For the defect-bearing brazed joints, a larger joint defect led to a higher initial fatigue striation spacing, i.e., a higher initial fatigue crack growth rate.

Table 4-3: Typical joint defect areas and corresponding initial fatigue striation spacings measured from fractography of fatigue test samples (σ_a = 180 MPa). Also shown in this table are the calculated stress intensity factor range as a function of defect area and applied stress ranges. Batch ID A & B represents two individual specimens that have the same interface roughness conditions. ΔK was derived by adopting Eq. (4-2).

Batch ID	7A	6A	3A	7B	6B
Defect area A (mm^2)	0.03	0.05	0.17	0.60	1.47
Initial striation spacing (μm)	0.09±0.02	0.12±0.02	0.19±0.02	0.26±0.01	0.54±0.05
SIF range ΔK (MPa√m)	5.50	6.17	8.44	11.56	14.43

4.4 Discussion

4.4.1 Failure mode for defect-free and defect-containing specimens

Suezawa [94] concluded that the strength of brazed joints can be altered by introducing various joint interface roughness conditions. This is because different interface roughness conditions would essentially provide distinct bonding areas, i.e. relatively rough joint interfaces should lead to stronger brazed joints. Figure 4-7 shows the longitudinal view of fractured specimens (batch 1, 2 and 7, Table 4-1) after HCF tests. Residual filler metals were exclusively found on the fracture surfaces of all the three fatigue specimens that had been prepared to P80, P180 and OPS interface roughness conditions, respectively. However, no visible separations or cracks could be revealed at the copper/stainless steel interface, Figure 4-7. This indicates that both the fatigue crack initiation and propagation occurred entirely within the filler metal region. The prepared joint interface roughness might have altered the strength of the copper/stainless steel interface, but surely did not affect the filler metal itself. Therefore, brazed joint interface roughness conditions had little effect on the fatigue life of defect-free joints.

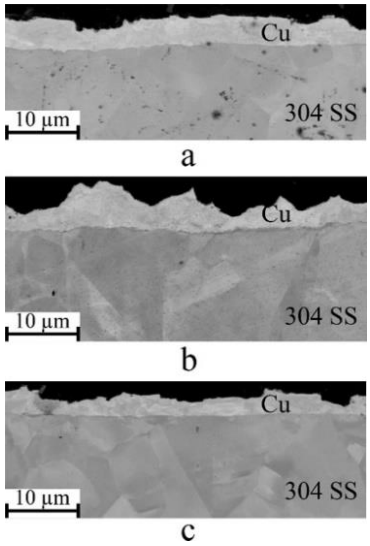

Figure 4-7: Longitudinal sections of the fatigue fractured samples, (a) from batch 1 (P80), (b) from batch 2 (P180) and (c) from batch 7 (OPS)

4.4.2 Influence of defect size on fatigue life

According to Figure 4-4(b), fatigue cracks always initiated from the defect regions for the defect-bearing brazed joints. Defects within the brazed joints occupied a small fraction of the overall joint. For example, Figure 4-8 shows the fracture surface of a specimen from batch 2 (P180 prepared). The area fraction of the final fracture zone was about 85% of the overall designated joint region, whereas the defect fraction was only about 0.2%. If we treat the defect as a pre-existing crack, the crack could grow gradually under the fatigue loading cycles leading to the final fracture.

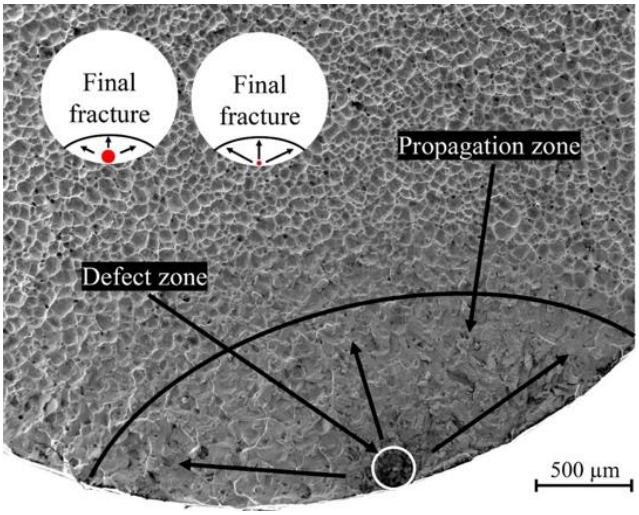

Figure 4-8: Fracture surface of a specimen from batch 2 (P180) showing the defect, fatigue crack propagation and final fracture zones; the insets illustrate fatigue samples where cracks initiated from either a large or a small defect

The insets within Figure 4-8 represent two fatigue specimens where cracks initiated from defects of different sizes. If we assume the area fractions of the final fracture zones are the same for both cases, then the number of cycles needed for the fatigue crack propagation should be different, i.e. the propagation distances for both cases should be different. The fatigue crack propagation distance for the specimen with a larger initial defect would be shorter than that for the specimen with a smaller defect. This fatigue crack propagation distance is indicated in Figure 4-8. Now the only unknown variable is the fatigue crack growth rate. The classic Paris law [95], Eq. (1) is therefore applied here to assist in understanding the initial fatigue crack growth rate in a qualitative way,

$$\frac{da}{dN} = C\left(\Delta K\right)^{m} \tag{4-1}$$

where the coefficient C and exponent m are the material constants, da/dN is the fatigue crack growth rate. It is clear that the initial fatigue crack growth rate for the defect-bearing joints is dependent on the stress intensity factor (SIF) range ΔK, which can be calculated according to the Murakami equation [96],

$$\Delta K = C_2 \times \Delta\sigma \times \sqrt{\pi \times \sqrt{A}} \tag{4-2}$$

where A is the projected defect area on a plane perpendicular to the maximum principal stress, and $\Delta\sigma$ is the applied cyclic stress range. According to literature, C_2 is 0.65 for surface defects [96]. The defects observed within this study were either surface or sub-surface defects, therefore C_2 of 0.65 is considered here. Hence, at the initial stage of the fatigue crack propagation, the fatigue crack growth rate can be expressed:

$$\frac{da}{dN} = C \times \left(C_2 \times \Delta\sigma \times \sqrt{\pi \times \sqrt{A}} \right)^m \tag{4-3}$$

where C, C_2, m, $\Delta\sigma$ and π are all constants, thus the initial fatigue crack growth rate can be simplified as a function of the initial defect area A. According to literature, in the linear elastic fracture mechanics (LEFM) regime, the exponent m is in the range of 3 to 5 for steels [97] and 2 to 4 for pure copper [98]. However, the initial crack size (Figure 4-8) of about 0.2 mm should be considered as a short crack. Consequently, use of the Paris law is inappropriate. Nevertheless, it is convenient to plot short crack growth rate against ΔK as the presentation of the long crack data. The measured exponent m in Eq. (4-3) is greater for short cracks than long cracks under the same ΔK. From literature, m is higher for short crack but in the same magnitude as long cracks [99–101]. Therefore, it is reasonable using the Paris law for a qualitative interpretation. As a consequence, a higher initial fatigue crack growth rate would be expected for a specimen with a larger defect. Since the fatigue propagation distance is considerably short, a specimen with a larger defect would have a shorter fatigue life.

The influences of brazed joint defects on the corresponding fatigue life are now considered semi-quantitatively. The actual relationship between the initial joint defect area and the corresponding fatigue life for all the HCF tested specimens at σ_a = 180 MPa is shown in Figure 4-9. The triangular symbols represent the defect-bearing brazed joints, whereas the circular symbols represent defect-free ones. It can be seen that the defect-bearing joints had much shorter fatigue life when compared to the defect-free ones. Also, the fatigue life of the defect-bearing joints dropped rapidly with the increase of defect areas. For example, the maximum defect area was measured to be ~1.47 mm^2, whereas the corresponding fatigue life was below 10^3 cycles, Figure 4-9. When the defect area decreased, the fatigue life increased and approached that of the defect-free ones. For instance, the defect-bearing specimens had fatigue life of ~4.8×10^4 cycles when the defects were sufficiently small, typically below 0.1 mm^2 in terms of the projection area. This value was relatively close to the lower limit of fatigue life of the defect-free specimens of ~5.2×10^4 cycles. The secondary vertical axis (Figure 4-9) shows

the calculated defect area fraction over the overall joint. This might be of a practical interest. For the defect-bearing specimens, the relationship between defect areas and corresponding fatigue life was also plotted on logarithmic scale as illustrated in the left inset in Figure 4-9. Linear fitting was applied to reveal how the fatigue life decreased as the defect increased; the slope of the linear fitting was found to be around 1.52 ± 0.25.

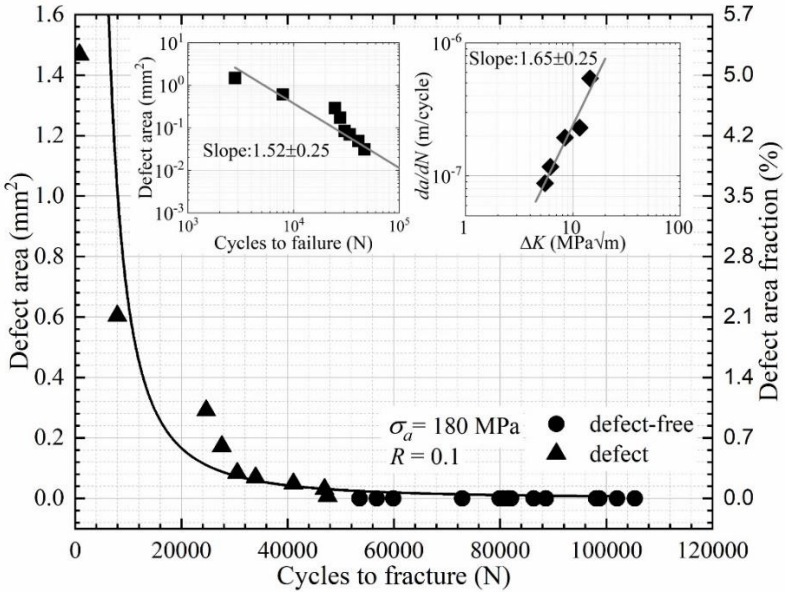

Figure 4-9: Relationship between the joint defect area and the corresponding fatigue life for all the fatigue tests performed at σ_a = 180 MPa; the insets show the relationship between joint defect area and fatigue life, and the initial fatigue crack growth rate as a function of ΔK on logarithmic scales

Fatigue crack growth rate is defined as crack extension per load cycle, *da/dN*, as shown in Eq. 4-1. Fatigue striation spacings measured near the joint defect can therefore be considered as an indication of the initial fatigue crack growth rate, Figure 4-6. Hence, the initial fatigue striation spacing of a specimen with a larger defect should be much greater than that with a smaller defect, owing to the larger defect area and hence larger stress intensity factor range ΔK. This was also revealed by the measurement of fatigue striation spacings on fracture surfaces of the defect-bearing specimens, Table 4-3. The corresponding ΔK values were also calculated and listed in Table 4-3 in an ascending order. In total, five ΔK values were considered here and it was found that ΔK increased from 5.50 MPa√m (batch 7A) to 14.43 MPa√m (batch 6B) when the corresponding initial defect area increased from 0.03 mm^2 to 1.47 mm^2, leading to an increase in the initial fatigue striation spacing from 0.09 ± 0.02 μm to 0.54 ± 0.05 μm, Table

4-3. The initial fatigue crack growth rate (*da/dN*) of the brazed specimens with various initial defect areas were also plotted against the corresponding SIF range (ΔK) on logarithmic scale, as shown in the right inset in Figure 4-9. The slope of the linear fitting, providing the Paris law exponent *m* as shown in Eq. 4-3, was found to be 1.65 ± 0.25, which agrees well with the lower bound of literature value of 2 to 4 for pure copper [98]. This suggests that a large joint defect, which leads to a higher SIF range ΔK, will result in a higher fatigue crack growth rate, hence shorten the fatigue life exponentially.

4.5 Conclusions

This chapter examined the influences of interface roughness and defects on the fracture and high cycle fatigue life of Type 304 stainless steel brazed joints. Based on the results obtained the following conclusions can be made:

1. The brazed joint showed higher tensile strength and HCF life when compared to pure copper.
2. No significant difference in fracture strengths can be seen for the brazed joint prepared with different interface roughness conditions from P80 to OPS. This indicates that joint interface roughness did not affect the consequent tensile strength of the brazed joints on the ground that all the brazed specimens failed entirely within the joint region.
3. The joint interface roughness had negligible influence on the fatigue life of defect-free brazed joints. This was attributed to the fact that both the fatigue crack initiation and propagation happened entirely within the joint region.
4. For the defect-bearing brazed joints, larger defect led to a higher fatigue crack growth rate at the initial stage. Qualitatively, the fatigue cycles to failure was found to decrease with the increase of defect area (size).

Although the experimental result has suggested that the interface roughness had limited influence on the mechanical strength of the brazed joints, the fracture strength as well as the fatigue life, however, were significantly higher as compared to the filler metal, i.e. pure copper. Thus, the brazed joint showed enhanced mechanical strength. This finding leads to the following chapter to investigate the microstructural contribution towards the overall strength of the brazed joint.

Chapter 5. Microstructure and theoretical joint strength

5.1 Introduction

In this chapter, microstructural characteristics of the Type 304 stainless steel brazed joints are reported. This includes texture and grain size distribution of the joint region (Section 5.2), together with precipitation morphology in Section 5.3. In addition, the strength heterogeneity of the joint region is reported in Section 5.4. Elemental analysis on the basis of SEM-EDX is also reported to reflect potential elemental segregation and chemical compositions of the joint region and secondary phases in Section 5.5. In Section 5.6, TEM imaging of the precipitates is reported, alongside with the crystal structure of the precipitates and the joint region obtained from TEM-SAED. At last, precipitation formation as well as the theoretical joint strength are discussed in Section 5.7.

5.2 Microstructure of the brazed joint

The overall microstructure of Type 304 stainless steel brazed joint is shown in Figure 5-1(a), where the brighter region was the copper-based brazed joint and darker region was the stainless steel base metal. No cracks or porosities were observed at the base-filler metal interface, implying good wetting behaviour. The thickness of the brazed joint was ~110 μm, which agrees well with the thickness of 125 μm for the inserted copper foil. A representative EBSD orientation map for the brazed joint region is shown in Figure 5-1(b), revealing equiaxed grain structures. The grains within the joint region were randomly orientated with intensities less than 4 times the perfect isotropic case for the {100} pole figure, Figure 5-1(c), suggesting a weak texture. The grain size is shown in Figure 5-1(d) where the size-distribution histogram and the Weibull fit curve are presented. The average grain size (equivalent diameter) was determined as 57.2 ± 2.3 μm by examining over 500 grains. Calculation of the average grain size was performed by using Chanel 5 software package, the determined value was also verified by comparing with that determined via linear intersect method. Joint microstructures for those that had been prepared to various interface roughness values were found to be identical, hence only one sample is shown here as an exemplar.

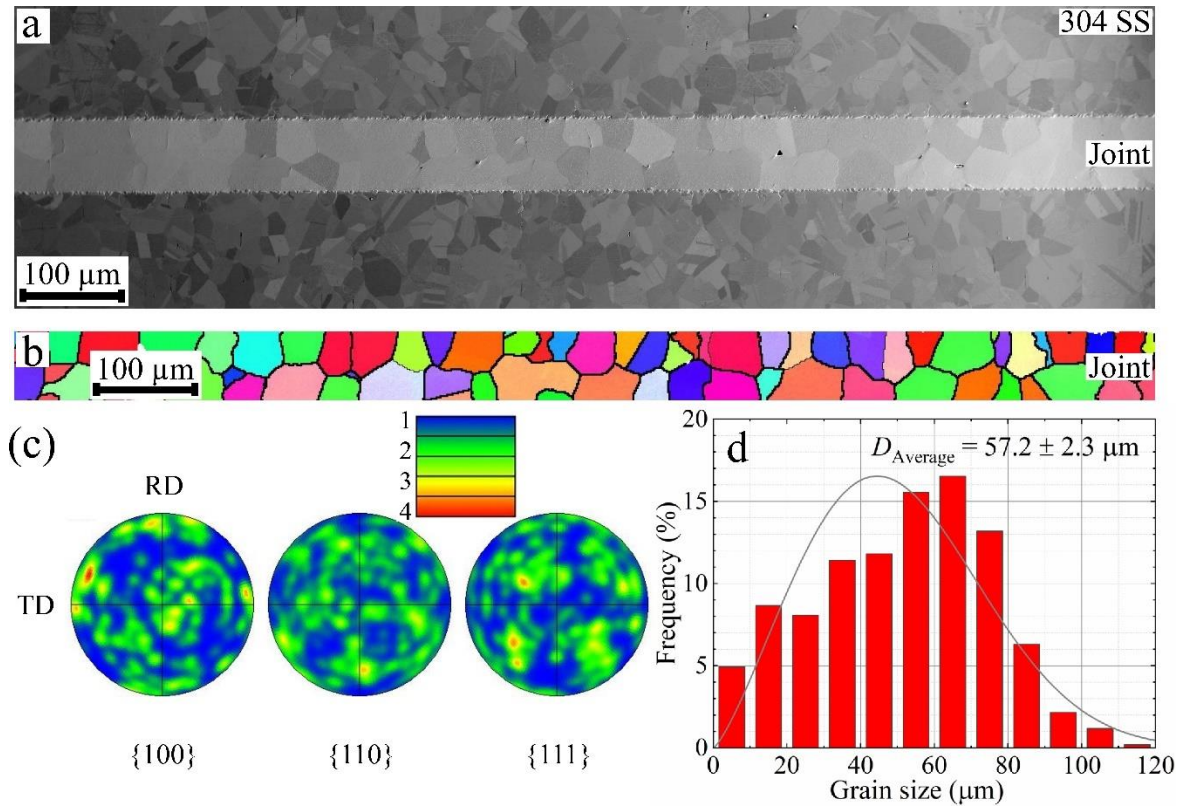

Figure 5-1: (a) SEM image of the as-brazed joint microstructure; (b) corresponding EBSD orientation map, showing near equiaxed grains within the joint region; (c) pole figures indicating a relatively weak texture; (d) grain size-distribution (equivalent diameter)

5.3 Precipitation distribution

Figure 5-2 shows detailed joint microstructure at the as-brazed condition where individual grains, grain boundaries as well as the base-filler metal interface (indicated by white arrows) can be seen. The presence of star-shaped precipitates within the joint region were revealed at higher magnification and shown in the inset in Figure 5-2(a). It is also confirmed that these precipitates existed in each individual grain throughout the brazed joint. In addition, both the size and number density of the precipitates decreased in the vicinity of grain boundaries, Figure 5-2(b), which is consistent with a precipitate-free zone theory [102]. The size of the precipitates was similar at all positions within grain interiors. Their average size and volume fraction were determined to be 117 ± 25 nm (radius) and 2.3%, respectively. Ghovanlou et al. [9] conducted brazing of low carbon steels using copper where iron-rich precipitates with a similar morphology were found. Under the thermodynamic equilibrium condition, copper can dissolve up to 3.5 wt.% iron at the brazing temperature of 1120°C, whereas the solubility of iron in

copper at room temperature is negligible, Figure 5-2(c). Therefore, these star-shaped features are likely to be iron-rich copper precipitates.

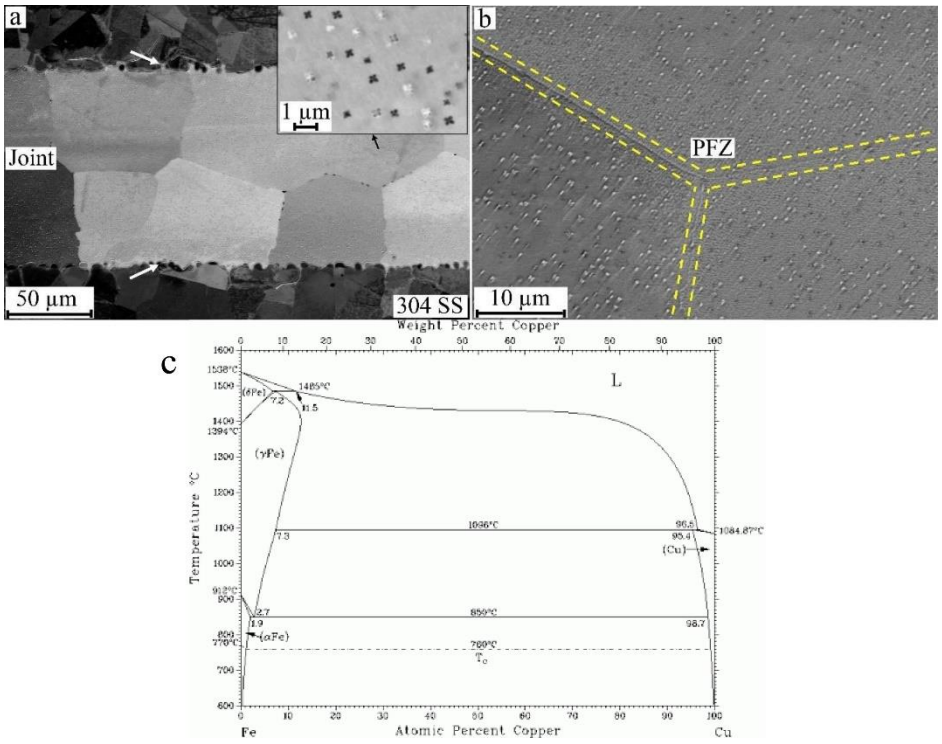

Figure 5-2: (a) Brazed joint microstructure showing individual grains as well as grain boundaries; the inset illustrates the petal-shaped precipitates within individual grains; (b) precipitate-free zone (PFZ) in the vicinity of grain boundaries; (c) Cu-Fe equilibrium phase diagram

5.4 Hardness of the joint region

Nanoindentation was performed to evaluate the strength heterogeneity across the brazed joint. Figure 5-3(a) shows locations of the 10 indents in the base stainless steel (5 indents on each side), 10 within the brazed joint but close to the base-filler metal interface, and the rest being distributed within the joint. Each row of the indents covered the entire joint region with the first and last being in the base metal. The average indent size in the base stainless steel was 2.0 µm, which was smaller than those within the brazed joint of 2.5 µm, Figure 5-3(a). This difference in indent size corresponds well with the determined hardness, i.e. the base stainless steel had a hardness value well above 2.5 GPa while those in the brazed joint were below 1.5 GPa, Figure 5-3(b). Note any indent positioned close to the interface or a free surface (e.g. less than a distance of 3 times the indent diameter) is judged inappropriate according to the best

practice of performing quantitative and reproducible indentation measurement [4]. As a result, no attempt was made to capture the refined hardness profile across the base-filler metal interface.

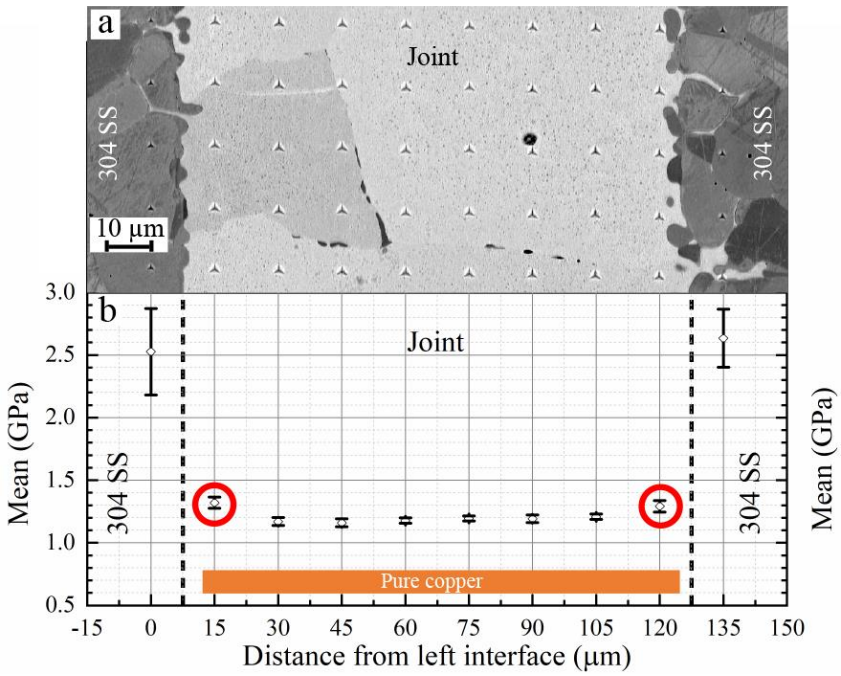

Figure 5-3: (a) The array of Berkovich indents across the brazed joints; (b) hardness derived from the nanoindentation measurements with the colour band representing hardness values for pure copper [4]

The average hardness of the copper matrix in the central region of the brazed joint was 1.1 GPa, Figure 5-3(b), and this was significantly higher than those being reported for pure copper of 0.5 to 0.7 GPa [4,103]. Taking indentation size effect into consideration, the obtained hardness of 1.1 GPa was still higher than that of single-crystal copper (0.7 GPa for a {110} crystallographic plane) obtained with a similar Berkovich indent size [87]. Hall-Petch effect can also affect the indentation hardness measurement, but it required an average grain size of 1.2 µm for pure copper to achieve such a high hardness value of 1.1 GPa [4,87]. This is significantly smaller compared to the 57.2 ± 2.3 µm observed in Figure 5-1(d). However, Hal-Petch effect was not likely to cause significant strengthening within the brazed joint as most of the indentations hardly covered any grain boundaries, Figure 5-3. Therefore, the increased hardness was more likely a consequence of elemental migration, i.e., precipitation hardening and solid-solution strengthening. Moreover, regions in the vicinity of the base-filler metal

interface showed a further hardness increase to 1.3 GPa (circled in Figure 5-3(b)). We will discuss this interesting aspect in detail together with the measured GND density in Chapter 6.

5.5 Chemical composition

Figure 5-4(b) to Figure 5-4(f) show the corresponding SEM-EDX elemental mapping of the selected region in Figure 5-4(a). It is apparent that Mn and Ni elements, Figure 5-4(e) and Figure 5-4(f), were evenly distributed through the joint region, whereas the amount of Cr and Fe, Figure 5-4(b) and Figure 5-4(c), were location dependent and with significant concentrations at the star-shaped regions. Thus, star-shaped particles were rich in Cr and Fe while relatively lean in Cu when compared to the Cu matrix, Figure 5-4(d). In addition, EDX point analyses were performed at two typical locations; points 1-4 for the Cu matrix and points 5-8 for the star-shaped particles, Table 5-1. The Cu matrix in Figure 5-4(a) contained ~96.1 wt.% Cu, 1.9 wt.% Fe, 0.3 wt.% Cr, 1.2 wt.% Ni and 0.5 wt.% Mn, while the star-shaped particles contained ~77.3% Cu,16.5% Fe, 3.8% Cr, 1.8% Ni and 0.6% Mn (all in wt.%). These chemical compositions revealed in Figure 5-4(a) were very close to those observed in the selected region in Figure 4-5(a), indicating that the star-shaped particles observed in Figure 5-4(a) might be the imprints (cross-sectional view) of those patterns in Figure 4-5(a).

Table 5-1: SEM-EDX data obtained by point analysis and area mapping at the boxed regions in Figure 5-4(a). Points 1-4 and 5-8 represent the copper matrix and star-shaped particles within Figure 5-4(a), respectively

SEM-EDX point analysis and area mapping	Composition (wt.%)				
	Cu	Fe	Cr	Ni	Mn
SEM-Point 1-4 (copper matrix)	96.10±0.44	1.93±0.47	0.33±0.15	1.17±0.06	0.50±0.10
SEM-Point 5-8 (particles)	77.25±0.52	16.50±0.56	3.80±0.14	1.83±0.05	0.63±0.05
SEM-EDX map in Figure 5-4(a)	93.90	3.70	0.70	1.20	0.50

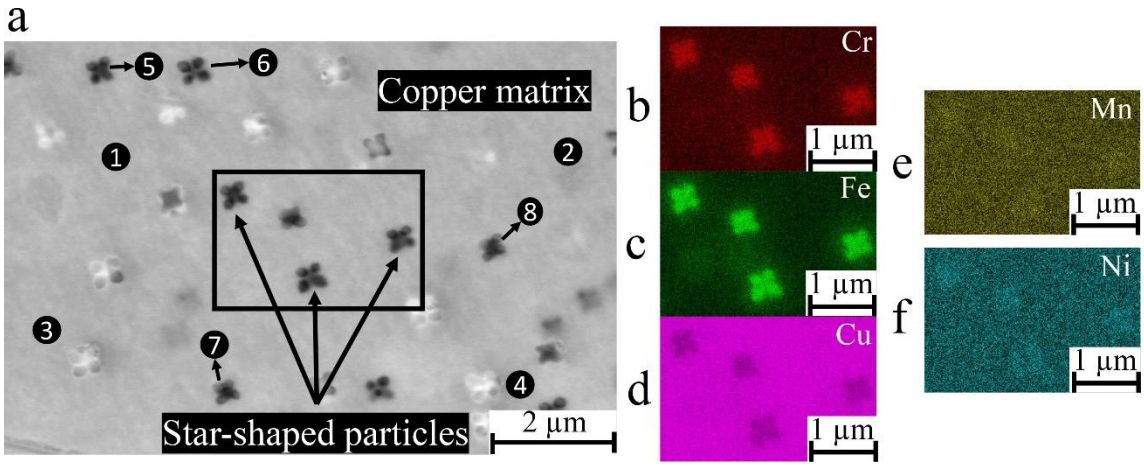

Figure 5-4: (a) Microstructure of Type 304 stainless steel brazed joints with star-shaped intermetallic compound presented; EDX elemental mapping of (b) Cr; (c) Fe; (d) Cu; (e) Mn (e) and (f) Ni of the selected rectangular region in (a)

In addition, Figure 5-5(a) shows two copper-rich grains separated by a grain boundary within the brazed joint region. The grain on the left contained star-shaped (four petals) particles, while the one on the right contained three-petal-shaped particles. In addition, most particles within each individual grain possessed preferred orientations. This indicates that the shapes and orientations of the particles might be dependent on the grain orientation of the copper matrix, i.e., a possible fixed orientation relationship between the particles and copper grains, as illustrated by a schematic diagram in Figure 5-5(b).

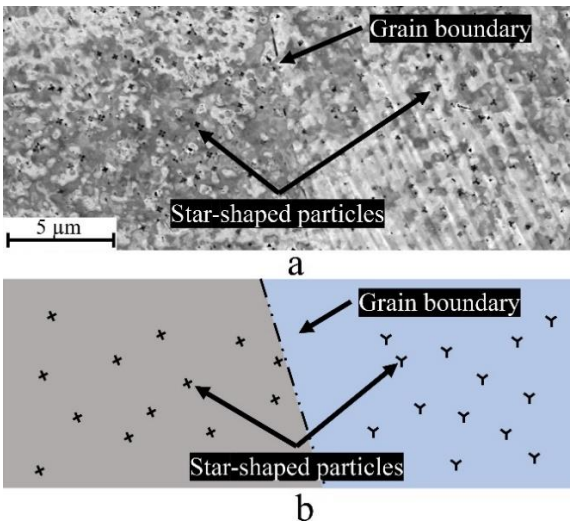

Figure 5-5: (a) Star-shaped particles formed at copper grains with different morphologies and orientations; (b) a schematic diagram showing different particle morphologies presented within two differently oriented grains

5.6 Crystal structure and orientation relationship

A representative TEM bright-field (BF) image of precipitates in the brazed joint is shown in Figure 5-6(a). Based on the SAED patterns ($[01\bar{1}]$ zone axis) for the precipitate in Figure 5-6(b) and the copper matrix in Figure 5-6(c), it is evident that the star-shaped precipitates had the same crystal structure to the copper matrix, i.e. face-centred cubic (fcc). However, the lattice constants of the precipitates and the copper matrix were determined to be 0.361 nm and 0.374 nm, respectively. This suggests a lattice constant misfit, $\delta_{\text{matrix-precipitate}}$, of ~5.0 % between the two.

To further characterise these precipitates, STEM-HAADF imaging was used and the result is shown in Figure 5-7(a). The two insets reveal the atomic arrangements of the copper matrix and the precipitate, Figure 5-7(b) and Figure 5-7(c), respectively. Interplanar spacings of both the (111) and (200) planes were measured, and the results showed that the precipitate had smaller interplanar spacings when compared to the copper matrix. Figure 5-7(d) shows the interfacial region between the precipitate and the copper matrix. The habit planes can be observed in the corresponding FFT pattern in Figure 5-7(e), i.e. $(111)_{\text{matrix}}$ // $(111)_{\text{precipitate}}$, $(11\bar{1})_{\text{matrix}}$ // $(11\bar{1})_{\text{precipitate}}$ and $(200)_{\text{matrix}}$ // $(200)_{\text{precipitate}}$. The morphology of the star-shaped precipitate was claimed to be associated with the balance between the precipitate/matrix interfacial energy and coherent strain energy, with the primary branch growing preferentially along the <111> directions [104,105].

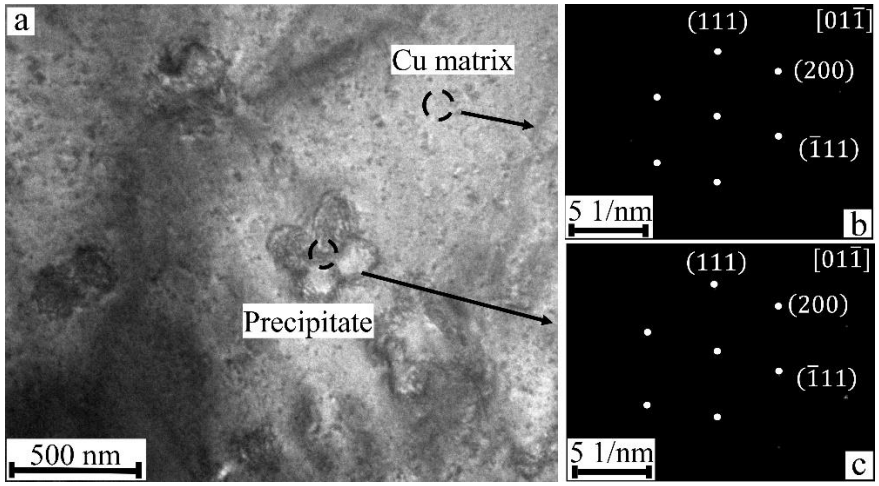

Figure 5-6: (a) Bright-field TEM image along the $[01\bar{1}]$ zone axis; (b) selected area electron diffraction (SAED) pattern of the copper-rich matrix; (c) SAED pattern of the precipitate

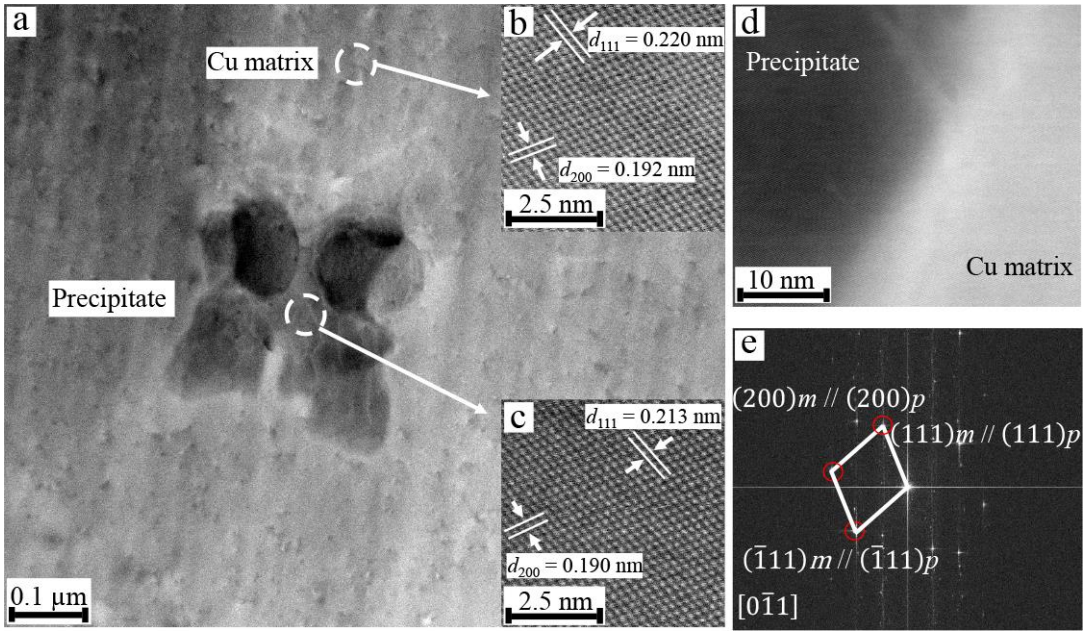

Figure 5-7: (a) HAADF imaging of a precipitate; (b) atomic arrangement of the copper matrix; (c) atomic arrangement of the precipitate; (d) high-resolution TEM image showing the interfacial region between the precipitate and the copper matrix; (e) FFT pattern of the interfacial region in (d), showing the habit planes

5.7 Discussion

5.7.1 Precipitation

Chen et al. [13] performed casting process of copper and copper alloys with additional iron element (<1.5 wt.%). As a consequence, iron-rich precipitates with an average size of 6 nm were created and the copper alloy was found to be strengthened via the precipitation hardening effect. Two distinct morphologies of these iron-rich precipitates were also identified and characterised in [11]: (i) near-spherical-shaped (body-centred-cubic, bcc crystal structure) nanoparticles with size ranges from 2 to 20 nm in diameter and (ii) star-shaped (fcc) nanoparticles with size ranges from 20 to 150 nm. Furthermore, it was reported in [12] that large star-shaped precipitates (bcc) between 250 and 500 nm would be produced if extra iron was added.

In the current work, the average iron content measured within the joint microstructure was 3.70 wt.% according to Figure 5-4(a) and Table 5-1. In addition, the average size (radius) of the observed star-shaped particles was ~117 nm, Figure 5-4(a). Two primary reasons could be responsible for the formation of large sized iron-rich nanoparticles in the present stainless steel

brazed joints. Firstly, the morphology and size of the nanoparticles is strongly affected by the iron content; this is consistent with the previous findings in [12] where star-shaped particles were found for Cu-2.0Fe-0.5Co and Cu-3.0Fe-0.5Co alloys with sizes of ~200 nm and ~300 nm, respectively. It was also claimed by Chen et al. [12] that iron-rich nanoparticles would undergo a spherical-to-star shape transition when iron content was higher than 2.0 wt%. Secondly, the brazing cycle (Figure 3-2) utilised a relatively slow cooling rate of about 130 °C/min, when compared to the cooling rate of 100 °C/s for the copper alloy casting process. The prolonged cooling cycle in brazing could potentially serve as an aging process that led to the coarsening of iron-rich nanoparticles [11].

In brief, the precipitation evolution observed in the present brazed joint can be summarised as follow. At the brazing temperature of 1120 °C, approx. 3.70 wt.% iron migrated from the base metal into liquid copper through high-temperature diffusion, Figure 3-2. At the beginning of cooling, iron started to precipitate out from the liquid copper as spherical nanoparticles. During the continuous and slow cooling, the iron-rich precipitates grew into star-shaped precipitates with a fcc crystal structure. As shown in Figure 5-4(a), the copper filler metal was no longer chemically homogeneous after the brazing process. Foreign elements, such as iron, nickel, manganese and chromium all diffused from the base metal into the joint region as a result of high-temperature diffusion. Both the chromium and iron contents were found to be location dependent; being rich in those star-shaped particles shown in Figure 5-4(b) and Figure 5-4(c). A similar observation of the particles has been reported in [106,107] where fine iron-rich particles were found in copper with the same morphology. Steward et al. [108] also suggested that these particles were iron-rich precipitates mostly being $FeCu_2$ and $FeCu_{18}$, determined by wavelength-dispersive X-ray spectroscopy. According to the SEM-EDX point analysis performed on the star-shaped particles, Figure 5-4(a) and Table 5-1, the iron-rich particles had a similar chemical composition close to that of formula $FeCu_4$ [109]. Similar nanoparticles with an average size of 350 nm were also reported as $FeCu_4$ phase by Shu et al. [110] when performing gradient deposition of copper on stainless steels.

It is worthwhile to note that only iron-rich nanoparticles have been reported to precipitate in copper matrix according to the work performed by Klein et al. [111]. Conversely, a measurable amount of chromium (3.8 wt.%) was also detected at the iron-rich nanoparticles but not at the copper matrix, Table 5-1. According to the Fe-Cu, Cr-Cu binary phase diagrams, copper can dissolve up to 3.5 wt.% iron and 2.0 wt.% chromium at the brazing temperature of 1120 °C. The joint region contained on average ~3.7 wt.% iron and ~0.7 wt.% chromium according to the EDX area mapping, Table 5-1. The amount of iron (3.7 wt.%) that diffused

from the base metal into the joint region agrees well with that in the Fe-Cu phase diagram (3.5 wt.%). However, the amount of chromium (0.7 wt.%) within the joint region was only less than half of the equilibrium value (2.0 wt.%). This could be attributed to the differences in concentrations of iron (~70 wt.%) and chromium (~19 wt.%) in the base metal, Table 3-1. In other words, there was less chromium within the base metal to diffuse into the copper filler metal. Nevertheless, both iron and chromium are almost immiscible in copper at room temperature and Chbihi et al. [112–114] has reported that chromium could precipitate out from copper matrix of Cu–1Cr–0.1Zr (wt.%) with a fcc crystal structure. Therefore, the observed star-shaped particles within Figure 5-4(a) are precipitates being rich in copper, iron and chromium.

5.7.2 Theoretical joint strength

To gain a better understanding of the influence of the observed precipitates (Figure 5-4) on the mechanical strength of the brazed joints. A theoretical evaluation of the joint strength is calculated here, and this will be compared to the experimentally determined value. Strengthening mechanisms in polycrystals can be summarised into four categories: solid-solution strengthening, grain size reduction strengthening, dislocation strengthening, and precipitation hardening [115]. For precipitation hardening, the presence of fine precipitates in metal matrix hinders dislocation motion and results in strengthening. The strengthening effect mainly depends on size, distribution, volume fraction, and strain field associated with the precipitates [116]. Two primary strengthening mechanisms are introduced to describe the interaction between dislocations and precipitates in copper alloys, i.e. dispersion strengthening [117] and coherency strain hardening [118].

Dispersion strengthening assumes that the precipitates do not deform with the matrix. Additional shear stress is therefore necessary to expand a dislocation to by-pass the precipitates [119]. For the homogenously distributed precipitates within the joint region, Figure 5-2(a) and Figure 5-2(b), the strengthening by dislocation-looping can be theoretically calculated using the Orowan equation [120]:

$$\sigma_{Orowan} = \frac{0.84MGb}{2\pi(1-\nu)^{1/2}\lambda}\ln\frac{r}{b} \tag{5-1}$$

where G and b are shear modulus of 45 GPa and Burgers vector of 0.255 nm for copper. M = 3.06 is the Taylor factor for fcc polycrystals [121]. ν = 0.33 is the Poisson's ratio and λ is the interparticle spacing between the precipitates. To simplify the calculation, the precipitates were treated as spheres with average radius r of 117 nm. λ was derived by using $\lambda = r(2\pi/3f)^{0.5}$ [120], where f is the volume fraction of the precipitates (2.3%). The values of r and f were determined from at least five SEM images similar to the one shown in Figure 5-2(a). Consequently, strengthening induced by the dispersed precipitates σ_{Orowan} was calculated as ~30 MPa. To this end, it can be confirmed that the strengthening induced by dislocation-looping mechanism played little role towards the overall strength of the brazed joint. We now consider the potential strengthening effect as a result of coherency strain hardening.

Coherency strain hardening occurs due to lattice mismatch between the precipitates and the matrix [122]. When a dislocation passes through ordered precipitates, it creates antiphase boundary (APB). Consequently, the energy required to create APB opposes the passage of dislocation, which in turn increases the strength of the material. It was also reported that the overall strength would increase as the precipitate size increases [123]. For single crystal Ni-based superalloys, TEM studies have shown that gamma prime precipitates shearing by dislocations are operative up to 800 °C, whereas above 800 °C the plastic flow occurs by dislocation-looping mechanism [124]. It is of interest to comment on the directionality of the interaction force between a dislocation and a coherent precipitate, i.e. attractive or repulsive, as this could determine whether such an effect is positive or negative towards the overall material strengthening. A given dislocation would experience equal numbers of attractive and repulsive forces and the maximum interaction force is identical for both attractive and repulsive particles [125]. The main difference between attractive and repulsive interactions being that for repulsive particles, the maximum force acts before the dislocation reaches the precipitate, while for attractive interactions, the maximum force occurs after the dislocation has passed the particle [125]. This indicates that a dislocation would always experience a repulsive force when interacting with a coherent precipitate, either before or after passing the particle. As a result, dislocation motion in this context means that an additional stress is required for a dislocation to glide through the metal matrix, hence contributing to the material strength.

Based on the high-resolution TEM observations, Figure 5-7(d) and Figure 5-7(e), it is evident that a cube/cube crystallographic relationship existed between the precipitates and the matrix. The lattice constant misfit $\delta_{\text{matrix-precipitate}}$ was estimated as 5.0% by analysing the interplanar spacings of the precipitates for the $[01\bar{1}]$ zone axis of the matrix, Figure 5-6(b) and Figure 5-6(c). The misfit of lattice constant would produce a local strain field surrounding the

precipitates. Although the precipitates (117 ± 25 nm) in this work are much larger than those encountered in conventional precipitation hardened alloys, Sengupta et al. [124] reported that coherency strain hardening could remain effective for precipitates with sizes up to 1.1 μm. The strengthening as a result of coherency strain hardening $\sigma_{\text{Coherency}}$ can be evaluated according to [126]:

$$\sigma_{Coherency} = 0.7MGf^{1/2}\left(\frac{2\delta_{matrix-precipitate}3b^3}{3r^3}\right)^{1/4} \quad (5\text{-}2)$$

where all the symbols have been defined earlier. $\sigma_{\text{Coherency}}$ from the strain field of the precipitate was calculated to be ~60 MPa. However, the precipitation related strengthening mechanism (dislocation-pinning and coherency strain hardening) cannot provide a reasonable explanation to the enhanced fracture stress σ_f (~500 MPa, Figure 4-1) in the copper brazed joint.

Grain size reduction strengthening could also contribute towards the enhanced fracture stress. The Hall-Petch relationship relates the yield stress and polycrystal grain size via an inverse square root of dimension [87]:

$$\sigma_{Hall-Petch} = \sigma_0 + \frac{k}{\sqrt{d}} \quad (5\text{-}3)$$

where k is a constant, σ_0 is the yield strength of single polycrystals and $\sigma_{\text{Hall-Petch}}$ represents the strengthening induced by grain size reduction. d is the mean grain size. To assess the contribution of grain size reduction strengthening, k of 0.1 GPa·√μm [4,127] was applied to give an enhancement of ~10 MPa. Therefore, the grain size reduction strengthening played little role for the brazed joint.

The SAED results in Figure 5-6(b) and Figure 5-6(c) reveals that the lattice constant of the copper matrix (0.374 nm) was larger than that of pure fcc copper (0.361 nm), suggesting a solid-solution effect with lattice distortion due to the presence of solute elements. In this context, STEM-EDX elemental mapping as well as point analysis was conducted and reported here to support in quantifying the solute elements within the copper matrix. STEM-EDX elemental mapping of the precipitates is presented in Figure 5-8(a)-(f). It is evident that manganese, Figure 5-8(f), was homogeneously distributed throughout the joint region, whereas the amounts of chromium, iron and nickel, Figure 5-8(b), (c) and (e), were location dependent and concentrated at the precipitates. Thus, the petal-shaped precipitates were enriched in

chromium, iron and nickel while relatively depleted in copper when compared to the copper matrix, Figure 5-8(d). This finding is consistent with what was observed from SEM-based EDX result, Figure 5-4. Furthermore, STEM-EDX point analysis was performed to obtain a semi-quantitative evaluation of the elemental distribution; the results were based on the average of five measurements. The copper matrix contained 5.9 ± 0.1% Ni, 2.9 ± 0.1% Fe, 1.9 ± 0.1% Mn, 0.6 ± 0.1% Cr and 88.7% Cu (all in wt.% unless otherwise stated), whereas the petal-shaped precipitates contained 16.9 ±3.3% Ni, 39.8 ± 10.8% Fe, 1.9 ± 0.1% Mn, 8.0 ± 1.3% Cr and 33.4% Cu, Table 5-2. Note the STEM-EDX revealed a higher amount of Ni, Fe, Mn, and Cr for the copper matrix as well as the precipitates. This difference was attributed to the different sampling volumes for STEM-EDX and SEM-EDX, that the STEM-EDX was based on a thin foil, whereas SEM-EDX was based on thick metallurgical samples with potential influences from material beneath the surface. The STEM-EDX result is consistent with SEM-EDX in terms of showing significant concentration of Fe, Cr and Ni within the precipitates. In addition, homogeneous distribution of Mn within the joint region was revealed by both STEM-EDX and SEM-EDX, Table 5-1 and Table 5-2.

Table 5-2: STEM-EDX data obtained by point analysis for the copper matrix and star-shaped particles within Figure 5-8(a)

STEM-EDX area mapping	Composition (wt.%)				
	Cu	Fe	Cr	Ni	Mn
Copper matrix	88.7	2.9 ± 0.1	0.6 ± 0.1	5.9 ± 0.1	1.9 ± 0.1
Precipitates	33.4	39.8 ± 10.8	8.0 ± 1.3	16.9 ± 3.3	1.9 ± 0.1

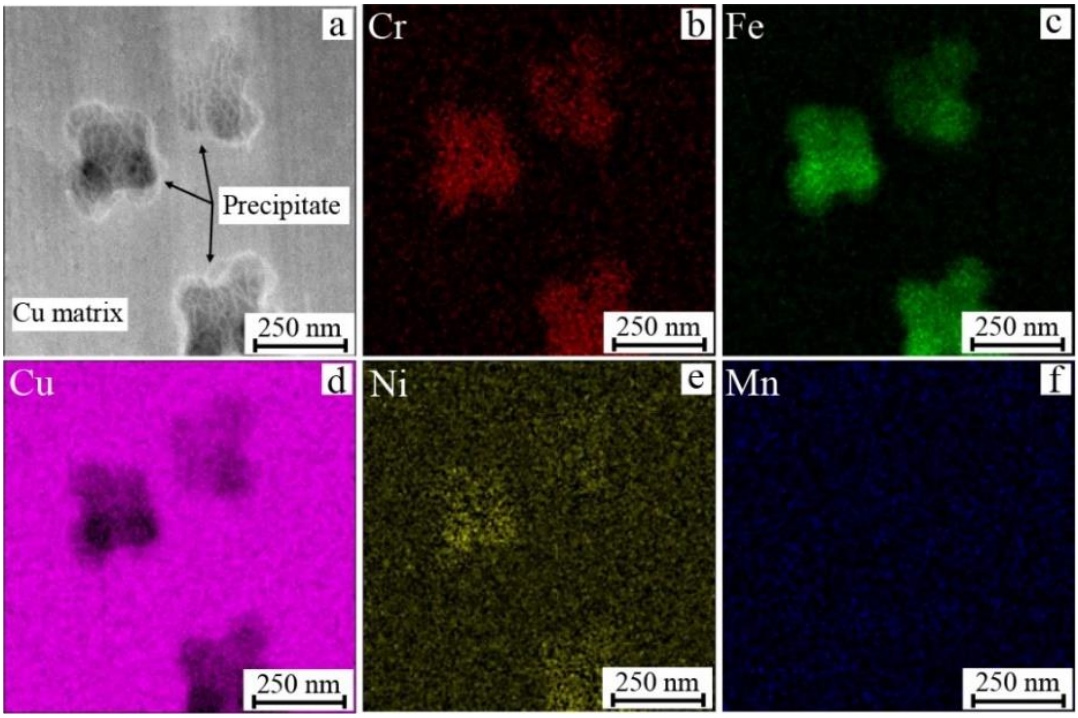

Figure 5-8: (a) HAADF imaging of petal-shaped precipitates; (b) to (f) STEM-EDX element mapping

To this point, it is critical to verify the EDX results by comparing with the theoretical elemental migration during brazing. It is known that diffusion coefficient increases with temperatures, it is thus reasonable to consider the high temperature regime only during the brazing cycle (~1050 °C and above, Figure 3-2), where most elemental diffusion would happen. Since EDX result indicates that Mn was homogeneously distributed within the joint region, Table 5-2 and Figure 5-8, diffusion characteristic of Mn in Cu is now briefly discussed.

Based on the data available from existing literature, diffusion coefficient of Mn in Cu at 1069.2 °C is 1490×10^{-15} m^2/s [128]. An estimation of the diffusion distance can be determined: $x = \sqrt{Dt}$, where x represents the diffusion distance, D and t are the diffusion coefficient and time, respectively. According to the brazing cycle, Figure 3-2, the duration above 1069.2 °C was ~12.5 min. The diffusion distance of Mn in Cu can thus be calculated as ~33.4 μm. Note the brazing temperature in the current study was 1120 °C, and pure Cu melts at 1084 °C. Therefore, the diffusion coefficient of Mn at 1120 °C will be much higher as there are more vacant lattice sites in molten Cu. Hence, the diffusion distance of Mn in molten copper is expected to be much higher than ~33.4 μm. Considering that inter-diffusion was to happen from both sides of the brazed joints, it is very likely that Mn would diffuse throughout the entire joint thickness of ~100 μm without segregation. In addition, Mn is completely soluble in

Cu and form Cu-Mn solid solution, which has fcc crystal structure and can be retained at room temperature when Mn is less than 83 at. % [129].

For other alloying elements (from the base metal) including Fe, Ni and Cr, the corresponding diffusion coefficients are at the same magnitude as compared to Mn [128,130]. It is thus expected that Fe, Ni and Cr would diffuse at a higher rate as compared to Mn because of their higher concentration within the base metal. Consequently, Fe, Ni and Cr are expected to distribute homogeneously within the copper matrix without any chemical gradients. Since Fe, Ni and Cr were associated with the star-shaped precipitates, Figure 5-8, the homogeneously distributed precipitates (Figure 5-4 and Figure 5-5) can also be considered as an experimental evidence to support the claim of homogeneous distribution of Fe, Ni and Cr.

Based on the STEM-EDX elemental analysis as well as the theoretical considerations, the matrix can be treated as a solid-solution of copper with iron, chromium, nickel and manganese being the solute elements. Therefore, a classic model for substitutional solid-solution strengthening based on elastic dislocation solute interactions [115] was applied:

$$\sigma_{ss} = \frac{MG\delta_{ss}^{3/2}c^{1/2}}{700} \tag{5-4}$$

where c is the molar ratio of the solute elements in the copper matrix. The interaction parameter δ_{ss} can be simplified as $\delta_{ss} = |3\delta_{matrix\text{-}solute}|$ [131,132]. $\delta_{matrix\text{-}solute}$ is the lattice constant misfit between the copper matrix and corresponding solute element. For example, the lattice constant misfit $\delta_{matrix\text{-}Fe}$ was calculated as 23.3% by adopting the lattice constant of 0.374 nm for Cu matrix (SAED, Figure 5-6(b)) and 0.287 nm for Fe, respectively. By adopting elemental distribution obtained from STEM-EDX, Table 5-2, the solid-solution strengthening effect can be readily calculated. For example, solid-solution strengthening due to the presence of Fe (converted molar ratio c = 3.3%) was ~20 MPa. Similarly, solid-solution strengthening induced by Cr, Ni and Mn were ~10 MPa, ~3 MPa and ~200 MPa, respectively. In sum, the enhancement caused by Mn plays a vital role in the solid-solution strengthening among all the substitutional elements in the copper/stainless steel brazed joint. In fact, Mn was known to cause strengthening effect when added into Cu [133], where the Cu-4.0 Mn (wt. %) alloy had an ultimate tensile strength of ~500 MPa. Therefore, it is concluded that Cu-Mn solid solution dominated the overall strengthening of the brazed joints.

5.8 Conclusions

This chapter examined the microstructural characteristics of the Type 304 stainless steel brazed joints. This includes the grain size and texture of the joint region, together with the hardness heterogeneity that was derived by using instrumented nanoindentation. In addition, elemental distribution was evaluated by EDX and the theoretical joint strength was estimated according to the collected microstructural data. Based on the results obtained the following conclusions can be made:

1. There were two primary phases within the joint region: the copper-rich matrix and the iron-copper-rich precipitates.
2. Hardness values measured by instrumented nanoindentation revealed increased strength of 1.1 GPa for the joint region, which was significant higher when compared to the bulk filler metal.
3. The copper matrix was rich in copper with small amount of iron, chromium, nickel and manganese. Manganese was homogeneously distributed throughout the joint region while iron, chromium and nickel are location-dependent, with significant concentration at the precipitates.
4. Theoretical evaluation of the joint strength has suggested that Cu-Mn solid-solution strengthening dominated the overall strengthening of the brazed joints, whereas contributions from precipitation hardening and grain size reduction strengthening were limited.

Taking the fracture strength of polycrystal copper as ~200 MPa, the theoretical fracture strength of the brazed joint can be predicted as ~400 MPa when adding the Cu-Mn solid-solution contribution linearly. However, this theoretically calculated material strength is still lower than the experimentally derived σ_f of ~500 MPa, Figure 4-1. Hence, the microstructural contribution alone cannot explain the enhanced mechanical strength of the brazed joint.

Chapter 6. Mechanical constraint

6.1 Introduction

One immediate question might arise as to whether the mechanical constraint induced stress triaxiality, can be used to reconcile the discrepancy between the calculated fracture strength of ~400 MPa and the experimental fracture stress of ~500 MPa, Figure 4-1. To address this, 45° joint configuration was employed, i.e. the brazed joint was orientated at 45° with respect to the loading direction. The design of 45° joint aimed at promoting a shear-type of failure as the maximum in-plane shear stress is inclined at 45° with respect to the tension axis. As demonstrated in previous simulation work [26,29], the level of stress triaxiality of axisymmetric tensile specimens, angled at 30° to 45° with respect to the far-field loading axis, were much reduced as compared to that of 90°. Thus, the 45° joint configuration would plastically deform in shear under a reduced level of mechanical constraint (i.e. a low stress triaxiality) as compared to the 90° counterpart, enabling a direct comparison of the overall strength of brazed joints under different mechanical constraint levels. Interrupted tensile testing was also conducted on the 45° and 90° brazed joints to understand the microscopic aspect of mechanical constraint. For this purpose, flat specimens were used to allow direct observation of the plastic flow of the brazed joint at 45° and 90° orientations. In addition, uniaxial tensile testing was also performed on these flat specimens. The fracture strengths of the flat specimens were compared with those from the cylindrical specimens, to ensure that the mechanical constraint being on the same level for both designs.

The design and tensile test results of the 45° joint configuration is given in Section 6.2. This is followed by investigation of plastic flow of the 45° and 90° brazed joints in Section 6.3. Finally, the mechanical constraint effect and its contribution to the mechanical strength is discussed in Section 6.4, together with the microscopic aspect of mechanical constraint.

6.2 Fracture strength and fractography of 90° and 45° brazed joints

For the 45° joint configuration, copper foil was inserted in between the stainless steel blocks, Figure 6-1(a), at 45° with respect to the loading direction. The extraction of tensile specimens was identical to that performed on the 90° brazed joint, Figure 6-1(b) and Figure 3-1. Note that the 45° brazed joint had similar equiaxed grains, weak texture, and an average

grain size of 60.3 ± 7.2 µm (for brevity, results are not shown in this work). Three specimens per joint design (90° and 45° orientations) were tensile loaded to failure and the average property was derived. The interrupted tensile tests were performed, and the specimens were loaded up to 90% of the final fracture stress.

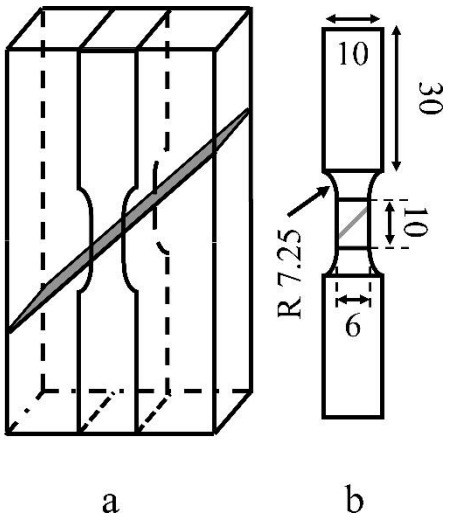

Figure 6-1: (a) Fabrication of the 45° joint; (b) flat tensile specimen with the brazed joint orientated at 45° with respect to the loading direction

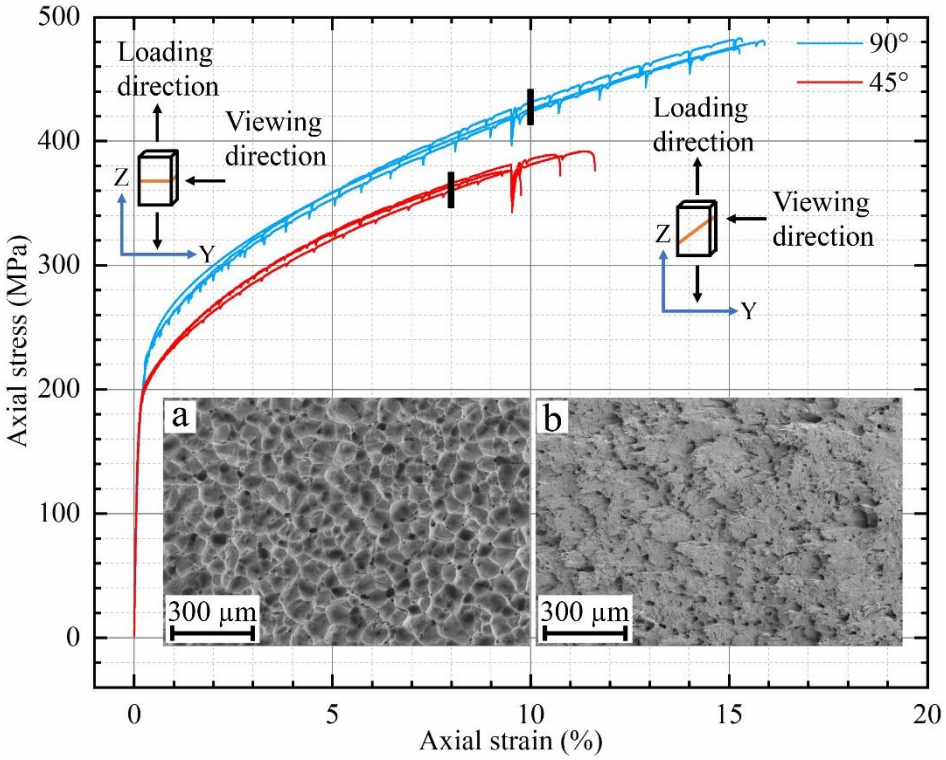

Figure 6-2: Axial stress-strain curves of the 90° and 45° brazed joint. Insets (a) and (b) represent fracture surfaces of the 90° and 45° joint configurations, respectively

Table 6-1: Tensile properties of the 90° and 45° brazed joint configurations

Material	σ_y (MPa)	σ_f (MPa)	ε (%)	90% of σ_f (MPa)
90° brazed joint	226 ± 0.1	478.7 ± 4.2	15.4 ± 0.3	~430
45° brazed joint	206 ± 0.1	385.6 ± 8.5	10.6 ± 0.9	~345
Polycrystalline pure copper [134]	~50	~200	32.4	N/A

The engineering stress-strain curves of the 90° and 45° brazed joints are presented in Figure 6-2. The corresponding 0.2% offset yield stress, σ_y, fracture stress, σ_f, as well as elongation-to-failure strain, ε, are summarised in Table 6-1. Tensile properties of polycrystalline copper as well as precipitation-hardened copper obtained from the literature are also listed in Table 6-1 for comparison. The 90° brazed joint had a fracture stress of 478.7 ± 4.2 MPa and elongation-to-failure strain of 15.4 ± 0.3%. The fracture surface, as shown in the inset (a) in Figure 6-2, revealed equiaxed dimples with sizes ranging from 30 μm to 100 μm, suggesting a ductile fracture mode. Overall, the 90° brazed joint exhibited enhanced tensile strength (both σ_y and σ_f) when compared to the filler metal (i.e. polycrystalline pure copper), Table 6-1. This observation is consistent with the nanoindentation results, Figure 5-3(b), in terms of revealing enhanced mechanical strength. In addition, the fracture strength σ_f of ~480 MPa is similar to those obtained from the cylindrical specimens of ~500 MPa, thus confirming that the mechanical constraint conditions for these two specimens are on the same level.

The 45° brazed joint had a fracture stress of 385.6 ± 8.5 MPa with elongation-to-failure strain of 10.6 ± 0.9%, being ~20% lower than the 90° counterpart, Table 6-1. The yield strength of 206 ± 0.1 MPa was also lower than that of 226 ± 0.1 MPa for the 90° counterpart, Figure 6-2. Note the strains were obtained based on the 10 mm gauge sections of the tensile specimens. Thus, the strain values reported in Figure 6-2 included elongations of the stainless steels and the brazed joints. SEM fractography revealed elongated dimples, indicating a shear-failure mode, inset (b) in Figure 6-2. To this end, the load for conducting interrupted tensile tests was taken as ~430 MPa and ~345 MPa (90% fracture strength) for the 90° and 45° joint configurations, respectively, Table 6-1. Since the joint microstructures were identical for the 90° and 45° configurations, Figure 5-1, the lower tensile strength of the 45° joint can be attributed to the reduced mechanical constraint effect. The elongated dimples on the fracture of the 45° joint also substantiated the purpose of introducing a shear-dominated fracture mode.

6.3 Plastic flow characteristics

Figure 6-3(a) and Figure 6-3(d) present SEM-BSE images for the 90° and 45° brazed joints strained to 90% of the fracture stress (~430 MPa and ~345 MPa, respectively), and the viewing direction (Y axis) is indicated in Figure 6-2. It was found that dislocation contrast selectively appeared at certain grains in the 90° joint, Figure 6-3(a), suggesting a preferred slip occurring with respect to the active slip systems. By comparison, dislocation contrast was uniformly distributed for the 45° counterpart, indicating homogeneous plastic deformation. Figure 6-3(b) and Figure 6-3(e) reveal the deformation characteristics within individual grains of the 90° and 45° joint configurations where the banded structures are present. Higher-magnification SEM images reveal the formation of extended boundaries for the banded structures, Figure 6-3(c) and Figure 6-3(f). These boundaries are characteristics of dislocation cell block structures as their appearance is a consequence of accommodation of slip system differences [64]. TEM observation of similar dislocation structures [64] confirmed these two types of boundaries, i.e. geometrically necessary boundaries (GNBs) that separate the cell block structures and incidental dislocation boundaries (IDBs) defining equiaxed volumes in between the GNBs [1]. This is illustrated in Figure 6-3(c) and Figure 6-3(f) where the solid yellow lines represent the GNBs and the dotted lines (in between solid yellow lines) denote IDBs. It was also reported by Hughes and Hansen [58] that GNBs are dense dislocation walls composed of GNDs, which are developed from slip system differences due to inhomogeneous plastic deformation [53]. In contrast, IDBs are groups of statistically stored dislocations being developed by mutual trapping of dislocations in the form of tangles and dipoles [1].

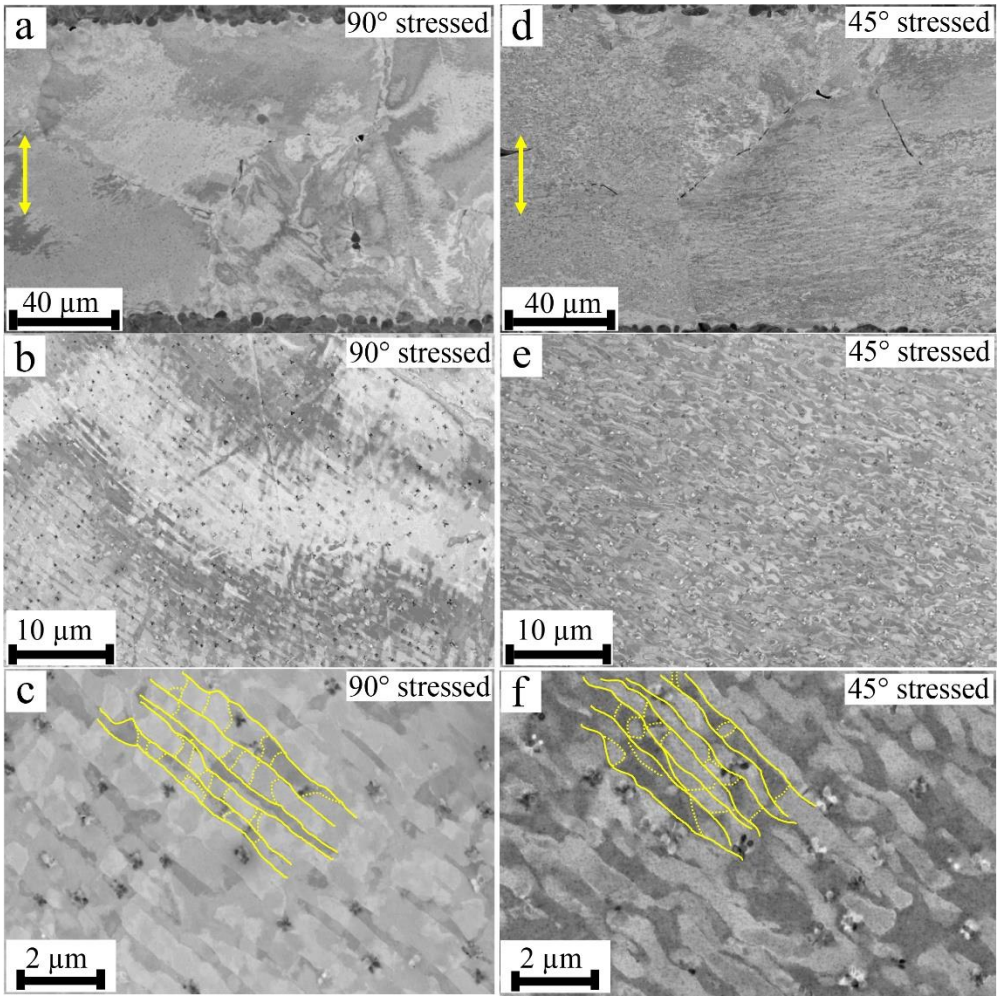

Figure 6-3: SEM-BSE images of brazed joints strained to 90% of the fracture stress, (a) to (c) 90° joint configuration; (d) to (f) 45° joint configuration. The loading direction is indicated by yellow arrows in (a) and (d)

The GNB spacings of the 45° and 90° joints were measured in ImageJ (intersect method) and the average value was reported, this was determined from more than 100 cell block structures across multiple grains. As representatively demonstrated in Figure 6-3(c) and Figure 6-3(f), GNB spacing in the 45° joint (0.33 ± 0.15 µm) was smaller than the 90° counterpart of 0.43 ± 0.15 µm. According to the evolution theory for dislocation cell block structures [61], new GNBs would always form preferentially within thicker cell block structures. This would allow subdivision of cell block structures to accommodate additional lattice curvature, hence reducing the overall GNB spacing. In addition, Mishin et al. [54] reported that GNB spacing would decrease with increased plastic strain, while misorientations across them increase. Hence, the smaller GNB spacing indicates a higher strain level for the 45° brazed joint. Since the 90° and 45° joints were subjected to 90% of the corresponding fracture stresses (~430 MPa

and ~345 MPa, respectively), the 45° joint thus showed a higher strain level at a lower applied stress. This finding substantiates that the 45° brazed joint was less constrained when compared to the 90° counterpart. The higher strain level also supports that the critically resolved shear stress was maximised when inclined at 45° in respect to the tension axis, as was also substantiated by the fracture surface observed from tensile test of these samples, Figure 6-2.

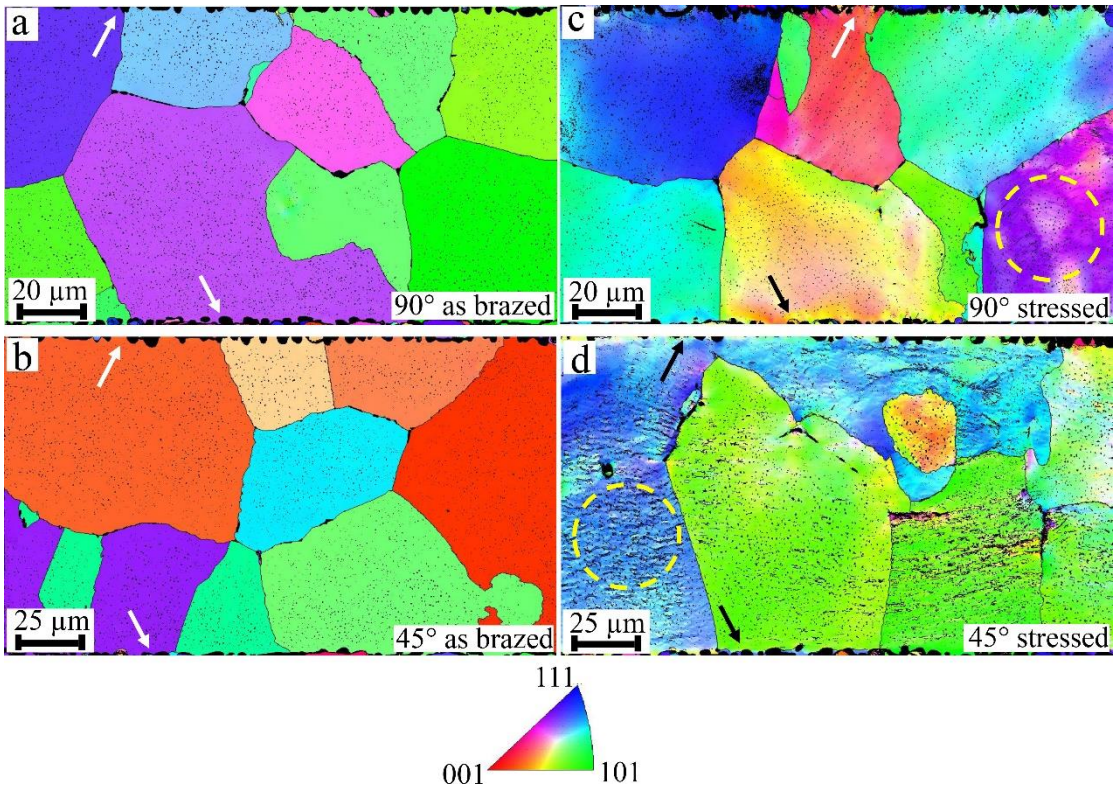

Figure 6-4: (a) and (b) EBSD orientation maps of 90° and 45° joint configuration at as-brazed condition; (c) 90° and (d) 45° brazed joints that had been strained to 90% of the fracture stress

Figure 6-4 shows EBSD orientation maps of the 90° and 45° joints, with Figure 6-4(a) and Figure 6-4(b) for the as-brazed (i.e. no-stress) condition, while Figure 6-4(c) and Figure 6-4(d) are for the strained condition. The macroscopic base-filler metal interfaces are indicated by white arrows. The EBSD measurement noise increased with the increasing plastic strain due to the lattice distortion induced by the increase in dislocation density, i.e. indexing success rate [53]. Nevertheless, greater than 90% indexing success rate was always achieved for the heavily strained specimens in the present work. This made the subsequent detailed GND analysis reliable. The black dots within individual grains in Figure 6-4(a) and Figure 6-4(b) corresponded to the star-shaped precipitates that cannot be resolved in these EBSD scans. The presence of local strain gradient for both the 90° and 45° joints after being strained to 90% of

the fracture stress, Figure 6-4(c) and Figure 6-4(d), were revealed by the large degree of misorientation induced lattice curvature. The regions with alternating colours highlighted by dashed circles in Figure 6-4(c) and Figure 6-4(d) corresponded to the cell block structures observed in Figure 6-3(c) and Figure 6-3(f).

To further reveal the influence of mechanical constraint on the plastic flow of brazed joint, EBSD scan of a larger field-of-view at a refined step size of 0.1μm was performed and the results are shown in Figure 6-5. The viewing direction was along the X axis indicated in Figure 6-2. It can be seen that dislocation contrast selectively appeared at certain grains in the 90° joint, Figure 6-5(a), whereas dislocation contrast was uniformly distributed for the 45° counterpart. This observation is consistent with SEM-BSE images presented in Figure 6-2 and confirms that the 45° brazed joint was less constrained when compared to the 90° joint. As a result of the refined EBSD step size, interfacial products were readily revealed, the white arrows in Figure 6-5 indicates the base-filler metal interface as well as the interfacial products.

Interfacial products with similar morphologies were recently reported in brazing of stainless steel materials. For example, interfacial products were revealed via EBSD for Type 316L stainless steel brazed joint processed with BNi-2 filler metal [135,136]. Zhang et al. [137] reported Cu-Ni and Fe-Ni intermetallic compounds as interfacial products at the base-filler metal interface of 316L stainless steel brazed joints processed with Cu alloys. In addition, Wei et al. [138] reported that these interfacial phases were bcc crystal structure, and these were formed by phase transformation from fcc during the cooling process. However, the underlaying mechanism of such phase transformation was not specified. For the brazed joints studied in the current work, all the base metals were prepared to different surface roughness conditions. It is therefore postulated that the observed interfacial products could also form via static recrystallisation. During the high temperature of brazing, the accumulated strain energy on the surface layer of the base metal would become the driving force to nucleate new dislocation-free grains, followed by subsequent grain growth during cooling. However, additional experiment is needed to validate this claim and no evidence could be identified from the existing literature to support this hypothesis. Since the observed interfacial phases could contribute towards the strength of the brazed joints and detailed characterisation of these would develop in-depth understanding of the strengthening mechanism, systematic study of these interfacial phases would be my future target.

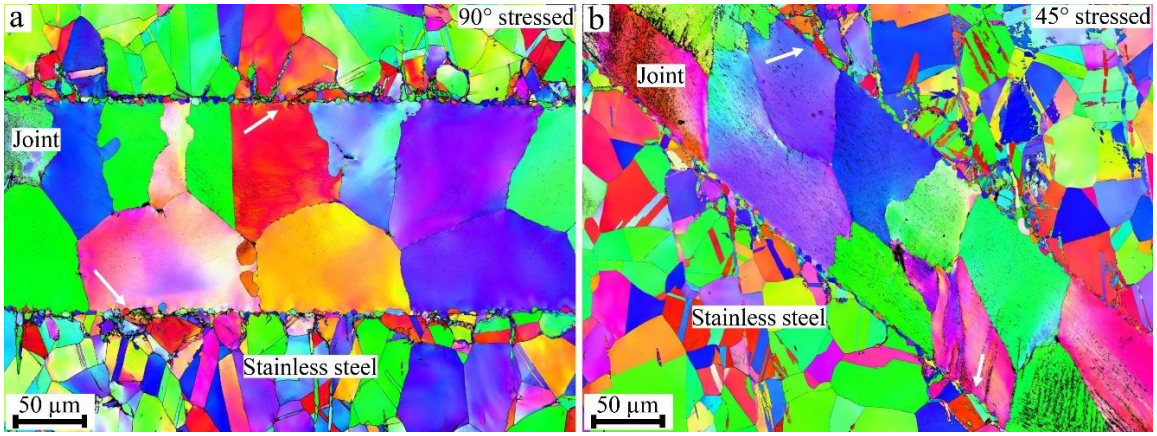

Figure 6-5: (a) and (b) EBSD orientation maps of 90° and 45° joint configuration at 90% strained condition; the viewing direction is along the X-axis as indicated in Figure 6-2

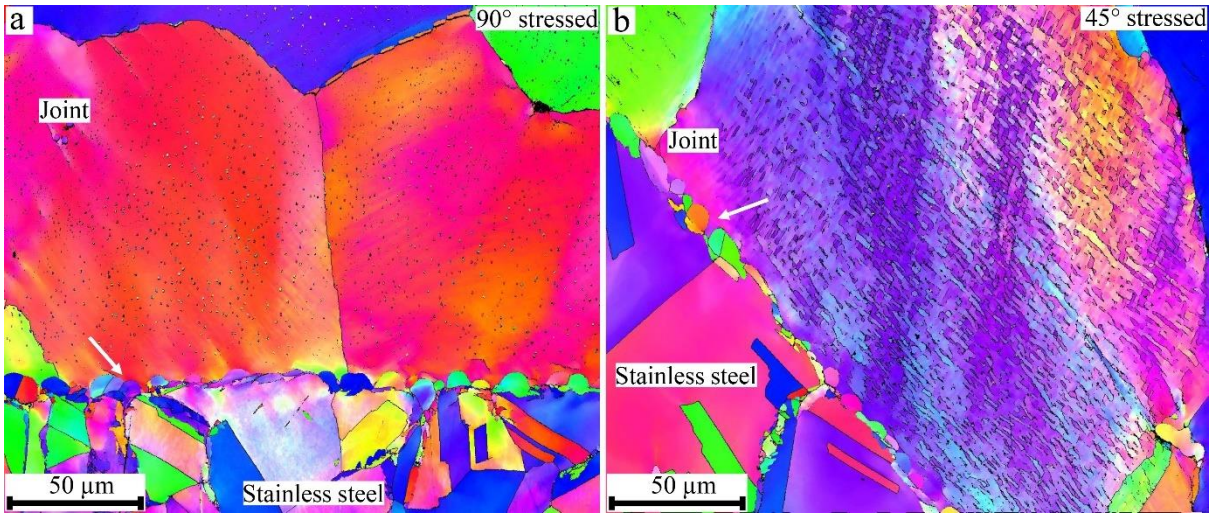

Figure 6-6: (a) and (b) EBSD orientation maps of 90% strained 90° and 45° joints at higher magnification; the viewing direction is along the X-axis as indicated in Figure 6-2

EBSD orientation map at a higher magnification is presented in Figure 6-6, where the interfacial products (white arrows) as well as the star-shaped precipitates can be clearly seen. In addition, plastic flow of the 45° joint configuration reveals dislocation cell block structures that are identical to those observed in Figure 6-3(c) and Figure 6-3(f). Large degrees of misorientations can be seen at the extended boundaries of the cell block structures, Figure 6-6(b). This observation supports that GNBs were developed to accommodate different active slip systems, and the extended boundaries of GNBs were associated with large degrees of misorientation [139].

6.4 Discussion

6.4.1 Contribution of mechanical constraint

The strengthening effect induced by the mechanical constraint effect is now calculated to fill the gap between the theoretical joint strength of ~400 MPa (Cu-Mn solid-solution strengthening) and the experimentally determined value of ~480 MPa, Figure 6-2, Table 6-1. For the 90° brazed joint that was under uniaxial tensile loading, both the base and filler metal would elongate in the longitudinal direction and contract in the transverse direction. However, plastic deformation of the joint would be restricted by the base metal due to elastic-plastic incompatibility, thereby introducing stress triaxiality. The stress state and deformation of brazed joints are therefore analogous to a specimen undergoes necking. As schematically shown in Figure 6-7(a), upon necking, the uniaxial stress state is modified by the geometrically irregularity, leading to the presence of a triaxial stress state [140]. It then becomes important to derive the longitudinal flow stress after necking, i.e., correcting the experimentally obtained fracture stress.

For isotropic cylindrical specimens under tensile loading, Bridgman [19] formulated a geometric approximation to obtain the longitudinal flow stress σ_{TB} that accounts for the presence of the transverse components of stress σ_r and σ_θ, Figure 6-7(a), assuming a uniform strain distribution in the minimum cross-section:

$$\sigma_{TB} = \sigma_T \left[\left(1 + \frac{2R}{a} \right) \ln \left(1 + \frac{a}{2R} \right) \right]^{-1} \tag{6-1}$$

where σ_T represents the true flow stress prior to applying the Bridgman correction, a is the internal radius of the tensile specimen at the minimum cross section, and R is the radius of the external curvature of the necking profile as indicated in Figure 6-7(b). Although the Bridgman necking criteria was developed for cylindrical specimens, Zhang et al. [141] confirmed that it can be used for specimens with rectangular cross sections and the correction of longitudinal flow stress was independent of the cross-section aspect ratio.

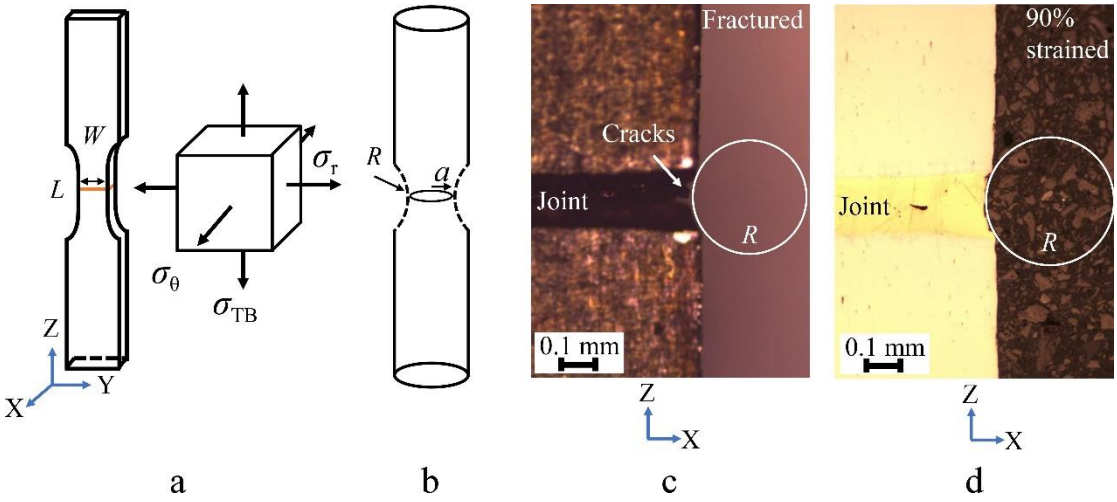

Figure 6-7: (a) Illustration of specimen width and thickness, as well as stress triaxiality; (b) Bridgman necking parameters *R* and *a*; (c) determination of *R* on Z-X plane; (d) *R* values for specimens strained to 90% of the fracture stress

Table 6-2: Average and standard deviation (STDEV) of thickness and width of specimens before (*W* & *L*) and after (*W'* & *L'*) tensile failure; Bridgman necking parameters of the internal radius *a* and external curvature radius *R* observed on Z-X and Z-Y planes

	Specimen width & thickness (mm)						Bridgman necking parameters (mm)					
		Before loading		After failure			Z-X plane			Z-Y plane		
	σ_f	*W*	*L*	*W'*	*L'*	σ_T	*a*	*R*	σ_{TB}	*a*	*R*	σ_{TB}
Average	478.7	5.92	2.94	4.95	2.45	687.7	1.22	0.20	367.6	2.48	0.37	359.3
STDVE	4.2	0.02	0.05	0.04	0.04	11.6	0.02	0.02	8.1	0.02	0.02	4.7

In this work, we firstly calculated the true flow stresses σ_T at sample fracture of the brazed joints. This was achieved by considering the reduced cross-sectional area that was measured from the fracture surfaces. Measurement of the thickness and width before (*W* & *L*) and after (*W'* & *L'*) tensile failure was performed on three tensile specimens. The average values were calculated and are given in Table 6-2. Note, the average Bridgman necking parameters are also listed in Table 6-2. To this end, the average width of tensile specimens reduced from 5.92 mm (*W*) to 4.95 mm (*W'*) and the thickness reduced from 2.94 mm (*L*) to 2.45 mm (*L'*). The true flow stress at sample fracture σ_T was thus determined as 687.7 MPa, Table 6-2.

The Bridgman necking parameter *R* was measured from the fractured tensile specimens as shown in Figure 6-7(c). Circles were used to fit the external curvature in the necking region and the radius was considered as the *R* values. The average value of *R* derived from Z-X plane

was 0.20 mm, Table 6-2. To ensure the accuracy of *R*, Zhang et al. [142] proposed to verify the deformed cross sections by performing interrupted tensile tests. Therefore, we examined the external curvature radius of specimens that had been strained to 90% of the fracture stresses. The radius values ranged from ~0.20 mm to ~0.30 mm when observing on Z-X plane, Figure 6-7(d).

Therefore, we can confirm that the Bridgman necking parameter *R* determined from the failed specimen (0.20 mm, Table 6-2) is accurate, as it is similar to that determined from the interrupted tensile specimens. The Bridgman necking parameter *a* (internal radius at the minimum cross section) was taken as half of the width of the specimen after tensile failure, i.e. *a* was taken as 1.22 mm when observing on Z-X plane. Thus, Eq. (6-1) was adopted to derive the longitudinal flow stress σ_{TB}, which was 367.6 MPa when calculated with parameters from the Z-X plane, Table 6-2. Similarly, σ_{TB} of 359.3 MPa was also calculated based on parameters obtained from Z-Y plane, Table 6-2. To this end, σ_{TB} derived from Z-X and Z-Y planes are similar and the average value is taken as ~360 MPa.

The longitudinal flow stress σ_{TB} of ~360 MPa suggests that the brazed joints would fail at a much lower stress level without the presence of mechanical constraint. This value is only slightly lower than the theoretical fracture strength of ~400 MPa based on Cu-Mn solid-solution contribution. Hence, it is judged that the longitudinal flow stress σ_{TB} at sample fracture agrees reasonably well with the theoretical joint strength. In addition, difference between the longitudinal flow stress σ_{TB} (~360 MPa) and the true flow stress σ_T at sample fracture (~690 MPa) is considered as the contribution of mechanical constraint, i.e. ~330 MPa. Therefore, the enhanced tensile strength of brazed joints can be considered as a combined effect of microscopic Cu-Mn solid-solution strengthening and macroscopic mechanical constraint effect.

6.4.2 Microscopic explanation for mechanical constraint

By creating the 45° brazed joint configuration (base-filler metal interface at 45° with respect to the loading axis), the level of mechanical constraint was reduced (lower stress triaxiality). To provide a microscopic explanation to the mechanical constraint, it is important to examine the GND distribution across the brazed joints. GND distribution was calculated for the 90° and 45° joint configurations for the as-brazed and strained condition. The kernel average misorientation (KAM) method was used to determine the local misorientation. Using continuum dislocation mechanics developed by Nye and Kroner [46], the dislocation density can be related to the lattice curvature assuming neglectable elastic strain. Note that EBSD-

based dislocation analysis considers GNDs only [32]. This is because GNDs are associated with long-range lattice curvature, whereas statistically stored dislocations are in the form of tangles without a net Burgers vector [53]. It is also realised that GND density derived from EBSD varies with step size [36]. Hence, the step size for EBSD scans in the current work was kept as 0.25 μm to minimise the measurement error.

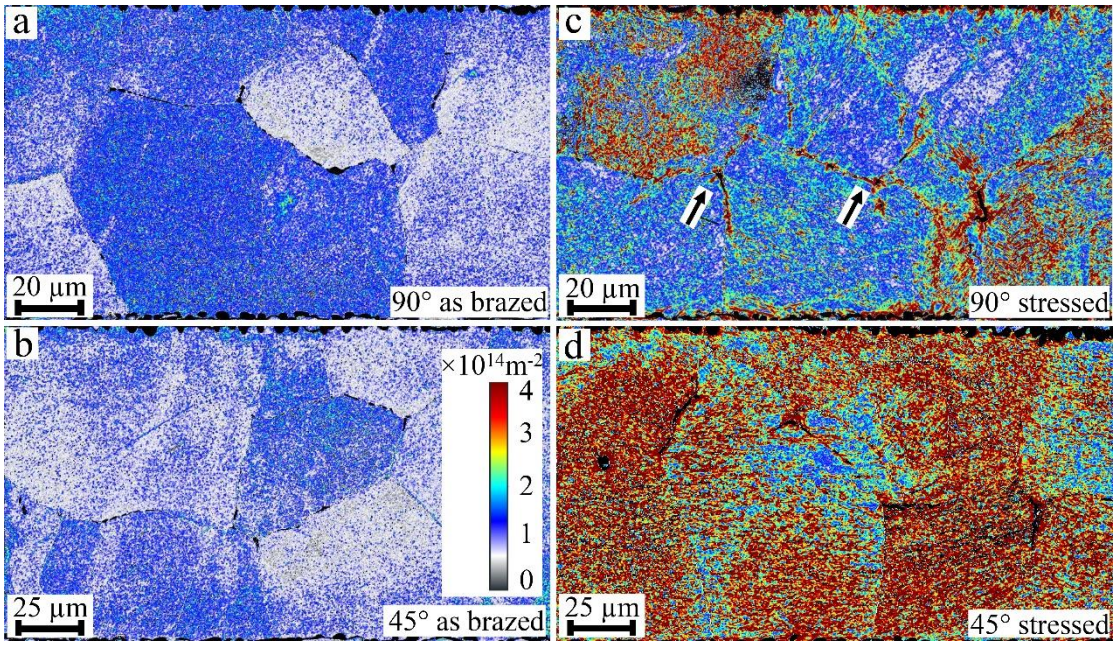

Figure 6-8: (a) and (b) GND distributions within the 90° and 45° joints for the as-brazed condition; (c) and (d) GND distributions for the strained condition

Figure 6-8 shows the derived GND density within the 90° and 45° joints for the as-brazed, Figure 6-8(a) and Figure 6-8(b), and the strained condition, Figure 6-8(c) and Figure 6-8(d). The overall GND density was relatively low at as-brazed condition, being 1.0×10^{14} m^{-2} for both joint configurations, Figure 6-8(a) and Figure 6-8(b). For the 90° joint at strained condition, high GND density was observed for certain grains that were potentially favourably orientated, Figure 6-8(c). This is consistent with the observation of selectively occurred dislocation contrast for the 90° joint, Figure 6-3(a). In addition, GND density was higher near grain boundaries and triple junctions, see arrows in Figure 6-8(c), with a lower GND density within grain interiors. These observations comply with Ashby's theory [52] that GNDs are generated to ensure lattice continuity [21]. For the 45° joint at strained condition, Figure 6-8(d), GND density was uniformly distributed across the joint region, supporting homogeneous dislocation contrast in Figure 6-3(d).

To provide a quantitative measure of GND distribution, in particular near the base-filler metal interface, the average GND density was derived at different distances to the interface as shown in Figure 6-9. For the as-brazed joint, GND density (circular symbols) was 1.0×10^{14} m^{-2} for both 90° and 45° configurations, confirming no GND segregation near the interfaces at as-brazed condition. At 90% strained condition, the 45° joint (hollow symbols) showed high GND density of 3.0×10^{14} m^{-2} across the joint region without much fluctuations. In contrast, GND gradient was clearly revealed for the 90° joint (black triangular), being 2.5×10^{14} m^{-2} in the vicinity of the interface and 1.7×10^{14} m^{-2} in the joint centre at 10 to 100 μm away from the interface, Figure 6-9.

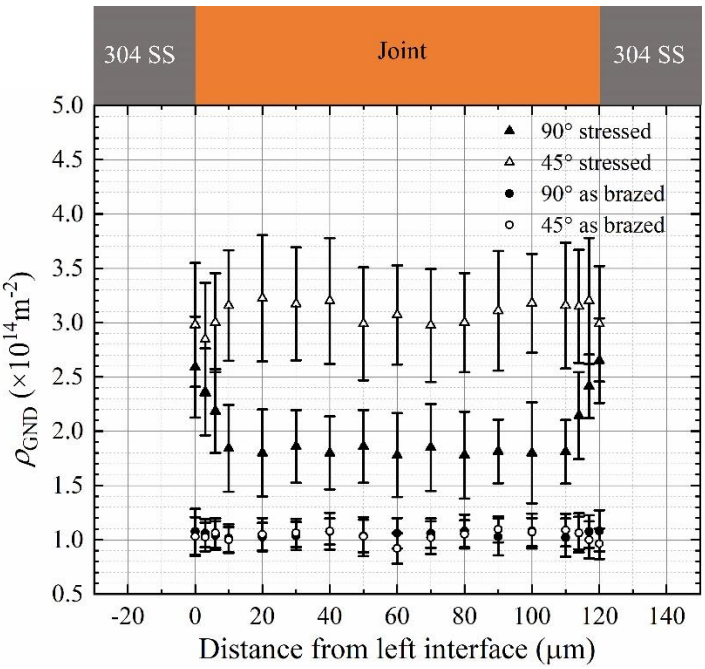

Figure 6-9: Average GND densities within the 45° and 90° brazed joints at different distances to the base-filler metal interface

The GND gradient in the 90° joint confirms the presence of elastic-plastic incompatibility between the base and filler metal imposed by the mechanical constraint. In other words, GNDs were introduced to accommodate inhomogeneous plastic deformation as a consequence of mechanical constraint. This finding is thus considered as an experimental (microscopic) evidence for strain inhomogeneity due to the presence of mechanical constraint. In contrast, uniform GND distribution in the 45° joint shows a reduced mechanical constraint effect. This agrees with our findings of smaller GNB spacings and lower tensile strength for the 45° brazed joints.

Recent studies [103] demonstrated that the overall strain hardening behaviour of copper/bronze laminate materials, with improvements in both strength and ductility, can be associated with the role of interfaces. Mechanistically, the property enhancement is a result of the geometric discontinuity of slip systems across the interfaces [143]. Lee et al. [144] suggested that strain gradient could occur due to inhomogeneous plastic deformation, which needs to be accommodated by GNDs at the interphase boundaries. Pile-ups of GNDs would generate back-stresses that countervail the forward motion of dislocations and therefore counterbalance the applied stress, leading to enhanced strength and ductility [145,146]. Thus, GND pile-ups at the base-filler metal interfaces observed within the brazed joint would potentially enhance the overall work hardening.

6.5 Conclusions

This Chapter elucidates the macroscopic material strengthening mechanism encountered in brazed joints. The following conclusions can be made:

1. The enhanced tensile strength of the brazed joint was a combined consequence of mechanical constraint and Cu-Mn solid-solution strengthening.
2. The mechanical constraint presented in the 90° joint led to an increased fracture strength, the calculation of longitudinal flow stress via the Bridgman necking criteria suggested a contribution of ~330 MPa. The mechanical constraint was responsible for reconciling the discrepancy between the calculated and experimentally determined strengths.
3. GND gradient was confirmed for the 90° joint, being 2.5×10^{14} m^{-2} near the interface and 1.7×10^{14} m^{-2} in the joint centre, whereas a homogeneous GND density of 3.0×10^{14} m^{-2} was found for the 45° joint. Pile-ups of GNDs at the base-filler metal interface provides an experimental (microscopic) evidence for strain inhomogeneity imposed by the mechanical constraint.

Chapter 7. Conclusions and recommendation of future work

In summary, the enhanced mechanical strength of copper-stainless steel brazed joints is a concurrent result of (i) Cu-Mn solid-solution strengthening, (ii) mechanical constraint. The mechanical constraint is a macroscopic effect, that is caused by elastic-plastic incompatibility between the base stainless steel and copper-rich joint region, Figure 7-1(a). The influence of mechanical constraint can be quantified via the Bridgman necking criteria and is present in brazed joints regardless of the specific material system. In contrast, the Cu-Mn solid-solution strengthening can be considered as a microscopic contribution. Material strength of a brazed joint can be estimated by considering the intrinsic strength of the filler metal (i.e. pure Cu in the current work) and additional strengthening caused by elemental inter-diffusion. This microscopic contribution is material dependent and can be modified by changing the processing parameters. Furthermore, GND pile-ups at the base-filler metal interface provides an experimental (microscopic) evidence for strain inhomogeneity imposed by the mechanical constraint, as schematically illustrated in Figure 7-1(b).

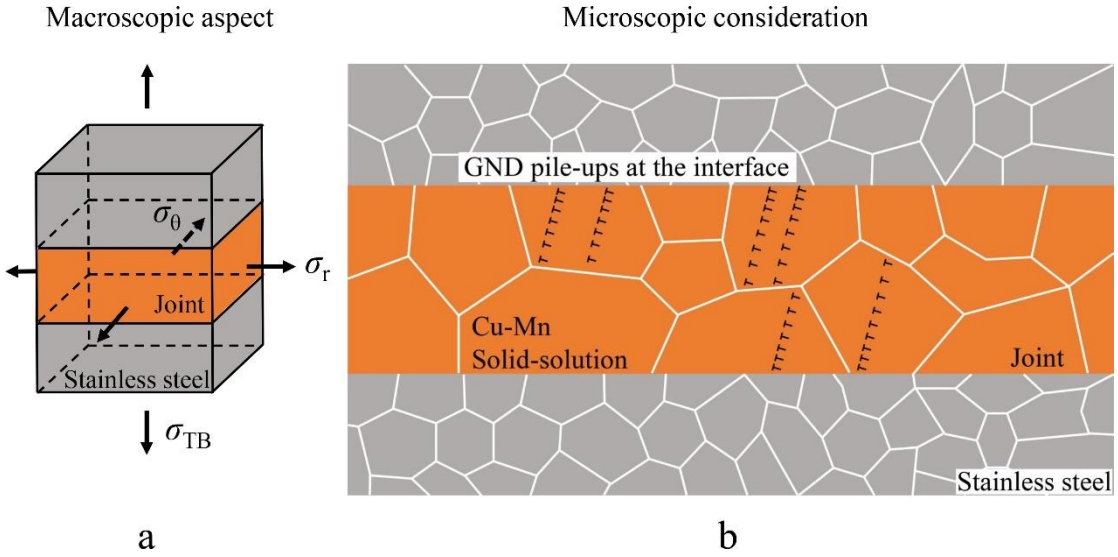

Figure 7-1: (a) Mechanical constraint and induced stress triaxiality in 90° brazed joint; (b) schematic illustration of Cu-Mn solid-solution strengthening and pile-ups of GNDs at the base-filler metal interface

According to the experimental investigation in Chapter 4, 5, and 6, some key findings are listed below:

1. Interface roughness conditions have negligible influence on the mechanical strength of the Type 304 stainless steel brazed joints. This is because failure of the brazed joints happened entirely within the joint region (in the centre of the filler metal) rather than at the interfacial region.
2. For defect-containing brazed joints, larger defects lead to higher fatigue crack growth rate at the initial stage. Qualitatively, the fatigue cycles to failure was found to decrease with the increase of defect size.
3. Theoretical evaluation of the brazed joint microstructure suggested that Cu-Mn solid-solution strengthening dominated the overall strengthening, whereas contributions from precipitation hardening and grain size strengthening were limited.
4. The contribution of mechanical constraint to the overall joint strength was estimated as ~330 MPa by adopting the Bridgman necking criteria.
5. The enhanced mechanical strength of brazed joint is a concurrent result of microscopic Cu-Mn solid-solution strengthening and macroscopic mechanical constraint effect.
6. The pile-ups of GNDs at the base-filler metal interface provides an experimental evidence for the strain inhomogeneity induced by the presence of mechanical constraint.

Based on the experimental observations in the current work, some future works are recommended and listed below:

1. To investigate different brazing processes to assess the influences of key processing parameters, such as brazing environment, time and cooling rate. For example, the brazing temperature and cooling rate can be refined to introduce a nanoscale dispersion of Fe-Cr-Cu precipitates that will further increase the joint overall strength.
2. To further characterise the properties of the copper-stainless steel brazed joints, i.e., to investigate low cycle fatigue and creep properties at both room and elevated temperatures.
3. To conduct detailed characterisation of the interfacial products at the base-filler metal interface. This includes their chemical composition and crystallographic characteristics, together with the corresponding formation process. In addition, plastic flow of these interfacial products and dislocation distributions can be explored via TEM examinations.

4. To conduct in-situ tensile test coupled with digital image correlation technique to investigate strain heterogeneity imposed by the presence of mechanical constraint in brazed joints.

Reference

[1] D.A. Hughes, N. Hansen, D.J. Bammann, Geometrically necessary boundaries, incidental dislocation boundaries and geometrically necessary dislocations, Scr. Mater. 48 (2003) 147–153.

[2] X. Huang, G. Winther, Dislocation structures. Part I. Grain orientation dependence, Philos. Mag. 87 (2007) 5189–5214.

[3] Granta, CES EduPack 2017, (2017).

[4] X.D. Hou, A.J. Bushby, N.M. Jennett, Study of the interaction between the indentation size effect and Hall-Petch effect with spherical indenters on annealed polycrystalline copper, J. Phys. D. Appl. Phys. 41 (2008).

[5] F. Silze, G. Wiehl, I. Kaban, H. Wendrock, T. Gemming, U. Kühn, J. Eckert, S. Pauly, Wetting behaviour of Cu-Ga alloys on 304L steel, Mater. Des. 91 (2016) 11–18.

[6] R.K. Roy, A.K. Panda, S.K. Das, Govind, A. Mitra, Development of a copper-based filler alloy for brazing stainless steels, Mater. Sci. Eng. A. 523 (2009) 312–315.

[7] F.P.L. Kavishe, T.J. Baker, Influence of joint gap width on strength and fracture toughness of copper brazed steels, Mater. Sci. Technol. 6 (1990) 176–181.

[8] A.J. West, H.J. Saxton, A.S. Telelman, C.R. Barrett, Deformation and failure of thin brazed joints-microscopic considerations, Metall. Mater. Trans. B Process Metall. Mater. Process. Sci. 2 (1971) 1009–1017.

[9] M.K. Ghovanlou, H. Jahed, A. Khajepour, Mechanical reliability characterization of low carbon steel brazed joints with copper filler metal, Mater. Sci. Eng. A. 528 (2011) 6146–6156.

[10] H.J. Saxton, A.J. West, C.R. Barrett, Deformation and failure of brazed joints-macroscopic considerations, Metall. Mater. Trans. B Process Metall. Mater. Process. Sci. 2 (1971) 999–1007.

[11] K. Chen, X. Chen, D. Ding, G. Shi, Z. Wang, Crystallographic features of iron-rich nanoparticles in cast Cu-10Sn-2Zn-1.5Fe-0.5Co alloy, Mater. Charact. 113 (2016) 34–42.

[12] K. Chen, X. Chen, Z. Wang, H. Mao, R. Sandström, Optimization of deformation properties in as-cast copper by microstructural engineering. Part I. microstructure, J. Alloys Compd. 763 (2018) 592–605.

[13] X. Chen, Z. Wang, D. Ding, H. Tang, L. Qiu, X. Luo, G. Shi, Strengthening and

toughening strategies for tin bronze alloy through fabricating in-situ nanostructured grains, Mater. Des. 66 (2015) 60–66.

[14] I. Kawakatsu, Y. Suezawa, Effects of surface preparations of base metal on the brazed joint strength, Trans. Japan Weld. Soeiet. 3 (1972).

[15] I.T. Hong, C.H. Koo, The study of vacuum-furnace brazing of C103 and Ti-6Al-4V using Ti-15Cu-15Ni foil, Mater. Chem. Phys. 94 (2005) 131–140.

[16] T. Zaharinie, Z. Huda, M.F. Izuan, M. Hamdi, Development of optimum process parameters and a study of the effects of surface roughness on brazing of copper, Appl. Surf. Sci. 331 (2015) 127–131.

[17] Y. Suezawa, Effects of surface roughness on the fatigue strength of brazed joint, Trans. Japan Weld. Soc. 7 (1976) 1677–1687.

[18] H. Wang, J. Cao, J. Feng, Brazing mechanism and infiltration strengthening of CC composites to TiAl alloys joint, Scr. Mater. 63 (2010) 859–862.

[19] P.W. Bridgman, Studies in large plastic flow and fracture, 1964.

[20] J. Kadkhodapour, S. Schmauder, D. Raabe, S. Ziaei-Rad, U. Weber, M. Calcagnotto, Experimental and numerical study on geometrically necessary dislocations and non-homogeneous mechanical properties of the ferrite phase in dual phase steels, Acta Mater. 59 (2011) 4387–4394.

[21] J. Jiang, T.B. Britton, A.J. Wilkinson, Evolution of dislocation density distributions in copper during tensile deformation, Acta Mater. 61 (2013) 7227–7239.

[22] H. Zhu, L. Zhu, J.H. Chen, X.F. Lv, Investigation of fracture mechanism of 6063 aluminum alloy under different stress states, Int. J. Fract. 146 (2007) 159–172.

[23] W.M. Garrison, N.R. Moody, Ductile fracture, J. Phys. Chem. Solids. 48 (1987) 1035–1074.

[24] A. Weck, D.S. Wilkinson, Experimental investigation of void coalescence in metallic sheets containing laser drilled holes, Acta Mater. 56 (2008) 1774–1784.

[25] J. Sun, Effect of stress triaxiality on micro-mechanisms of void coalesence and micro-fracture ductility of materials, Eng. Fract. Mech. 39 (1991) 799–805.

[26] X.W. Zhang, J.F. Wen, X.C. Zhang, X.G. Wang, S.T. Tu, Effects of the stress state on plastic deformation and ductile failure: Experiment and numerical simulation using a newly designed tension-shear specimen, Fatigue Fract. Eng. Mater. Struct. 42 (2019) 2079–2092.

[27] D. Wu, E.M. Christian, E.G. Ellison, Influence of constraint on creep stress distribution in notched bars, J. Strain Anal. 19 (1984).

[28] B.S. Henry, A.R. Luxmoore, The stress triaxiality constraint and the Q-value as a ductile fracture parameter, Eng. Fract. Mech. 57 (1997) 375–390.

[29] W. Li, F. Liao, T. Zhou, H. Askes, Ductile fracture of Q460 steel: Effects of stress triaxiality and Lode angle, J. Constr. Steel Res. 123 (2016) 1–17.

[30] A. Paggi, G. Angella, R. Donnini, Strain induced grain boundary migration effects on grain growth of an austenitic stainless steel during static and metadynamic recrystallization, Mater. Charact. 107 (2015) 174–181.

[31] L. Qian, X. Wang, C. Sun, A. Dai, Correlation of macroscopic fracture behavior with microscopic fracture mechanism for AHSS sheet, Materials (Basel). 16 (2019).

[32] T.J. Ruggles, T.M. Rampton, A. Khosravani, D.T. Fullwood, The effect of length scale on the determination of geometrically necessary dislocations via EBSD continuum dislocation microscopy, Ultramicroscopy. 164 (2016) 1–10.

[33] D.P. Field, C.C. Merriman, N. Allain-Bonasso, F. Wagner, Quantification of dislocation structure heterogeneity in deformed polycrystals by EBSD, Model. Simul. Mater. Sci. Eng. 20 (2012).

[34] C. Moussa, M. Bernacki, R. Besnard, N. Bozzolo, About quantitative EBSD analysis of deformation and recovery substructures in pure Tantalum, IOP Conf. Ser. Mater. Sci. Eng. 89 (2015).

[35] T.J. Ruggles, D.T. Fullwood, Estimations of bulk geometrically necessary dislocation density using high resolution EBSD, Ultramicroscopy. 133 (2013) 8–15.

[36] E. Demir, D. Raabe, N. Zaafarani, S. Zaefferer, Investigation of the indentation size effect through the measurement of the geometrically necessary dislocations beneath small indents of different depths using EBSD tomography, Acta Mater. 57 (2009) 559–569.

[37] J. Jiang, T.B. Britton, A.J. Wilkinson, Measurement of geometrically necessary dislocation density with high resolution electron backscatter diffraction: Effects of detector binning and step size, Ultramicroscopy. 125 (2013) 1–9.

[38] B.S. El-Dasher, B.L. Adams, A.D. Rollett, Viewpoint: Experimental recovery of geometrically necessary dislocation density in polycrystals, Scr. Mater. 48 (2003) 141–145.

[39] L.P. Kubin, A. Mortensen, Geometrically necessary dislocations and strain-gradient plasticity: A few critical issues, Scr. Mater. 48 (2003) 119–125.

[40] W. Pantleon, Resolving the geometrically necessary dislocation content by conventional electron backscattering diffraction, Scr. Mater. 58 (2008) 994–997.

[41] M. Calcagnotto, D. Ponge, E. Demir, D. Raabe, Orientation gradients and geometrically necessary dislocations in ultrafine grained dual-phase steels studied by 2D and 3D EBSD, Mater. Sci. Eng. A. 527 (2010) 2738–2746.

[42] B. Beausir, C. Fressengeas, Disclination densities from EBSD orientation mapping, Int. J. Solids Struct. 50 (2013) 137–146.

[43] H. Gao, Y. Huang, W.D. Nix, J.W. Hutchinson, Mechanism-based strain gradient plasticity - I. Theory, J. Mech. Phys. Solids. 47 (1999) 1239–1263.

[44] W.T. Read, W. Shockley, Dislocation models of crstal grain boundaries, Phys. Rev. 78 (1950).

[45] A.J. Wilkinson, D. Randman, Determination of elastic strain fields and geometrically necessary dislocation distributions near nanoindents using electron back scatter diffraction, Philos. Mag. 90 (2010) 1159–1177.

[46] J.F. Nye, Some geometrical relations in dislocated crystals, Acta Metall. 1 (1953) 153–162.

[47] C.J. Gardner, B.L. Adams, J. Basinger, D.T. Fullwood, EBSD-based continuum dislocation microscopy, Int. J. Plast. 26 (2010) 1234–1247.

[48] D.P. Field, P.B. Trivedi, S.I. Wright, M. Kumar, Analysis of local orientation gradients in deformed single crystals, Ultramicroscopy. 103 (2005) 33–39.

[49] A.J. Wilkinson, E.E. Clarke, T.B. Britton, P. Littlewood, P.S. Karamched, High-resolution electron backscatter diffraction: An emerging tool for studying local deformation, J. Strain Anal. Eng. Des. 45 (2010) 365–376.

[50] T. Zhang, D.M. Collins, F.P.E. Dunne, B.A. Shollock, Crystal plasticity and high-resolution electron backscatter diffraction analysis of full-field polycrystal Ni superalloy strains and rotations under thermal loading, Acta Mater. 80 (2014) 25–38.

[51] H. Lim, S. Subedi, D. T. Fullwood, B. L. Adams, R. H. Wagoner, A practical meso-scale polycrystal model to predict dislocation densities and the hallpetch effect, Mater. Trans. 55 (2014) 35–38.

[52] A. M.F., The deformation of plastically non-homogeneous materials, Philos. Mag. 21 (1969) 37–41.

[53] C. Moussa, M. Bernacki, R. Besnard, N. Bozzolo, Statistical analysis of dislocations and dislocation boundaries from EBSD data, Ultramicroscopy. 179 (2017) 63–72.

[54] O.V. V. Mishin, D. Juul Jensen, N. Hansen, D.J. Jensen, N. Hansen, Microstructures and boundary populations in materials produced by equal channel angular extrusion, Mater. Sci. Eng. A. 342 (2003) 320–328.

[55] Q. Liu, N. Hansen, Geometrically necessary boundaries and incidental dislocation boundaries formed during cold deformation, Scr. Metall. Mater. 32 (1995) 1289–1295.

[56] D.A. Hughes, D.C. Chrzan, Q. Liu, N. Hansen, Scaling of misorientation angle distributions, Phys. Rev. Lett. 81 (1998) 4664–4667.

[57] D.A. Hughes, Q. Liu, D.C. Chrzan, N. Hansen, Scaling of microstructural parameters: Misorientations of deformation induced boundaries, Acta Mater. 45 (1997) 105–112.

[58] D.A. Hughes, N. Hansen, Microstructure and strength of nickel at large strains, Acta Mater. 48 (2000) 2985–3004.

[59] R.A. Jago, N. Hansen, Grain size effects in the deformation of polycrystalline iron, Acta Metall. 34 (1986) 1711–1720.

[60] D. Kuhlmann-Wilsdorf, N. Hansen, Geometrically necessary, incidental and subgrain boundaries, Scr. Metall. Mater. 25 (1991) 1557–1562.

[61] A. Godfrey, D.A. Hughes, Scaling of the spacing of deformation induced dislocation boundaries, Acta Mater. 48 (2000) 1897–1905.

[62] B. Bay, N. Hansen, D.A. Hughes, D. Kuhlmann-Wilsdorf, Overview no. 96 evolution of f.c.c. deformation structures in polyslip, Acta Metall. Mater. 40 (1992) 205–219.

[63] D. Kuhlmann-Wilsdorf, Theory of plastic deformation: properties of low energy dislocation structures, Mater. Sci. Eng. A. 113 (1989) 1–41.

[64] Q. Liu, D. Juul Jensen, N. Hansen, Effect of grain orientation on deformation structure in cold-rolled polycrystalline aluminium, Acta Mater. 46 (1998) 5819–5838.

[65] V. Randle, N. Hansen, D.J. Jensen, The deformation behaviour of grain boundary regions in polycrystalline aluminium, Philos. Mag. A Phys. Condens. Matter, Struct. Defects Mech. Prop. 73 (1996) 265–282.

[66] Y. Kawasaki, Cell structures in deformed copper single crystals, J. Phys. Soc. Japan. 36 (1974) 142–148.

[67] D.B. Miracle, S.L. Donaldson, S.D. Henry, C. Moosbrugger, G.J. Anton, B.R. Sanders, N. Hrivnak, C. Terman, J. Kinson, K. Muldoon, ASM Handbook Metallography and Microstructures, ASM Int. 09 (2004) 3470.

[68] S. Nishikawa, S. Kikuchi, The diffraction of cathode rays by calcite, in: Proc. Imp. Acad., 1928: pp. 475–477.

[69] B.L. Adams, S.I. Wright, K. Kunze, Orientation imaging: the emergence of a new microscopy, Metall. Trans. A. 24 (1993) 819–831.

[70] S. Zaefferer, R.A. Schwarzer, Automated measurement of single grain orientations in the TEM, Zeitschrift Für Met. 85 (1994) 585–591.

[71] R.A. Schwarzer, J. Sukkau, Automated crystal orientation mapping (ACOM) with a computer-controlled TEM by interpreting transmission kikuchi patterns, Mater. Sci. Forum. 273–275 (1998) 215–222.

[72] A.J. Wilkinson, A new method for determining small misorientations from electron back scatter diffraction patterns, Scr. Mater. 44 (2001) 2379–2385.

[73] I. Brough, P.S. Bate, F.J. Humphreys, Optimising the angular resolution of EBSD, Mater. Sci. Technol. 22 (2006) 1279–1286.

[74] A. Arsenlis, D.M. Parks, Crystallographic aspects of geometrically-necessary and statistically-stored dislocation density, Acta Mater. 47 (1999) 1597–1611.

[75] S. Sun, B.L. Adams, W.E. King, Observations of lattice curvature near the interface of a deformed aluminium bicrystal, Philos. Mag. A Phys. Condens. Matter, Struct. Defects Mech. Prop. 80 (2000) 9–25.

[76] A.J. Schwartz, M. Kumar, B.L. Adams, David P. Field, Electron Backscatter Diffraction in Materials Science, (2000).

[77] J.A. Venables, C.J. Harland, Electron back-scattering patterns—a new technique for obtaining crystallographic information in the scanning electron microscope, Philos. Mag. 27 (1973) 1193–1200.

[78] A. Winkelmann, G. Cios, T. Tokarski, G. Nolze, R. Hielscher, T. Kozie, EBSD orientation analysis based on experimental Kikuchi reference patterns, Acta Mater. 188 (2020) 1–10.

[79] C. Ernould, B. Beausir, J.J. Fundenberger, V. Taupin, E. Bouzy, Global DIC approach guided by a cross-correlation based initial guess for HR-EBSD and on-axis HR-TKD, Acta Mater. 191 (2020) 131–148.

[80] B. Beausir, J.-J. Fundenberger, Analysis Tools for Electron and X-ray diffraction, ATEX - software, (2017). www.atex-software.eu.

[81] C. Fressengeas, B. Beausir, C. Kerisit, A.L. Helbert, T. Baudin, F. Brisset, M.H. Mathon, R. Besnard, N. Bozzolo, On the evaluation of dislocation densities in pure tantalum from EBSD orientation data, Mater. Tech. 106 (2018).

[82] G.M. Hughes, G. Smith, A.G. Crocker, P.E.J. Flewitt, An examination of the linkage of cleavage cracks at grain boundaries, Mater. Sci. Technol. 21 (2005) 1268–1274.

[83] M.W. Phaneuf, Applications of focused ion beam microscopy to materials science specimens, Micron. 30 (1999) 277–288.

[84] P.R. Munroe, The application of focused ion beam microscopy in the material sciences, Mater. Charact. 60 (2009) 2–13.

[85] B. Chen, P.E.J. Flewitt, D.J. Smith, C.P. Jones, An improved method to identify grain boundary creep cavitation in 316H austenitic stainless steel, Ultramicroscopy. 111 (2011) 309–313.

[86] S.P. Baker, J. Liu, Nanoindentation Techniques, Ref. Modul. Mater. Sci. Mater. Eng. (2016) 1–9.

[87] X. Hou, N.M. Jennett, Application of a modified slip-distance theory to the indentation of single-crystal and polycrystalline copper to model the interactions between indentation size and structure size effects, Acta Mater. 60 (2012) 4128–4135.

[88] W.C. Oliver, G.M. Pharr, An improved technique for determining hardness and elastic modulus using load and displacement sensing indentation experiments, J. Mater. Res. 7 (1992) 1564–1583.

[89] C. Leinenbach, M. Koster, H.J. Schindler, Fatigue assessment of defect-free and defect-containing brazed steel joints, J. Mater. Eng. Perform. 21 (2012) 739–747.

[90] B. Chen, J.N. Hu, P.E.J. Flewitt, A.C.F. Cocks, R.A. Ainsworth, D.J. Smith, D.W. Dean, F. Scenini, Effect of thermal ageing on creep and oxidation behaviour of Type 316H stainless steel, Mater. High Temp. 32 (2015) 592–606.

[91] T. Poulain, J. Mendez, G. Hénaff, L. de Baglion, Analysis of the ground surface finish effect on the LCF life of a 304L austenitic stainless steel in air and in PWR environment, Eng. Fract. Mech. 185 (2017) 258–270.

[92] M. Wu, L. Chang, L. Zhang, X. He, X. Qu, Effects of roughness on the wettability of high temperature wetting system, Surf. Coatings Technol. 287 (2016) 145–152.

[93] D. Shi, C. Dong, X. Yang, Y. Sun, J. Wang, J. Liu, Creep and fatigue lifetime analysis of directionally solidified superalloy and its brazed joints based on continuum damage mechanics at elevated temperature, Mater. Des. 45 (2013) 643–652.

[94] Y. Suezawa, Relation between the mechanical properties of the steel brazed joints and its filler metal elements and surface roughness of base metal, in: Proc. 23rd Heat Treat. Soc. Conf., 2006: pp. 135–142.

[95] P. Paris, F. Erdogan, A critical analysis of crack propagation laws, J. Basic Eng. 85 (1963) 528–533.

[96] J. Günther, D. Krewerth, T. Lippmann, S. Leuders, T. Tröster, A. Weidner, H. Biermann, T. Niendorf, Fatigue life of additively manufactured Ti–6Al–4V in the very high cycle fatigue regime, Int. J. Fatigue. 94 (2017) 236–245.

[97] A.M.P. De Jesus, R. Matos, B.F.C. Fontoura, C. Rebelo, L. Simões Da Silva, M. Veljkovic, A comparison of the fatigue behavior between S355 and S690 steel grades,

J. Constr. Steel Res. 79 (2012) 140–150.

[98] R. Seifi, R. Hosseini, Experimental study of fatigue crack growth in raw and annealed pure copper with considering cyclic plastic effects, Theor. Appl. Fract. Mech. 94 (2018) 1–9.

[99] K. Obrtlík, J. Polák, M. Hájek, A. Vašek, Short fatigue crack behaviour in 316L stainless steel, Int. J. Fatigue. 19 (1997) 471–475.

[100] J. Newman Jr, The merging of fatigue and fracture mechanics concepts: a historical perspective, Prog. Aerosp. Sci. 34 (1998) 347–390.

[101] C.W. Brown, M.A. Hicks, A study of short fatigue crack growth behaviour in titanium alloy ImI 685, Fatigue Eng. Mater. Struct. 6 (1983) 67–76.

[102] T. Ogura, S. Hirosawa, A. Cerezo, T. Sato, Atom probe tomography of nanoscale microstructures within precipitate free zones in Al-Zn-Mg(-Ag) alloys, Acta Mater. 58 (2010) 5714–5723.

[103] X. Ma, C. Huang, J. Moering, M. Ruppert, H.W. Höppel, M. Göken, J. Narayan, Y. Zhu, Mechanical properties of copper/bronze laminates: Role of interfaces, Acta Mater. 116 (2016) 43–52.

[104] T. Grosdidier, A. Hazotte, A. Simon, Precipitation and dissolution processes in γ/γ′ single crystal nickel-based superalloys, Mater. Sci. Eng. A. 256 (1998) 183–196.

[105] X. Fan, Z. Guo, X. Wang, J. Yang, J. Zou, Morphology evolution of γ′ precipitates in a powder metallurgy Ni-base superalloy, Mater. Charact. 139 (2018) 382–389.

[106] S.R.B. Cooke, S. Aschenbrenner, The occurrence of metallic iron in ancient copper, J. F. Archaeol. 2 (1975) 251–266.

[107] P.G. Sanders, J.A. Eastman, J.R. Weertman, Elastic and tensile behavior of nanocrystalline copper and palladium, Acta Mater. 45 (1997) 4019–4025.

[108] R.V. Steward, M.L. Grossbeck, B.A. Chin, H.A. Aglan, Y. Gan, Furnace brazing type 304 stainless steel to vanadium alloy (V-5Cr-5Ti), J. Nucl. Mater. 287 (2000) 1224–1228.

[109] D.M. Minić, A. Gavrilović, D.M. Minić, L.D. Rafailović, P. Angerer, J. Wosik, A. Mariĉić, Phase transformations of Fe73.5Cu1Nb3Si15.5B7 amorphous alloy upon thermal treatment, J. Alloys Compd. 504 (2010) 462–467.

[110] X. Shu, G. Chen, J. Liu, B. Zhang, J. Feng, Microstructure evolution of copper/steel gradient deposition prepared using electron beam freeform fabrication, Mater. Lett. 213 (2018) 374–377.

[111] S. Klein, S. Weber, W. Theisen, Effect of heat treatment on phase structure and thermal

conductivity of a copper-infiltrated steel, J. Mater. Sci. 50 (2015) 3586–3596.

[112] A. Chbihi, X. Sauvage, D. Blavette, Atomic scale investigation of Cr precipitation in copper, Acta Mater. 60 (2012) 4575–4585.

[113] A. Popovich, V. Sufiiarov, I. Polozov, E. Borisov, D. Masaylo, A. Orlov, Microstructure and mechanical properties of additive manufactured copper alloy, Mater. Lett. 179 (2016) 38–41.

[114] X. Zhang, C. Lin, S. Cui, Z. Li, Characteristics of nano-alumina particles dispersion strengthened copper fabricated by reaction synthesis, Rare Met. Mater. Eng. 45 (2016) 893–896.

[115] J.Y. He, H. Wang, H.L. Huang, X.D. Xu, M.W. Chen, Y. Wu, X.J. Liu, T.G. Nieh, K. An, Z.P. Lu, A precipitation-hardened high-entropy alloy with outstanding tensile properties, Acta Mater. 102 (2016) 187–196.

[116] L. Peng, H. Xie, G. Huang, G. Xu, X. Yin, X. Feng, X. Mi, Z. Yang, The phase transformation and strengthening of a Cu-0.71 wt% Cr alloy, J. Alloys Compd. 708 (2017) 1096–1102.

[117] G. Shi, X. Chen, H. Jiang, Z. Wang, H. Tang, Y. Fan, Strengthening mechanisms of Fe nanoparticles for single crystal Cu-Fe alloy, Mater. Sci. Eng. A. 636 (2015) 43–47.

[118] K.R. Anderson, J.R. Groza, Microstructural size effects in high-strength high-conductivity Cu-Cr-Nb alloys, Metall. Mater. Trans. A Phys. Metall. Mater. Sci. 32 (2001) 1211–1223.

[119] Y.J. Li, A.M.F. Muggerud, A. Olsen, T. Furu, Precipitation of partially coherent α-Al(Mn,Fe)Si dispersoids and their strengthening effect in AA 3003 alloy, Acta Mater. 60 (2012) 1004–1014.

[120] F. Qian, S. Jin, G. Sha, Y. Li, Enhanced dispersoid precipitation and dispersion strengthening in an Al alloy by microalloying with Cd, Acta Mater. 157 (2018) 114–125.

[121] Y.Y. Zhao, H.W. Chen, Z.P. Lu, T.G. Nieh, Thermal stability and coarsening of coherent particles in a precipitation-hardened (NiCoFeCr)94Ti2Al4 high-entropy alloy, Acta Mater. 147 (2018) 184–194.

[122] P.H. Thornton, R.G. Davies, T.L. Johnston, The temperature dependence of the flow stress of the γ′ phase based upon Ni3Al, Metall. Trans. 1 (1970) 207–218.

[123] H. Gleiter, E. Hornbogen, Precipitation hardening by coherent particles, Mater. Sci. Eng. 2 (1968) 285–302.

[124] A. Sengupta, S.K. Putatunda, L. Bartosiewicz, J. Hangas, P.J. Nailos, M. Peputapeck,

F.E. Alberts, Tensile behavior of a new single crystal nickel-based superalloy (CMSX-4) at room and elevated temperatures, J. Mater. Eng. Perform. 3 (1994) 664–672.

[125] A.J. Ardell, Precipitation hardening, Metall. Mater. Trans. A. 16 (1985) 2131–2165.

[126] R.E. Smallman, A.H.W. Ngan, Modern Physical Metallurgy, 8th ed., Oxford, UK, 2014.

[127] Z.C. Cordero, B.E. Knight, C.A. Schuh, Six decades of the Hall–Petch effect – a survey of grain-size strengthening studies on pure metals, Int. Mater. Rev. 61 (2016) 495–512.

[128] C.A. Mackliet, Diffusion of iron, cobalt, and nickel in single crystals of pure copper, Phys. Rev. 109 (1958).

[129] N.A. Gokcen, The Cu-Mn (copper-manganese) system, J. Phase Equilibria. 14 (1993) 76–83.

[130] K. Hoshino, Y. Iijima, K.I. Hirano, Diffusion of vanadium, chromium, and manganese in copper, Metall. Trans. A. 8 (1977) 469–472.

[131] C.A. Schuh, T.G. Nieh, H. Iwasaki, The effect of solid solution W additions on the mechanical properties of nanocrystalline Ni, Acta Mater. 51 (2003) 431–443.

[132] J.Y. He, W.H. Liu, H. Wang, Y. Wu, X.J. Liu, T.G. Nieh, Z.P. Lu, Effects of Al addition on structural evolution and tensile properties of the FeCoNiCrMn high-entropy alloy system, Acta Mater. 62 (2014) 105–113.

[133] O. Engler, Deformation and texture of copper-manganese alloys, Acta Mater. 48 (2000) 4827–4840.

[134] Y. Chen, X. Zhang, E. Liu, C. He, C. Shi, J. Li, P. Nash, N. Zhao, Fabrication of in-situ grown graphene reinforced Cu matrix composites, Sci. Rep. 6 (2016) 1–9.

[135] W. Zhang, W. Jiang, Y. Yu, F. Zhou, Y. Luo, M. Song, Fatigue crack simulation of the 316L brazed joint using the virtual crack closure technique, Int. J. Press. Vessel. Pip. 173 (2019) 20–25.

[136] C. Xiao, W. Jiang, Y. Yu, M. Song, S.-T. Tu, J. Gong, Influence of borides dissolution during the homogenization treatment on the mechanical properties and fracture behavior of austenitic stainless steel brazed joints, Mater. Sci. Eng. A. 782 (2020) 139200.

[137] L.X. Zhang, J.C. Feng, P. He, Brazing temperature and time effects on the mechanical properties of TiC cermet/Ag-Cu-Zn/steel joints, Mater. Sci. Eng. A. 428 (2006) 24–33.

[138] Z. Wei, W. Jiang, M. Song, C. Xiao, S.T. Tu, Effects of element diffusion on microstructure evolution and residual stresses in a brazed joint: Experimental and numerical modeling, Materialia. 4 (2018) 540–548.

[139] D.A. Hughes, N. Hansen, High angle boundaries formed by grain subdivision mechanisms, Acta Mater. 45 (1997) 3871–3886.

[140] J.M. Choung, S.R. Cho, Study on true stress correction from tensile tests, J. Mech. Sci. Technol. 22 (2008) 1039–1051.

[141] Z.L. Zhang, M. Hauge, J. Ødegård, C. Thaulow, Determining material true stress-strain curve from tensile specimens with rectangular cross-section, Int. J. Solids Struct. 36 (1999) 3497–3516.

[142] Z.L. Zhang, J. Ødegård, O.P. Søvik, Determining true stress-strain curve for isotropic and anisotropic materials with rectangular tensile bars: Method and verifications, Comput. Mater. Sci. 20 (2001) 77–85.

[143] N. Li, J. Wang, J.Y. Huang, A. Misra, X. Zhang, In situ TEM observations of room temperature dislocation climb at interfaces in nanolayered Al/Nb composites, Scr. Mater. 63 (2010) 363–366.

[144] H.H. Lee, J.I. Yoon, H.K. Park, H.S. Kim, Unique microstructure and simultaneous enhancements of strength and ductility in gradient-microstructured Cu sheet produced by single-roll angular-rolling, Acta Mater. 166 (2019) 638–649.

[145] X. Wu, Y. Zhu, Heterogeneous materials: a new class of materials with unprecedented mechanical properties, Mater. Res. Lett. 5 (2017) 527–532.

[146] C.W. Shao, P. Zhang, Y.K. Zhu, Z.J. Zhang, Y.Z. Tian, Z.F. Zhang, Simultaneous improvement of strength and plasticity: Additional work-hardening from gradient microstructure, Acta Mater. 145 (2018) 413–428.